A CFD Investigation of Turbulent Buoyant Helium Plumes

by

William Chung

A thesis
presented to the University of Waterloo
in fulfillment of the
thesis requirement for the degree of
Master of Applied Science
in
Mechanical Engineering

Waterloo, Ontario, Canada, 2007

I hereby declare that I am the sole author of this thesis. This is a true copy of the thesis, including any required final revisions, as accepted by my examiners.

I understand that my thesis may be made electronically available to the public.

William Chung

Abstract

The objective of this work is to assess the capabilities of two modeling approaches, Reynolds-Averaged Navier Stokes (RANS) and Large Eddy Simulation (LES), to investigate turbulent buoyant helium plumes for the purpose of studying the dynamics of buoyancy driven plumes in the near source region. In this case, the velocity and plume concentration of the plume are predicted.

RANS was applied to a model planar wall plume and predictions were compared to experimental data gathered in the self-preserving region. It was also used to model an axisymmetric plume with results compared to experimental data gathered in the near source region. The Simple Gradient Diffusion Hypothesis (SGDH) and the Generalized Gradient Diffusion Hypothesis (GGDH) were implemented in the standard k-ε model for the planar plume. The CFX buoyancy model in the commercial code, as well as SGDH and GGDH, were applied in predicting the characteristics of the axisymmetric plume. For the planar plume, good agreement with the experimental data was found when the SGDH approach was used. Both spreading rates and maximum values of velocity and mixture fraction were well predicted. Larger discrepancies between predictions and data were noticed with the GGDH model. Both models showed minimal sensitivity to the model constant, $C_{3\varepsilon}$. In the case of the axisymmetric plume, all models were highly sensitive to the buoyancy constant. The GGDH model yielded the best results. In particular very good agreement was achieved for the radial profiles of the streamwise velocity.

The axisymmetric plume was also simulated using LES. Initially the Smagorinsky constant was set at the default value of 0.2 and the grid size was varied to determine the dependency of the time averaged and rms quantities for velocity and plume concentration on the grid spacing. The two finest meshes tested produced similar time averaged values for velocity and plume concentration indicating that they were less sensitive to grid spacing. These time averaged results also showed that values for streamwise velocity and plume concentration along the central axis were significantly over predicted compared to the experimental results. Time-averaged centerline streamwise velocity plots showed that the streamwise velocity from the numerical results continue to increase while the experimental values begin to decrease after 0.69 m. This indicated that the transition from laminar-to-turbulence was poorly predicted. Rms quantities remained sensitive to the mesh spacing

even at the finest mesh tested; however the accuracy of the rms results appeared to improve as the grid was refined. Setting the Smagorinsky constant to zero produced a more accurate time averaged predictions but the rms quantities worsened.

Acknowledgments

The author wishes to acknowledge his advisor, Dr. Cécile Devaud, for her guidance and support and NSERC for their financial support.

Contents

List of Tables

List of Figures

Nomenclature

B_o	source buoyancy flux $[m^3/s^3]$
C	Kolmogorov constant
$C_{1\varepsilon}$	model constant in turbulent dissipation equation
$C_{2\varepsilon}$	model constant in turbulent dissipation equation
C_3	CFX buoyancy constant
$C_{3\varepsilon}$	buoyancy constant
C_s	Smagorinsky constant
C_μ	turbulent viscosity constant
D	plume source diameter $[m]$
$F\,(x/y)$	self-preserving parameter for plume mixture fraction
F_{max}	maximum plume mixture fraction
$E\,(\kappa)$	energy-spectrum function $[m^3/s^2]$
G	production of turbulent kinetic energy due to buoyancy $[kg/ms^3]$
$G\,(x, x')$	LES filter function $[1/m]$
L	length of side of cube in physical space $[m]$
M	number of time steps
N	number of grid nodes along one length of the cube in physical space
P	production of turbulent kinetic energy due to shear $[kg/ms^3]$
P_{ij}	rate of production of Reynolds stress $[kg/ms^3]$
R_{ij}	pressure rate-of-strain tensor $[kg/ms^3]$
R_f	flux Richardson number
Re	Reynolds number
S_ε	dissipation equation source term $[kg/ms^4]$
$S_{\varepsilon B}$	effect of buoyancy source term in the turbulent dissipation equation $[kg/ms^4]$
$\overline{S}$	filtered rate-of-strain $[1/s]$
$\overline{S}_{ij}$	filtered rate-of-strain tensor $[1/s]$
T_{kij}	flux of Reynolds stress $[kg/s^3]$
$T_{kij}^{(p)}$	flux of Reynolds stress due to fluctuating pressure $[kg/s^3]$
$T_{kij}^{(u)}$	flux of Reynolds stress due to turbulent convection $[kg/s^3]$
$T_{kij}^{(\nu)}$	diffusive flux of Reynolds stress $[kg/s^3]$

$V\,(x/y)$	self-preserving parameter for velocity $[m/s]$
V_{max}	maximum velocity $[m/s]$
V_o	inlet velocity $[m/s]$
a_{ij}	anisotropic Reynolds stresses $[m^2/s^2]$
b	slot width $[m]$
f	plume mixture fraction
g_j	gravitational acceleration $[m/s^2]$
k	turbulent kinetic energy $[m^2/s^2]$
l_f	characteristic plume width for plume mixture fraction $[m]$
l_m	mixing length $[m]$
l_v	characteristic plume width for velocity $[m]$
p	pressure $[N/m^2]$
p'	fluctuating pressure $[N/m^2]$
$\vec{r}$	vector from the upwind node to the integration point
t	time $[s]$
u_i	velocity component in the i-direction $[m/s]$
u_η	Kolmogorov velocity $[m/s]$
v_o	source velocity $[m/s]$
x_i	coordinate direction $[m]$
Δ	filter width $[m]$
Δt	time step $[s]$
Δx	grid spacing $[m]$
Γ_t	turbulent diffusivity $[kg/ms]$
β	blending factor
δ_{ij}	Kronecker delta
ε	rate of dissipation of turbulent kinetic energy $[m^2/s^3]$
ε_{ij}	dissipation tensor $[m^2/s^3]$
η	Kolmogorov lengthscale $[m]$

κ	wavenumber $[1/m]$
μ	molecular viscosity $[kg/ms]$
μ_t	turbulent or eddy viscosity $[kg/ms]$
ν	kinematic viscosity $[m^2/s]$
ν_t	turbulent viscosity $[m^2/s]$
ϑ	turbulent velocity scale $[m/s]$
ρ	density $[kg/m^3]$
ρ_o	source gas density $[kg/m^3]$
ρ_∞	reference density $[kg/m^3]$
σ_k	turbulent Prandtl number for kinetic energy
σ_t	turbulent Prandtl number for production of turbulent kinetic energy due to buoyancy
σ_ε	turbulent Prandtl number for dissipation
σ_ρ	CFX model constant
τ	turbulence timescale $[s]$
τ_{ij}	stress tensor $[N/m^2]$
τ_{ij}^s	subgrid-scale Reynolds stress $[N/m^2]$
τ_η	Kolmogorov timescale $[s]$
$\overline{\phi}$	Reynolds-averaged quantity (RANS)
$\overline{\phi}$	filtered quantity (LES)
ϕ'	fluctuating component
ϕ_{ip}	value at the integration point
ϕ_{up}	value at the upwind node
∇	gradient operator

Chapter 1

Introduction

Fire safety engineering is an important and necessary discipline applicable in everyday life. From 1993 to 2002 Canada has experienced just under 600,000 fires. These fires led to 375 deaths, 3000 injuries and over $1.2 billion in losses annually [5]. The investigation of fires that have taken place can aid in decreasing these numbers but simply relying on experience gained from past fires is insufficient to enhance safety . It is also necessary to study and understand fire behavior from an engineering standpoint. This includes gaining knowledge on fire initiation, growth and the spread of full-scale fires, as well as their environmental interactions and impacts. With more insight into fire dynamics, preventative measures can be developed and fire safety measures can be designed into structures and other components to minimize the spread and effects of fire, ultimately leading to a decrease in death, injury and losses.

Fire modeling is an important tool in developing fire prevention measures and determining optimal fire safety designs. Fires can be modeled to determine the extent of damages that may occur in defined situations, as well as to assess probable fire risks which may arise. This can be achieved through experimental or numerical methods.

The study of non-reacting buoyant plumes is an important step in understanding the convective transport of fluids and is useful in fire modeling. In situations where the prediction of fire spreading rates and overall smoke plume dynamics are desired, and values

for combustion rate and chemical components are not necessary, the simulation can be simplified and cost can be reduced by modeling a non-reacting buoyant plume with an equivalent Froude number to that expected in the fire of interest [6]. This is because the hot combustion products resulting from a fire have similar movement and flow dynamics to that of a buoyant plume. Thus the buoyant plume is a good substitution in the modeling of fires.

The present work involves a numerical investigation of non-reacting buoyant plumes for application in fire safety. Background on turbulence, CFD and previous numerical studies of buoyant plumes are described in Chapter 2. This chapter introduces the various modeling approaches within CFD and how they relate to turbulent flows. It provides information on numerical methods used in the past to model the buoyant plume and how they lead to the present work. The present work is then described including the methods to be used and the test cases against which model outputs will be compared.

Two of the modeling approaches described in Chapter 2 are implemented in the present work in simulating a large turbulent buoyant helium plume. The model equations and simulation parameters for each of these are described, and results are compiled and presented, in Chapters 3 and 4. These chapters discuss how the flow dynamics predicted using the numerical model compare to the experimental data. The dependency of the results on certain model parameters is also examined, as well as how the results compare to those obtained in the past using similar techniques. This discussion is followed with conclusions and future work in Chapter 5.

Chapter 2

Background

This chapter introduces the importance of turbulence in buoyant plumes. The energy cascade is used to explain how energy is passed from the large scales of motion to the dissipative scales and the Kolmogorov hypotheses is introduced to explain the isotropic motion of the dissipative scales. Following this, the various numerical methods are discussed along with examples of models devised in the past. This leads to the literature review which describes a collection of numerical work on turbulent buoyant plumes. It shows the evolution of the study leading up to the present work. Details of the present research are then given along with the details of the test cases.

2.0.1 Turbulent buoyant jets and plumes

Rodi [1] distinguishes three types of turbulent flows: turbulent jets, turbulent plumes and turbulent buoyant jets or forced plumes. In a turbulent jet the main source of kinetic energy and momentum flux for fluid motion is a pressure drop through an orifice. The defining factor in jets is the outward flow of momentum from the jet to the surroundings. This momentum is distributed to the surroundings through vortex structures which also aid in the jet growth. Two turbulent jets are depicted in Figs. 2.1 and 2.2. These two figures display the initial jet region which propagates from the jet source. This exit jet

breaks down into vortex structures. A turbulent plume, such as the one shown in Fig. 2.3, arises when the primary source of kinetic energy and momentum flux is a gravitational force. Properties and characteristics of the turbulent plume are defined by the buoyancy flux which is the rate of production of weight deficiency. Turbulent buoyant jets form when a turbulent jet transitions to a plume. Thus, when the motion of the fluid is primarily dependent on the weight deficiency rather than an initial momentum flux, the jet takes on the characteristics of a plume.

2.1 Turbulent Flows

Buoyancy driven flows are turbulent. This turbulence is generated from the buoyancy of the plume gas rising into the ambient fluid and thus, it is necessary to understand the fundamentals of turbulence. Turbulent flows are characterized as being unsteady and irregular consisting of many scales of motion. This leads to a random velocity field with a wide variation in characteristics in both space and time. In a turbulent flow, the fluids and the properties these fluids carry mix.

Turbulent flow consists of rotational flow structures, called eddies, in a wide range of length scales. These length scales can range in size from the width of the flow to those which are too small to be seen by the human eye. The larger scales of motion predominately transport the conserved properties and are very dependent on initial conditions and boundary conditions while the smaller ones are independent of initial geometry and are relatively isotropic leading to a universal form. To describe the energy distribution and how energy is transferred between the eddies, Richardson [7] introduced the concept of flow through an energy cascade. The energy cascade hypothesizes that kinetic energy enters the turbulent flow via flow structure of the size of the largest eddies. The large eddies break up into smaller eddies and in the process transfer energy down to smaller scales. Viscosity effects become important at the smaller eddies and the energy is dissipated.

The Kolmogorov hypotheses [8] introduced the idea that the smallest scales of motion are isotropic. The motion of the large length scales are very dependent on the mean flow.

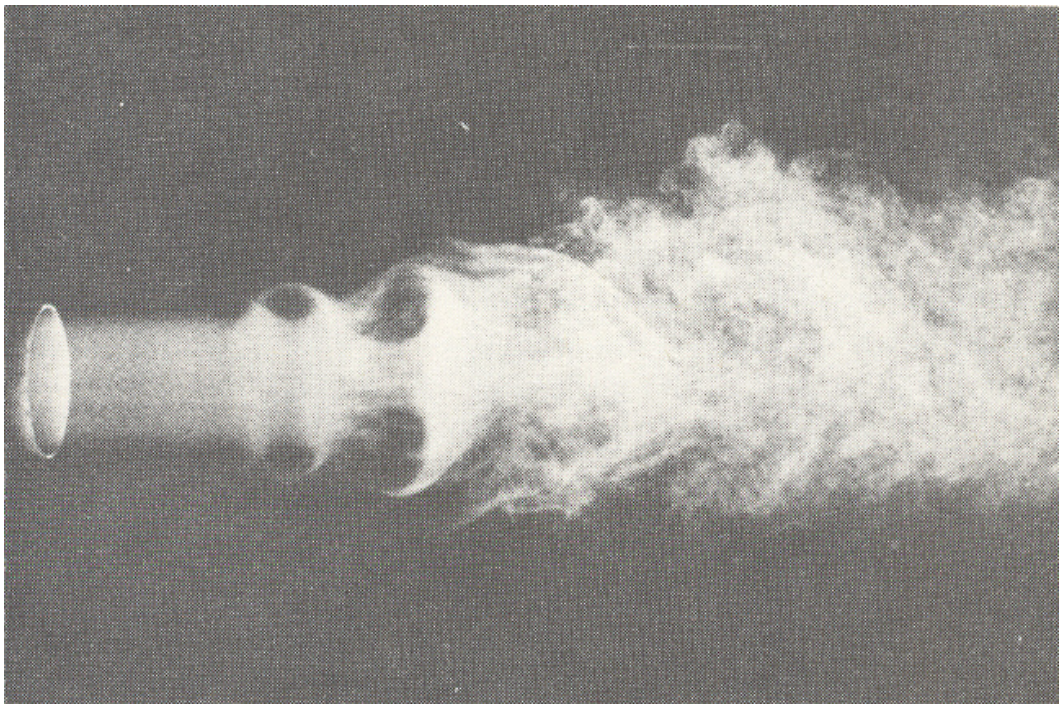

Figure 2.1: Turbulent jet with exit Reynolds number of $10.5 \text{x} 10^4$. (Photograph courtesy of Steven Crow and Cambridge University Press [1])

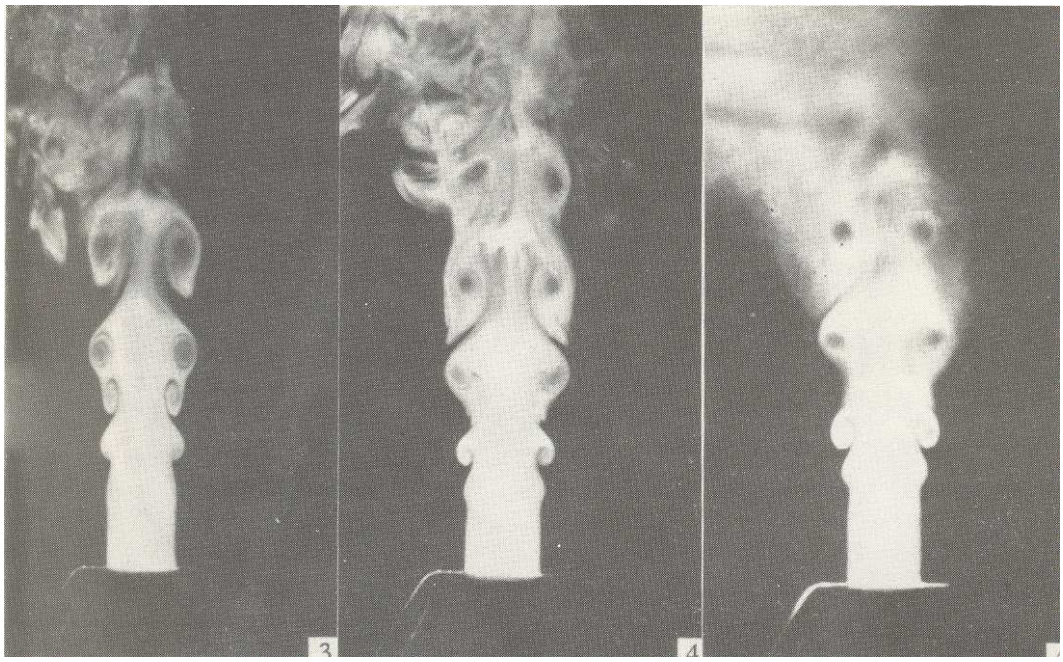

Figure 2.2: Axisymmetric turbulent jet. (Photographs courtesy of Cambridge University Press [1])

Figure 2.3: Plane turbulent plume showing large scale motions (Photograph courtesy of Kotsovinos [1]).

As the length scales decrease so does the directional dependence of the eddies on the mean flow. Therefore, the small scales of motion become independent of the initial geometry and tend toward a universal form. This means that the small scales of motion are similar in all turbulent flows and only dependent on the energy transferred down to them and the kinematic viscosity, ν.

The energy spectrum function, $E(\kappa)$, describes the turbulent kinetic energy distribution among the various sized eddies. The energy spectrum is the relationship between the energy density per unit wave number, E, the wave number, κ, and the dissipation rate, ε. From Kolmogorov's hypothesis, the spectrum is defined as:

$$E(\kappa) = C\varepsilon^{2/3}\kappa^{-5/3}, \tag{2.1}$$

where C is a universal constant. This energy spectrum is important in understanding the three modeling approaches to be described in the following section.

2.2 Numerical Methods

Experimental procedures for investigating plume dynamics require detailed measurements which can be costly and time-consuming. Computational Fluid Dynamics (CFD) play an important role in the modeling of flows, offering a versatile tool for determining flow dynamics. In CFD there are three primary modeling approaches: Direct Numerical Simulation (DNS), Large Eddy Simulation (LES) and Reynolds-Averaged Navier-Stokes (RANS). This section describes each approach and how they are implemented.

2.2.1 DNS

DNS is the most accurate approach to turbulence simulation. The Navier-Stokes equations are solved without averaging or approximation for each realization of the flow. All the motions in the flow are fully resolved in this method, and therefore the size of the grid must be small enough to capture all of the smaller scales of motion.

The computational cost of DNS modeling of homogeneous turbulence for a cubic domain is based on the length of one side of the domain, L, the grid spacing, Δx, and the time step, Δt. The overall computational domain must be large enough to capture the largest eddies characteristic of the flow of interest. The grid spacing is dependent on the size of the dissipative scales which must be resolved. The time step chosen is dependent on the level of accuracy. For a solution to be accurate in time, the time step must be such that a fluid parcel does not move further than one grid spacing per time step. The number of grid nodes required, N^3, and the number of time steps required, M, are dependent on the Reynolds number. The number of grid nodes required for one dimension of the domain, N, is:

$$N \propto Re^{3/4}. \tag{2.2}$$

Therefore, the total number of grid nodes required is:

$$N^3 \propto Re^{9/4}. \tag{2.3}$$

The time step is related to the grid spacing through the Courant number and the turbulent kinetic energy,

$$\frac{k^{1/2}\Delta t}{\Delta x} = \frac{1}{20}. \tag{2.4}$$

It is recommended that a solution run be on the order of four times the turbulence time scale, $\tau = k/\varepsilon$ [9]. Therefore, the total number of time steps required is:

$$M = \frac{4\tau}{\Delta t} \propto Re^{3/4}. \tag{2.5}$$

As the Reynolds number increases both the number of grid nodes and time steps required to fully resolve the turbulent nature of the flow increase rapidly. Therefore, due to computational limitations, DNS simulations are limited to low Reynolds number flows in a relatively simple geometrical domain. Thus, DNS is too computationally expensive for practical engineering flows. As computer technology enhances, this may be a feasible option in the future.

2.2.2 LES

LES takes advantage of the fact that while the larger length scales are very dependent on the initial conditions and boundary conditions the smaller length scales are isotropic. A filtering operation is used to separate the large scale motions, which are resolved, from the small ones, which are modeled. This allows for a coarser grid than what would be used in DNS. In this way computational cost can be saved compared to DNS, where a large portion of the computational cost arises from resolving the dissipative scales. The filtered velocity is defined as:

$$\overline{u}_i(x,t) = \int G(x,x')\, u_i(x',t)\, dx', \tag{2.6}$$

where $\overline{u}$ is the filtered velocity field and the localized function, $G(x,x')$, is the filter kernel.

The velocity field, $u_i(x,t)$, is defined as a sum of the filtered component, $\overline{u}_i(x,t)$, and the residual component, $u'(x,t)$ as shown in Eq.(2.7).

$$u_i(x,t) = \overline{u}_i(x,t) + u'(x,t) \tag{2.7}$$

The filtered velocity field can be derived using the mass continuity equation (Eq.(2.8)) and the filtered Navier-Stokes equations (Eq.(2.8)).

$$\frac{\partial \rho}{\partial t} + \frac{\partial(\rho \overline{u}_j)}{\partial x_j} = 0, \tag{2.8}$$

$$\frac{\partial(\rho \overline{u}_i)}{\partial t} + \frac{\partial(\rho \overline{u_i u_j})}{\partial x_j} = -\frac{\partial \overline{p}}{\partial x_i} + \frac{\partial \overline{\tau}_{ij}}{\partial x_j}, \tag{2.9}$$

where ρ is the density and $\overline{p}$ is the filtered pressure field. The equations are closed by modeling the viscous stress tensor. The viscous stress tensor, $\overline{\tau}_{ij}$, is often defined using the Smagorinsky model [10] as:

$$\overline{\tau}_{ij} = -2\mu_t \overline{S}_{ij}, \tag{2.10}$$

where $\overline{S}_{ij}$ is the filtered rate of strain tensor. The turbulent viscosity, μ_t, is a function of density, ρ, the filter width, Δ, and the characteristic filtered rate of strain, $\overline{S}$. It is defined as:

$$\mu_t = C_s^2 \rho \Delta^2 \left|\overline{S}\right|, \tag{2.11}$$

where C_s is an empirical constant. The filtered rate of strain tensor and the characteristic filtered rate of strain are defined as:

$$\overline{S}_{ij} = \frac{1}{2}\left(\frac{\partial \overline{u}_i}{\partial x_j} + \frac{\partial \overline{u}_j}{\partial x_i}\right), \tag{2.12}$$

$$\overline{S} = \left(2\overline{S}_{ij}\overline{S}_{ij}\right)^{1/2}. \tag{2.13}$$

There have been numerous refinements to the Smagorinsky model including various dynamic subgrid-scale (SGS) stress models which locally calculate the eddy viscosity coefficient, C_s [11, 12, 13]. The improvement on the original Smagorinsky model from these refinements is difficult to gauge for fire plumes, due to the fact that the behavior of the flow field in fire plumes is dominated by the large-scale resolvable eddies and thus the smaller scales have a lesser impact [14].

2.2.3 RANS

All scales of motion are modeled for the RANS approach. The transport equations (Eqs.(2.14-2.16)) are solved for the time averaged velocity field.

$$\frac{\partial \rho}{\partial t} + \frac{\partial\left(\rho \overline{u}_j\right)}{\partial x_j} = 0, \tag{2.14}$$

$$\frac{\partial\left(\rho \overline{u}_i\right)}{\partial t} + \frac{\partial}{\partial x_j}\left(\rho \overline{u}_i \overline{u}_j + \rho\overline{u_i' u_j'}\right) = -\frac{\partial \overline{p}}{\partial x_i} + \frac{\partial \overline{\tau}_{ij}}{\partial x_j}, \tag{2.15}$$

$$\frac{\partial \rho\overline{\phi}}{\partial t} + \frac{\partial}{\partial x_j}\left(\rho\overline{u_j}\overline{\phi} + \rho\overline{u_j'\phi'}\right) = \frac{\partial}{\partial x_j}\left(\Gamma\frac{\partial \overline{\phi}}{\partial x_j}\right), \tag{2.16}$$

where ρ is the density and $\overline{p}$ is the mean pressure. The mean viscous stress tensor component, $\overline{\tau}_{ij}$ is:

$$\overline{\tau}_{ij} = \mu\left(\frac{\partial \overline{u}_i}{\partial x_j} + \frac{\partial \overline{u}_j}{\partial x_i}\right). \tag{2.17}$$

The unknown Reynolds stresses are solved for using a turbulence model. Turbulence modeling uses a simpler mathematical model to predict the effects of turbulence over the full time dependent Navier-Stokes equations. This turbulence model either can be based on

a turbulent viscosity hypothesis or Reynolds-stress transport equations. The assumption behind the turbulent viscosity hypothesis is that the mean velocity gradient, $\frac{\partial \overline{u}_i}{\partial x_j}$, is used to determine the anisotropic Reynolds-stress $a_{ij} = \overline{u_i' u_j'} - \frac{2}{3}\overline{\rho} k \delta_{ij}$ with the relationship:

$$-\overline{\rho}\overline{u_i' u_j'} = 2\mu_t \overline{S}_{ij} - \frac{2}{3}\overline{\rho} k \delta_{ij}, \tag{2.18}$$

where the strain rate tensor, $\overline{S}_{ij} = \frac{1}{2}\left(\frac{\partial \overline{u}_i}{\partial x_j} + \frac{\partial \overline{u}_j}{\partial x_i}\right) - \frac{1}{3}\frac{\partial \overline{u}_l}{\partial x_l}\delta_{ij}$ and $k = \frac{1}{2}\overline{u_i' u_j'}$.

The turbulent viscosity is given by:

$$\mu_t = C\rho\vartheta\ell, \tag{2.19}$$

where C is a dimensionless constant, ϑ is the turbulent velocity scale and ℓ is the length scale.

Models based on the turbulence viscosity hypothesis offer a convenient method to close the Navier-Stokes equations. The accuracy of the hypothesis ranges from high to low depending on flow type. A number of turbulence viscosity models have been proposed and fall into three groups: the algebraic model, the one-equation model and the two-equation model. The algebraic model is a zero-equation model meaning that it does not require the solution of any additional equations over the transport equations. This type of modeling can only be used in simpler flow geometries to obtain accurate results. One example of an algebraic model is the mixing length model. It relates the mixing length scale, l_m to the turbulent viscosity. The turbulent velocity scale for this model is:

$$\vartheta = c\ell \left|\frac{\partial \overline{u}_i}{\partial y}\right|. \tag{2.20}$$

The two constants c and C are absorbed into a new length scale, l_m, and the turbulent viscosity equation becomes:

$$\mu_t = \overline{\rho} l_m^2 \left|\frac{\partial \overline{u}_i}{\partial y}\right|. \tag{2.21}$$

The value of the mixing length is set in relation to the application. For example, for a two-dimensional boundary-layer flow, $l_m = \kappa y$, where κ is the von Karman's constant and y is the distance from the surface. Two examples of mixing length models include those developed by Baldwin and Lomax [15] and Cebeci and Smith [16].

The one-equation model solves for one turbulence transport equation, most often for the turbulent kinetic energy, k, as shown in Eq.(2.22).

$$\frac{\partial k}{\partial t} + \overline{u}_j \frac{\partial k}{\partial x_j} = \tau_{ij} \frac{\partial \overline{u}_i}{\partial x_j} - C_D \frac{k^{3/2}}{l_m} + \frac{\partial}{\partial x_j} \left[\left(\nu + \frac{\nu_t}{\sigma_k} \right) \frac{\partial k}{\partial x_j} \right], \tag{2.22}$$

where C_D is a model constant. Other common one-equation models include the Baldwin-Barth model [17] and the Spalart-Allmaras model [18].

This model has a higher accuracy than the zero-equation model. Kolmogorov [19] and Prandtl [20] independently suggested that an estimate of the turbulent viscosity be based on the value of turbulent kinetic energy. The turbulent viscosity scale is related to the turbulent kinetic energy as $\vartheta = k^{1/2}$ and the turbulent viscosity becomes:

$$\mu_t = \overline{\rho} c k^{1/2} l_m, \tag{2.23}$$

where the constant $c \approx 0.55$.

The two-equation model is the most commonly used model for turbulence in RANS based calculations. These type of models are complete and it is not necessary to specify flow-dependent variables. One of the most widely used models is the k-ε model developed by Jones and Launder [21]. It consists of two transport equations, one for the turbulent kinetic energy, k, and one for the turbulent dissipation rate, ε. The transport equations for k and ε are:

$$\frac{\partial \left(\overline{\rho} k \right)}{\partial t} + \frac{\partial}{\partial x_j} \left(\overline{\rho} k \overline{u}_j \right) = \frac{\partial}{\partial x_j} \left[\left(\mu + \frac{\mu_t}{\sigma_k} \right) \frac{\partial k}{\partial x_j} \right] + P + G - \overline{\rho} \varepsilon, \tag{2.24}$$

$$\frac{\partial \left(\overline{\rho} \varepsilon \right)}{\partial t} + \frac{\partial}{\partial x_j} \left(\overline{\rho} \varepsilon \overline{u}_j \right) = \frac{\partial}{\partial x_j} \left[\left(\mu + \frac{\mu_t}{\sigma_\varepsilon} \right) \frac{\partial \varepsilon}{\partial x_j} \right] + S_\varepsilon, \tag{2.25}$$

where P is the production of turbulent kinetic energy due to shear, G is the production of turbulence due to the buoyancy effect, S_ε is the source term in the dissipation equation and σ_k and σ_ε are model constants.

The turbulent viscosity is independent of the mixing length in this case and is dependent on k and ε. The velocity scale is defined as $\vartheta = k^{1/2}$ and the length scale is defined as $\ell = k^{3/2}/\varepsilon$. The turbulent viscosity becomes:

$$\mu_t = \overline{\rho} C_\mu \frac{k^2}{\varepsilon}, \tag{2.26}$$

where C_μ is a model constant.

Other k-ε models include the realizable k-ε model of Shih et al. [22] and the Re-Normalized Group method (RNG) method of Yakhot and Orszag [23]. Another two-equation model is the k-ω model, including Wilcox's k-ω model [24] and SST k-ω model of Menter [25].

Reynolds-stress models solve for the individual Reynolds stresses, $\overline{u_i' u_j'}$, and for the dissipation, ε, and thus does not require modeling the turbulent viscosity. In these models, the transport equation for the Reynolds stresses is:

$$\frac{\partial \overline{\rho}\overline{u_i' u_j'}}{\partial t} + \frac{\partial \overline{\rho}\overline{u_i' u_j'}\overline{u}_k}{\partial x_k} + \frac{\partial}{\partial x_k} T_{kij} = P_{ij} + R_{ij} - \overline{\rho}\varepsilon_{ij}, \tag{2.27}$$

where T_{kij} is the Reynolds stress flux, P_{ij} is the rate of production of Reynolds stress, R_{ij} is the pressure-rate-of-strain tensor and ε_{ij} is the dissipation tensor. They are expressed as:

$$T_{kij} = T_{kij}^{(u)} + T_{kij}^{(p)} + T_{kij}^{(\nu)}, \tag{2.28}$$

$$P_{ij} = -\overline{\rho}\left(\overline{u_i' u_k'}\frac{\partial \overline{u}_j'}{\partial x_k} + \overline{u_j' u_k'}\frac{\partial \overline{u}_i'}{\partial x_k}\right), \tag{2.29}$$

$$R_{ij} = \overline{p'\left(\frac{\partial u_i'}{\partial x_j} + \frac{\partial u_j'}{\partial x_i}\right)}, \tag{2.30}$$

$$\varepsilon_{ij} = 2\nu\overline{\frac{\partial u_i'}{\partial x_k}\frac{\partial u_j'}{\partial x_k}}, \tag{2.31}$$

where p' is the fluctuating pressure and $T_{kij}^{(u)}$, $T_{kij}^{(p)}$ and $T_{kij}^{(\nu)}$ are the flux of Reynolds stress due to turbulent convection, fluctuating pressure and diffusion respectively. They are defined as:

$$T_{kij}^{(u)} = \overline{\rho}\overline{u_i' u_j' u_k'}, \tag{2.32}$$

$$T_{kij}^{(p)} = \overline{u_i' p'}\delta_{jk} + \overline{u_j' p'}\delta_{ik}, \tag{2.33}$$

$$T_{kij}^{(\nu)} = -\mu\frac{\partial \overline{u_i' u_j'}}{\partial x_k}. \tag{2.34}$$

In principle this model offers great potential for accurate calculations but has not shown greater performance than the turbulence viscosity model because it is considerably more

complicated to implement. There are a total of seven equations which must be solved for the Reynolds stresses and turbulence dissipation in comparison to a maximum of two equations for the turbulence viscosity model. The large number of equations also increases the computational time. The computational cost of a Reynolds stress model can reach up to two times greater than a k-ε model [9].

The Algebraic Stress Model (ASM) is a simplified Reynolds stress model. It determines the Reynolds stresses as a function of k, ε and the mean velocity gradients and is used in conjunction with the k-ε turbulence model. By removing or modeling the convective and diffusive terms from the Reynolds stress equations, large amounts of computational cost can be saved. Modeling these terms reduces the Reynolds stress equations to a set of algebraic equations. The transport equation for ASM is:

$$\frac{\partial\left(\overline{\rho}\overline{u_i'u_j'}\right)}{\partial t}+\frac{\partial\overline{\rho}\overline{u_i'u_j'}\overline{u}_k}{\partial x_k}-\frac{\partial}{\partial x_k}\left(\frac{C_s\overline{\rho}k}{\varepsilon}\overline{u_k'u_l'}\frac{\partial}{\partial x_l}\overline{u_i'u_j'}\right)=P_{ij}+R_{ij}-\frac{2}{3}\overline{\rho}\varepsilon\delta_{ij}, \tag{2.35}$$

where C_s is the Smagorinsky constant.

2.3 Literature Review

In this section, the current state of research on numerical models of buoyant plumes is summarized focusing on the RANS and LES approaches described above. The RANS approach has been used frequently over the past to model the buoyant plume [26]. Various turbulence viscosity models have been tested in association with the RANS approach, including the Algebraic Reynolds Stress Model (ASM) [27, 28], ASM and k-ε hybrids [27, 29] and the k-ε turbulence model with various buoyancy modifications [2, 3, 26, 30, 31, 32, 33, 34, 35, 36] added through source terms in the turbulence equations. With recent advancement of computer technology, LES has become a more viable modeling approach for studying plume dynamics [6, 37, 38, 39, 40].

2.3.1 RANS simulation of buoyant plumes

A summary of the buoyancy modifications for the numerical models are listed in Table 2.1.

The RANS approach has been widely used for the modeling of buoyant plumes [26]. The k-ε turbulence model of Launder and Spalding [43] is commonly applied to close the Navier-Stokes equations [44]. This model remains popular due to its simplicity, numerical robustness and well-documented validation tests. However, well known deficiencies in the standard formulation of the model include the under prediction of the spreading rate of vertical thermal plumes and the over prediction of the spreading rate of horizontal stratified flows [30, 31].

To avoid the buoyancy deficiency of the standard k-ε model, ASM can be used. It has the potential to better model the buoyancy and rotational effects because it accounts for Reynolds stress anisotropy but is more computationally expensive than the k-ε model and has not been as widely validated [44].

Davidson [29] suggested a hybrid between the k-ε model and ASM. The non-isotropic Reynolds stress due to buoyancy is taken from the ASM and the remaining is modeled using the k-ε model with the Simple Gradient Diffusion Hypothesis (SGDH) used to model the production of turbulence due to buoyancy. Upon testing their model on a thermal plume, it was found that there was very little difference in predicted velocity and heat transfer rates between the k-ε model and the hybrid model. Use of the hybrid model increased the CPU time by only 3%.

Shabbir and Taulbee [28] tested the standard k-ε model with buoyancy modifications using SGDH and the ASM model separately on a thermal axisymmetric buoyant plume. Velocity and temperature results showed that the ASM performed just as well as the k-ε model but with added computational time. Similarly, Chow and Mok [27] tested four turbulence models, ASM, standard k-ε with the Generalized Gradient Diffusion Hypothesis (GGDH) buoyancy modifications of Daly and Harlow [45], Low Reynolds Number (LRN) k-ε and a hybrid k-ε and ASM model, in simulating compartment pool fires. Evaluation of the four turbulence models resulted in similar predictions for all cases, although the CPU

Table 2.1: Summary of buoyancy modifications

$S_\varepsilon = C_{1\varepsilon}\frac{\varepsilon}{k}P + C_{3\varepsilon}\frac{\varepsilon}{k}G - C_{2\varepsilon}\overline{\rho}\frac{\varepsilon^2}{k}$

Reference	R_f	$C_{3\varepsilon}$	G
Davidson [29]	-	1.44	$-\frac{\mu_t}{\sigma_t}\frac{1}{\overline{\rho}}\frac{\partial\overline{\rho}}{\partial x_j}g_j$
Shabbir and Taulbee [28]	-	1.44	$-\frac{\mu_t}{\sigma_t}\frac{1}{\overline{\rho}}\frac{\partial\overline{\rho}}{\partial x_j}g_j$
Chow and Mok [27]	-	1.44	$-\frac{3}{2}\frac{\mu_t}{\sigma_t\overline{\rho}k}\overline{u'_ju'_k}\frac{\partial\overline{\rho}}{\partial x_k}g_j$
Annarumma et al. [30]	-	1.44	$-\frac{\mu_t}{\sigma_t}\frac{1}{\overline{\rho}^2}\frac{\partial\overline{\rho}}{\partial x_j}\left(\frac{\partial\overline{p}}{\partial x_j}+\rho_\infty g_j\right)$
Nam and Bill [31]	-	1.44	$-\mu_t\frac{1}{\overline{\rho}}\frac{\partial\overline{\rho}}{\partial x_j}g_j$
Brescianini and Delichatsios [41]	-	1.0	$-\frac{\mu_t}{\sigma_t}\frac{1}{\overline{\rho}^2}\frac{\partial\overline{\rho}}{\partial x_j}\left(\frac{\partial\overline{p}}{\partial x_j}+\rho_\infty g_j\right)$ $-\frac{3}{2}\frac{\mu_t}{\sigma_t\overline{\rho}^2k}\left(\overline{u'_ju'_k}\frac{\partial\overline{\rho}}{\partial x_k}\right)\left(\frac{\partial\overline{p}}{\partial x_j}+\rho_\infty g_j\right)$

$S_\varepsilon = C_{1\varepsilon}\frac{\varepsilon}{k}\left(P+G\right)\left(1+C_{3\varepsilon}R_f\right) - C_{2\varepsilon}\overline{\rho}\frac{\varepsilon^2}{k}$

Reference	R_f	$C_{3\varepsilon}$	G
Markatos et al. [32]	$-\frac{G}{P+G}$	0.9	$-\frac{\mu_t}{\sigma_t}\frac{1}{\overline{\rho}}\frac{\partial\overline{\rho}}{\partial x_j}g_j$
Xue et al. [42]	Not Specified	0.8	$-\frac{\mu_t}{\sigma_t}\frac{1}{\overline{\rho}}\frac{\partial\overline{\rho}}{\partial x_j}g_j$
Yan and Holmstedt [33]	Not Specified	0.6	$-\frac{3}{2}\frac{\mu_t}{\sigma_t\overline{\rho}k}\overline{u'_ju'_k}\frac{\partial\overline{\rho}}{\partial x_k}g_j$
Worthy et al. [34]	$-\frac{G}{P+G}$	Varied	$-\frac{\mu_t}{\sigma_t}\frac{1}{\overline{\rho}}\frac{\partial\overline{\rho}}{\partial x_j}g_j$ $-\frac{3}{2}\frac{\mu_t}{\sigma_t\overline{\rho}k}\overline{u'_ju'_k}\frac{\partial\overline{\rho}}{\partial x_k}g_j$
Van Maele and Merci [26]	$-\frac{G}{P+G}$	0.8	$-\frac{\mu_t}{\sigma_t}\frac{1}{\overline{\rho}^2}\frac{\partial\overline{\rho}}{\partial x_j}\left(\frac{\partial\overline{p}}{\partial x_j}+\rho_\infty g_j\right)$ $-\frac{3}{2}\frac{\mu_t}{\sigma_t\overline{\rho}^2k}\left(\overline{u'_ju'_k}\frac{\partial\overline{\rho}}{\partial x_k}\right)\left(\frac{\partial\overline{p}}{\partial x_j}+\rho_\infty g_j\right)$

times required ranged from 6.3% to 29.5% greater than the k-ε model. Consequently, ASM is not often applied due to its higher computational cost.

The SGDH buoyancy modification has been a popular method by which to include the effect of buoyancy in the standard k-ε model. The buoyancy modification is added through the production of turbulence due to the buoyancy effect in the turbulent kinetic energy equation (Eq.(2.24)) and the source term in (Eq.(2.25)). Markatos et al. [32] modeled buoyancy-induced smoke flow in a two-dimensional enclosure. They found that the addition of the buoyancy modification did improve the realism of the predictions. The correct trends were captured when compared to the experimental data but the model results tended to over predict the depth of the hot layer within the enclosure. Ranging the buoyancy constant, $C_{3\varepsilon}$, between 0.3 and 1.0 had no discernible effect on the results. Convergence problems occurred when simulations were run with values of the buoyancy constant less than 0.3. Annarumma et al. [30] modeled a vertical turbulent diffusion flame, representative of a fire, applying SGDH to the k-ε turbulence model. Simulations for the axisymmetric flame over predict values of both axial velocity and temperature along the center axis while underestimating lateral spreading rates. These shortcomings were attributed to the model failing to reproduce the mechanism for generating the buoyant instability present in the flame in the transition from laminar to turbulent flow. Thus, the turbulent mixing predicted was unrealistically low.

Nam and Bill [31] recognized that the SGDH buoyancy modification tended to lead to over predicted centerline maximum values in axisymmetric plumes while under predicting spreading rates. Therefore, they suggested modifying two of the model constants in the SGDH buoyancy modification which most directly affect the diffusion of velocity and the temperature distribution. They argued that by increasing the viscosity coefficient, C_μ, this would directly increase the eddy viscosity, directly affecting the velocity profile to increase spreading rates. Similarly, the turbulent Prandtl number, σ_t, strongly impacts the temperature profile while having little affect on the velocity distribution. By lowering the turbulent Prandtl number, they determined that the temperature spreading rates would increase. These two quantities were varied until satisfactory results were obtained for test cases involving an axisymmetric plume generated by a pool fire and two sets of heptane-spray fire plumes. Further, the study was compared with plume correlations derived from

experimental results. The results of the modified constants in the k-ε model showed significant improvement in predicting the spreading rates and maximum values of both the velocity and temperature. The downside of this approach is that the general applicability of the model decreases when model constants are tuned to optimize for a particular test case.

Yan and Holmstedt [33] also recognized the deficiency of the SGDH in the k-ε model for simulating buoyant plumes. Therefore, they tested the GGDH buoyancy modification on both plane and axisymmetric thermal plumes and a buoyant diffusion flame. Upon comparing the results to those of the standard k-ε model and the experimental data, it was found that the standard k-ε model considerably under predicted spreading rates for both the thermal plumes and the diffusion flame. This is consistent with past results [30, 31]. The buoyancy modified model using the GGDH produced significant improvement in accuracy of temperature and velocity.

Following the work of Yan and Holmstedt [33], Worthy et al. [34] investigated the algebraic stress model used by Davidson [29] in addition to the standard k-ε model and implemented the SGDH and GGDH buoyancy modifications. The various models were applied to the planar plume of Chen et al. [35]. The SGDH modification created little difference to the velocity and temperature predictions when compared to the standard k-ε model in the self-preserving region. They concluded that the GGDH modification improved results significantly and that GGDH applied to the k-ε model presented the most accurate results. Further, the value of the buoyancy constant, $C_{3\varepsilon}$, varied depending on the experimental data and model used. Later, Sangras et al. [46, 47] and Dai et al. [48] produced experimental data for thermal buoyant plumes at larger distances downstream of the plume source than previously published. Their new results showed lower spreading rates in the self-preserving region than experiments undertaken in the past. They noted that previous experiments had extracted data in the self-preserving region leading to the possibility of inaccurate conclusions. Brescianini and Delichatsios [41] presented a study comparing the k-ε turbulence model with buoyancy models SGDH and GGDH and the ASM to the new buoyant plume data of Sangras et al. [46, 47] and Dai et al. [48]. Upon testing the standard k-ε turbulence model with the SGDH and GGDH buoyancy modifications as well as with the ASM on a number of turbulent buoyant jets and plumes they concluded that choice

of the most suitable buoyancy model was dependent on the set of experimental data to be modeled. None of the models tested accurately captured all the flow details of the velocity and temperature in both planar and axisymmetric flows. It was also concluded that there were no advantages to using the more complex ASM to model the planar and axisymmetric thermal buoyant plumes.

Van Maele and Merci [26] applied the standard and realizable k-ε turbulence models with the SGDH and GGDH buoyancy modification to an axisymmetric free plume and planar wall plume. The realizable model was developed by Shih et al. [22] and consisted of a new model dissipation rate equation and a new realizable eddy viscosity formulation. Simplifications were made to the terms used to model the production of turbulence due to the buoyancy, G. Pressure gradients were neglected. This assumption was found to have no impact on the results. The Boussinesq approximation, $\overline{\rho} \approx \rho_{\infty}$, was verified as appropriate for the SGDH buoyancy modification but had noticeable effect on the results obtained for velocity and temperature in the axisymmetric plume and plume concentration for the planar plume using the GGDH modification of the k-ε RANS formulation. The results for the axisymmetric plume model showed that the SGDH modification produced no noticeable changes from the results obtained using the standard k-ε model while applying GGDH in association with the standard and realizable k-ε model had a larger influence on the results. Overall, the realizable k-ε model with the GGDH buoyancy modification approach produced the most accurate results for the axisymmetric plume, producing good agreement with velocity and temperature results and with the the experimental data. In fact overall, all turbulent properties were well predicted. The standard k-ε model with the GGDH also produced good results. Similar conclusions were obtained for the planar plume.

2.3.2 LES simulation of buoyant plumes

McGrattan et al. [37] noted that because there are so many turbulence parameters required in CFD turbulence models, and that the values for these parameters appeared to vary for different applications, accuracy in the use of turbulence models to save computational cost

becomes case specific. Therefore, they attempted to use LES to directly simulate the large scale eddies and to idealize the effects of the small scales using a constant value of eddy viscosity. The experiment used for assessment of velocity and temperature predictions consisted of the examination of smoke movement in an enclosure fire. Results presented for the small-scale experiments were well predicted and coincided well with the experimental data and correlations given. Large-scale simulations were carried out but no results were provided. McGrattan et al. [37] concluded that a wide range of experiments could be modeled with reasonable accuracy using LES.

Ma and Quintiere [38] examined axisymmetric fire plumes attempting to extend the work of McGrattan et al. [37] from isolated fire plumes to unconfined fires. Using the LES approach, the standard Smagorinsky SGS model was applied with a default Smagorinsky constant value of $C_s = 0.2$. The test case considered consisted of an unconfined, free burning pool fire. Results showed that predicted flame heights matched well with values obtained using the flame height correlations. Good temperature and velocity predictions were obtained in the non-combustion regions but the temperature was over predicted near the burner surface.

An LES investigation of non-reacting turbulent buoyant jets was undertaken by Zhou et al. [39]. They recognized that much of the work on turbulent plumes had been focused on predictions of flow variables in the far-field self-preserving regions. The near-source region is where the laminar to turbulent flow transition takes place and where the large vortex structures form. These vortex structures lead to the puffing cycles observed in fire plumes [39] as well as break down to small scale vortices in the plume. Zhou et al. [39] studied thermal buoyant jets under various density ratios. Applying the Smagorinsky SGS model with a fixed Smagorinsky constant of $C_s = 0.1$ for the small scale eddies, results showed that the puffing cycle was well predicted in the near-source region, consistent with experimental data. The mean velocity along the centerline axis from the plume source indicated that the plume gas initially accelerates due to the buoyancy forces and then decelerates as turbulent mixing takes place. This initial acceleration is strongly dependent on the density ratio of the surrounding ambient air to the plume gas, ρ_∞/ρ_o. The density ratio also affects the spreading rates of the velocity and temperature. An increase in density ratio increases the spreading rates due to a perceived increase in turbulence intensity in

the flow.

Following their initial study on non-reacting turbulent buoyant jets, Zhou et al. [40] applied LES to reacting plumes. As in the non-reacting case, the reacting case showed the large vortex structures in the near-source region and the puffing cycles. The large vortices then broke down to the small-scale eddies following the transition from laminar to turbulent flow. The results were validated with experimental results [49] and axial velocity, temperature, species concentration and mixture fraction were well predicted.

With the experimental work of O'Hern et al. [4], DesJardin et al. [6] were able to study the near-field of a large turbulent helium plume. LES was conducted to determine plume instabilities and flow dynamics, including velocity components and plume concentration, as a function of grid resolution as well as how the results react with and without the use of the SGS model. The best results were obtained with the finest mesh and without the application of the SGS model. It was found that for buoyancy driven flows, the SGS model is not sufficient. Time averaged and rms values for the plume concentration were found to be significantly over predicted near the plume base and very sensitive to the grid resolution. Further, rms streamwise velocity error increased as the distance from the plume source increased.

2.4 Present Research

The studies mentioned in the previous section predominately focus on the self-preserving region and neglect to investigate how the models perform in the near source region of thermal buoyant plumes. It is necessary to study the near source region to ensure that the entire plume is accurately predicted. The objective of this work is to assess the capabilities of two different modeling approaches to investigate turbulent buoyant helium plumes in the near source region. First, several buoyancy-corrected k-ϵ models using the RANS approach are examined. The experimental planar wall plume of Sangras et al. [2, 3] is simulated in this study to ensure that the present modeling technique is correctly setup. The experimental results, including normalized radial velocity and helium mass fraction

profiles, are extracted in the self-preserving region. Numerical results for this plume are compared with those of Van Maele et al. [26] to ensure the results obtained are consistent with simulations where data is gathered in the self-preserving region. The model is then applied to simulate the experimental axisymmetric helium plume of O'Hern et al. [4] where data is gathered in the near-source region. Flow dynamics consisting of velocity and plume concentration are compared to experimental data to assess the accuracy of the model. Secondly, LES is applied to the same axisymmetric helium plume to determine if the LES approach is viable for the simulation of buoyant plumes. Various grid sizes are modeled to determine the sensitivity of the grid size on the results. Time averaged results, rms quantities and time dependent flow patterns are analyzed and compared to the experimental results [4] as well as to the numerical results of DesJardin et al. [6]. The Smagorinsky constant, C_s, is varied to understand how the modeled viscosity impacts the model. Experimental data for the axisymmetric plume of O'Hern et al. [4] can be found at [50].

2.5 Test Cases

In order to discuss the accuracy of the turbulence models, simple, representative and well documented experimental test cases must be selected. Simulations are run based on the parameters and specifications of these experimental test cases to validate the numerical model. The first case discussed consists of a planar turbulent wall plume where experimental data is extracted in the self-preserving region [2, 3]. This plume is chosen because the results available for this plume include both the velocity and helium mixture fraction normalized profiles. Further, it is the most recent experimental helium plume data available where results are extracted in the self-preserving region. The second case is an axisymmetric turbulent plume where experimental data is provided in the near-source region [4]. This experimental plume extends the body of research of buoyant plumes into the near-source region.

2.5.1 Planar Plume

A line source of buoyant gas located along the base of a flat wall is described as a planar turbulent wall plume. Turbulent wall plumes are classical examples of buoyant turbulent flow with application in confined natural convection processes and fires. Experimental testing of a planar wall plume was carried out by Sangras et al. [2, 3]. The objective of their work was to extend the study of turbulent round and free line plumes to plane turbulent wall plumes using similar methods.

The experiment setup consists of an enclosure 3.4 m by 2.0 m and 3.6 m high, depicted in Fig. 2.4. Porous side walls and ceiling are used to control room disturbances. The plume enters through a 9.4 mm wide, 876 mm long slot located at the bottom of the enclosure mounted flush to a flat floor. On the other side of the slot a vertical wall is mounted adjacent to the edge of the slot. This wall is mounted to a screen array, also to aid in controlling room disturbances. Laser-Induced Fluorescence (LIF) and Laser Velocimetry (LV) measurements are conducted to gather dataon the mixture fraction of the plume and fluid velocity respectively.

The plume source is a helium/air mixture at 29.0 Vol% helium, has a density of 0.871 kg/m^3 and enters through the slot at a normal velocity of 0.868 m/s. This corresponds to a Reynolds number of 740 and Froude number of 3.50. Fully developed conditions are established in the self-preserving region before data is gathered. The plume enters into still air with an ambient pressure of 99 $\pm$ 0.5 kPa and temperature of 297 $\pm$ 0.5 K. The experimental uncertainties associated with the measurements of streamwise velocity and mixture fraction are within 5% and 6% respectively. Measurements are taken in the fully developed region far from the source and the data is provided using self-preserving correlations. In this region, the effects of the source disturbances and momentum have dissipated ensuring that buoyancy is the dominating force in the gas movement.

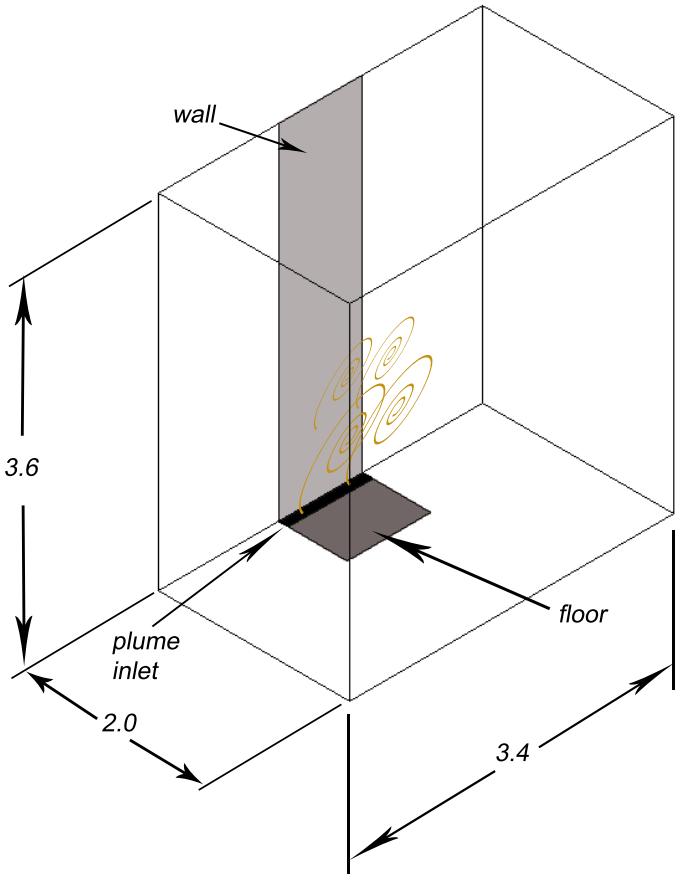

Figure 2.4: Experimental layout of the planar wall plume of Sangras et al. [2, 3] Dimensions in meters.

2.5.2 Axisymmetric Plume

The experimental study conducted by O'Hern et al. [4] was undertaken to extend existing studies of the behavior of buoyancy-dominated plumes to near-source regions. This was accomplished through the measurement of velocity and mass fraction in a large fully turbulent plume in the near-source region of the plume where the strongest buoyancy effect can be obtained.

Experiments were conducted at the Fire Laboratory for Accreditation of Models by Experimentation (FLAME) at Sandia National Laboratories in Albuquerque, New Mexico. The chamber used, shown in Fig. 2.5, is a 6.1 m cubical enclosure with a 2.3 m diameter chimney located on top of the chamber. Air enters the chamber through an annular air duct located 0.71 m above the facility floor. The air flow is straightened through a honeycomb apparatus to help maintain flow uniformity. The helium plume enters the chamber through a 1m diameter opening located 1.74 m above the air duct. This is surrounded by a 0.51 m platform to simulate the "ground plane" and causes the surrounding air to be drawn in radially. This setup simulates an unconfined plume within an enclosure with known boundary conditions. The elevation and planar schematics of the facility are displayed in Figs. 2.6 and 2.7 indicating the dimensions of the chamber layout.

In the experiment, air enters the chamber at an average normal velocity of 0.15 m/s $\pm 8\%$ at a temperature of $13^oC \pm 3^oC$. Acetone is added into the helium flow to be used as the fluorescent tracer gas at 1.7 vol%. As well, oxygen is added to the helium mixture at 1.9 vol% to quench the acetone phosphorescence. This results in a plume molecular weight of 5.45 g/mol. The plume gas enters the chamber at an average normal velocity of 0.325 m/s $\pm 2.6\%$ and a temperature of $11^oC \pm 3^oC$. The average mixture Reynolds number, $Re = D \cdot V_0/\nu$ is equal to 3200, where D is the plume source diameter, V_0 is the inlet velocity and ν is the kinematic viscosity of the mixture.

Data is gathered after initial transients have passed through the chamber and the experiment has reached a quasi-steady state. Experimental results are produced with a velocity uncertainty on the order of $\pm 20\%$ and plume concentration uncertainty on the order of $\pm 18\%$ plus a fixed offset of up to $\pm 5\%$. The turbulent statistics contain uncertainty

on the order of ±30% and the concentration fluctuations contain uncertainties on the order of ±21%.

PIV and PLIF measurements are performed to obtain the velocity and mass fraction data respectively over a two-dimensional field. PIV data are acquired at 200 frames per second and PLIF data are acquired at 100 frames per second for 7-8 seconds. Further details of the data acquisition techniques can be obtained in [4].

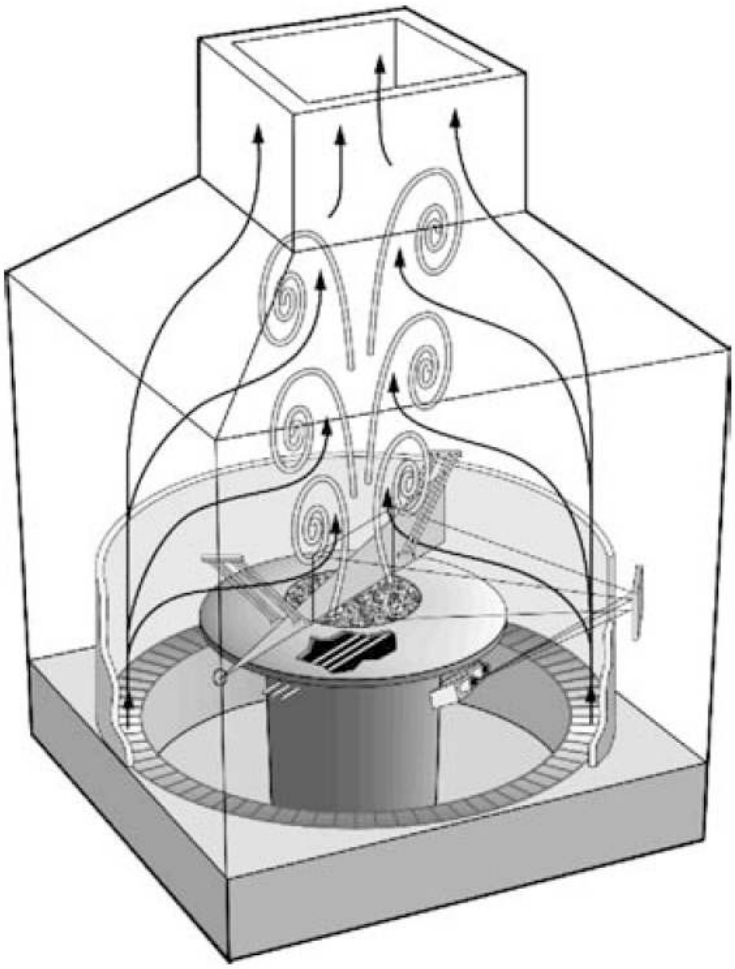

Figure 2.5: Schematic of set-up in FLAME facility. Facility details can be found in O'Hern et al. [4].

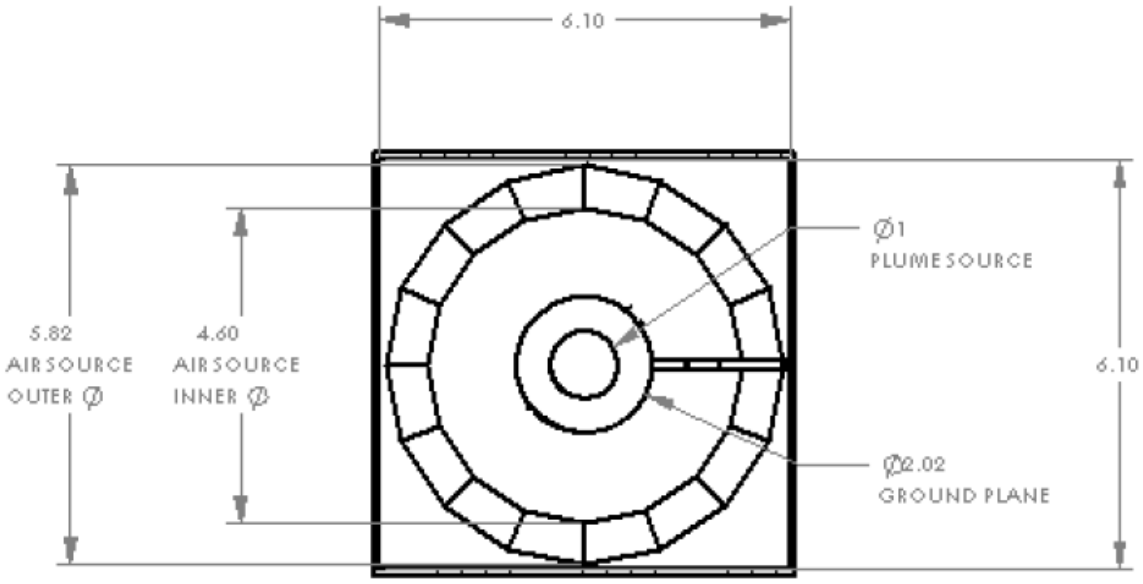

Figure 2.6: Horizontal view of FLAME facility. Dimensions in meters.

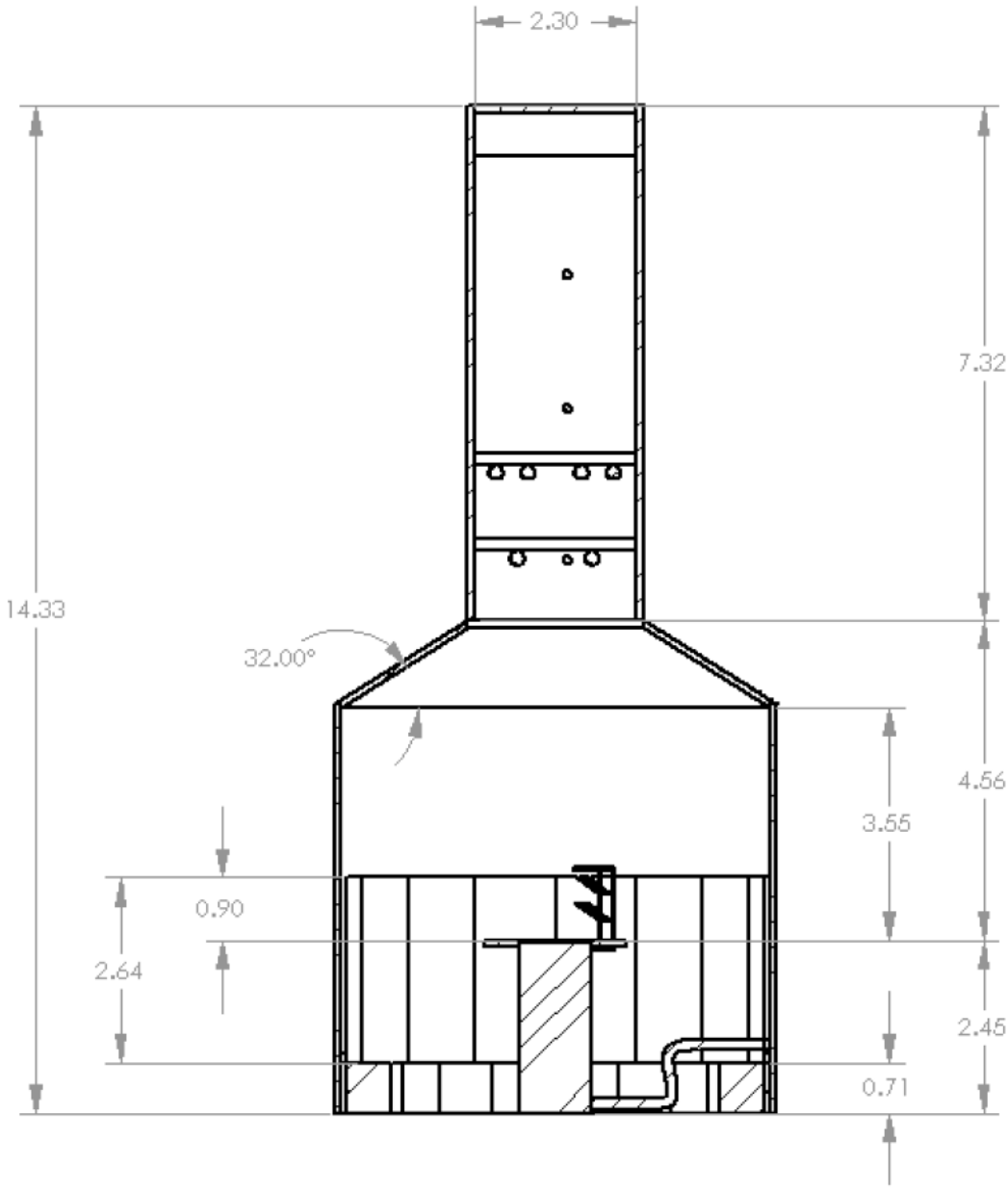

Figure 2.7: Elevation view of FLAME facility. Dimensions in meters.

Chapter 3

Reynolds Averaged Navier-Stokes Simulation

Most of the experimental work identified in Chapter 2 is performed on relatively small scales. Experimental techniques have been limited to gathering data far downstream from the plume source in the self-preserving region. This results in a high density ratio plume, where the density ratio is defined as the ratio of plume density to the ambient air density. Therefore previous numerical studies of the buoyant helium and thermal plume have been limited to these regions [4]. The experimental work of O'Hern et al. [4] extends the existing study of the behavior of buoyancy-dominated plumes to near-source regions. A numerical study using Reynolds Averaged Navier-Stokes (RANS) is performed on the experimental work of O'Hern et al. [4] to identify differences in modeling the near-source region from the far-source region.

In this chapter, buoyancy modifications are applied to the standard k-ε turbulence model and tested on two helium plumes. The first plume is the planar wall plume studied by Sangras et al. [2, 3]. This simulation is used as a benchmark to ensure results are consistent with those obtained in the past. The numerical results are compared to those of Van Maele et al. [26]. The second plume is that of O'Hern et al. [4]. No previous RANS calculations applying the Simple Gradient Diffusion Hypothesis (SGDH) and the

Generalized Gradient Diffusion Hypothesis (GGDH) of Daly and Harlow [45] have been reported on this plume.

Partial results of this chapter have been submitted to the Combustion Institute Canadian Section spring technical meeting [51, 52].

3.1 Governing Equations

Computational Fluid Dynamics (CFD) is based on the conservation laws of mass and momentum as well as the mean scalar quantities. The transport equations are:

$$\frac{\partial \rho}{\partial t} + \frac{\partial \left(\rho \overline{u}_j\right)}{\partial x_j} = 0, \tag{3.1}$$

$$\frac{\partial \left(\rho \overline{u}_i\right)}{\partial t} + \frac{\partial}{\partial x_j}\left(\rho \overline{u}_i \overline{u}_j + \rho \overline{u_i' u_j'}\right) = -\frac{\partial \overline{p}}{\partial x_i} + \frac{\partial \overline{\tau}_{ij}}{\partial x_j}, \tag{3.2}$$

$$\frac{\partial \rho \overline{\phi}}{\partial t} + \frac{\partial}{\partial x_j}\left(\rho \overline{u_j} \overline{\phi} + \rho \overline{u_j' \phi'}\right) = \frac{\partial}{\partial x_j}\left(\Gamma \frac{\partial \overline{\phi}}{\partial x_j}\right). \tag{3.3}$$

The mean viscous stress tensor component, $\overline{\tau}_{ij}$ is:

$$\overline{\tau}_{ij} = \mu \left(\frac{\partial \overline{u}_i}{\partial x_j} + \frac{\partial \overline{u}_j}{\partial x_i}\right). \tag{3.4}$$

The turbulent diffusivity hypothesis states that the Reynolds fluxes of a scalar are linearly related to the mean scalar gradient, thus:

$$-\rho \overline{u_j' \phi'} = \Gamma_t \frac{\partial \overline{\phi}}{\partial x_j}, \tag{3.5}$$

where the turbulent diffusivity, $\Gamma_t = \mu_t / \sigma_t$, μ_t is the eddy viscosity and the turbulent Prandtl number, $\sigma_t = 0.85$.

3.2 Turbulence Model

The standard $k-\varepsilon$ turbulence model of Launder and Spalding [43] is applied in this work. It is a two-equation model which solves for the turbulent kinetic energy, k, and the turbulent

dissipation rate, ε. The eddy viscosity is defined as:

$$\mu_t = \overline{\rho}\, C_\mu \frac{k^2}{\varepsilon}, \tag{3.6}$$

where $\overline{\rho}$ is the mean density and C_μ is a dimensionless constant equal to 0.9.

To model the Reynolds stresses in the momentum equation, an extended Boussinesq relationship is used to relate the Reynolds stresses to the mean strain rate:

$$-\overline{\rho}\overline{u_i' u_j'} = 2\mu_t \overline{S}_{ij} - \frac{2}{3}\overline{\rho} k \delta_{ij}, \tag{3.7}$$

where the strain rate tensor, $\overline{S}_{ij} = \frac{1}{2}\left(\frac{\partial \overline{u}_i}{\partial x_j} + \frac{\partial \overline{u}_j}{\partial x_i}\right) - \frac{1}{3}\frac{\partial \overline{u}_l}{\partial x_l}\delta_{ij}$ and $k = \frac{1}{2}\overline{u_i' u_j'}$.
The steady transport equations for k and ε are:

$$\frac{\partial}{\partial x_j}\left(\overline{\rho} k \overline{u}_j\right) = \frac{\partial}{\partial x_j}\left[\left(\mu + \frac{\mu_t}{\sigma_k}\right)\frac{\partial k}{\partial x_j}\right] + P + G - \overline{\rho}\varepsilon, \tag{3.8}$$

$$\frac{\partial}{\partial x_j}\left(\overline{\rho} \varepsilon \overline{u}_j\right) = \frac{\partial}{\partial x_j}\left[\left(\mu + \frac{\mu_t}{\sigma_\varepsilon}\right)\frac{\partial \varepsilon}{\partial x_j}\right] + C_{1\varepsilon}\frac{\varepsilon}{k}P - C_{2\varepsilon}\overline{\rho}\frac{\varepsilon^2}{k} + S_{\varepsilon B}, \tag{3.9}$$

where $\overline{u}$ is the time averaged velocity, μ is the molecular viscosity and P is the production of turbulent kinetic energy due to shear. It is expressed as:

$$P = -\overline{\rho}\overline{u_i' u_j'}\left(\frac{\partial \overline{u}_i}{\partial x_j}\right). \tag{3.10}$$

G is the production of turbulence due to the buoyancy effect. It represents an exchange between turbulent kinetic energy, k, and the potential energy. The source term, $S_{\varepsilon B}$, models the effect of buoyancy on the turbulent dissipation rate. Buoyancy modifications are added to the dissipation equation through the source term, $S_{\varepsilon B}$. The default values for the constants are as follows: $C_{1\varepsilon} = 1.44$, $C_{2\varepsilon} = 1.92$, $\sigma_k = 1.0$ and $\sigma_\varepsilon = 1.3$ [21].

3.3 Buoyancy Modifications

Buoyancy forces due to density differentials are the driving force in the flow of the two helium plumes considered in this study. Buoyancy is incorporated in the turbulence model

by the addition of the source term to the turbulent dissipation equation (Eq.(3.9)) as well as the production of turbulence due to the buoyancy effect, G, in the kinetic energy equation (Eq.(3.8)). In this study, three buoyancy modifications are implemented to assess the capabilities of modeling the buoyant helium plume. The buoyancy modifications to be implemented include the default CFX model, SGDH and GGDH.

Rodi [53] suggested the modified ε-equation:

$$\frac{\partial}{\partial x_j}\left(\overline{\rho}\varepsilon\overline{u}_j\right) = \frac{\partial}{\partial x_j}\left[\left(\mu + \frac{\mu_t}{\sigma_\varepsilon}\right)\frac{\partial \varepsilon}{\partial x_j}\right] + C_{1\varepsilon}\frac{\varepsilon}{k}\left(P+G\right)\left(1+C_{3\varepsilon}R_f\right)C_{2\varepsilon}\overline{\rho}\frac{\varepsilon^2}{k}, \tag{3.11}$$

where R_f is the flux Richardson number. The flux Richardson number is the ratio of the rate of removal of energy by buoyancy to its production by shear and is expressed as, $R_f = -G/P$. An alternative definition and one that is now taken as the standard is given by Rodi as $R_f = -G/\left(P+G\right)$ [53]. Using this alternate form of the flux Richardson number, the source term for the SGDH and GGDH model becomes:

$$S_{\varepsilon B} = C_{1\varepsilon}\left(1 - C_{3\varepsilon}\right)\frac{\varepsilon}{k}G, \tag{3.12}$$

where $C_{3\varepsilon}$ is the buoyancy constant. The equations for G in the SGDH and GGDH model are shown in Eq.(3.13) and (3.14) respectively.

$$G = -\frac{\mu_t}{\sigma_t}\frac{1}{\overline{\rho}^2}\frac{\partial \overline{\rho}}{\partial x_j}\left(\frac{\partial \overline{p}}{\partial x_j} + \rho_\infty g_j\right), \tag{3.13}$$

$$G = -\frac{3}{2}\frac{\mu_t}{\sigma_t \overline{\rho}^2 k}\left(\overline{u_j' u_k'}\frac{\partial \overline{\rho}}{\partial x_k}\right)\left(\frac{\partial \overline{p}}{\partial x_j} + \rho_\infty g_j\right), \tag{3.14}$$

where $\overline{p}$ is the mean pressure, ρ_∞ is the reference density corresponding to the density of air in the free stream and g is the gravitational acceleration. The primary difference between the two models is the inclusion of the cross-stream density variation, $\partial\overline{\rho}/\partial x_k$, in GGDH, whereas the SGDH model only includes the streamwise density gradient for the vertical plume.

The turbulent normal stress tends to be poorly predicted using the k-ε turbulence model. Therefore, Van Maele et al. [26] recommend replacing the turbulent normal stresses $\overline{u_\alpha' u_\alpha'}$ by the turbulent kinetic energy k. They justified this by stating that the turbulent

normal fluctuations in the mean flow direction are approximately twice the magnitude of the other turbulent normal stress components. The experimental data of the axisymmetric plume [50] indicates that this is a good assumption near the plume source but away from the source within a radius of 0.15 m of the center axis the assumption fails. Convergence problems occurred when attempting to include the normal stresses and so the recommendation of Van Maele et al. [26] was included.

Similar to the thermal plumes numerically modeled in the past, Van Maele et al. [26] found their results insensitive to the value of $C_{3\varepsilon}$ between 0.3 and 1.0. In the present study, values ranging from 0 to 1 are tested.

In Ansys CFX, the production of turbulence due to the buoyancy effect, G, and the source term for the ε-equation, $S_{\varepsilon B}$, are:

$$S_{\varepsilon B} = C_{1\varepsilon} C_3 \frac{\varepsilon}{k} \max(0, G), \tag{3.15}$$

$$G = -\frac{\mu_t}{\overline{\rho}\sigma_\rho} \frac{\partial \overline{\rho}}{\partial x_j} g_j. \tag{3.16}$$

where C_3 and σ_ρ are model constants, both having a default value of 1.0 for the full buoyancy model. Thus, the default CFX buoyancy-corrected k-ε model corresponds to Eq.(3.12) with $C_{3\varepsilon}$=0. The CFX buoyancy model is very similar to the SGDH model but with the addition of two assumptions. The CFX model assumes that the pressure gradient is negligible and that the reference density is equivalent to the fluid density. Assuming the pressure gradient is negligible is reasonable due to the fact that the plume velocity is relatively low creating low pressure gradients. The assumption that the reference density is equivalent to the fluid density is good for weaker plumes which have a low buoyancy effect but for stronger plumes, this assumption would act to lower the production of turbulence due to the buoyancy effect.

3.4 Computational Details

ANSYS ICEM CFD 10.0 was used to generate the mesh. ICEM was an ideal choice for the given problem. It has the capability of generating hexahedral meshes which works well

for the two-dimensional simulation. Mesh spacing and refinement can be easily defined by the user to create the desired mesh.

The RANS model is included in the general purpose commercial CFD package, ANSYS CFX-10.0 [54]. ANSYS-CFX is a fluid flow analysis and design application software. The software package is structured into three tools: pre-processing performed in CFX-Pre, the solver performed in CFX-Solver and post-processing performed in CFX-Post.

CFX-Pre is a versatile tool used for numerically modeling. Upon importing the desired mesh, the model parameters can be adjusted as desired. The various source terms are included in CFX by user CFX Expression Language (CEL) functions based on FORTRAN subroutines. Model parameters include the flow physics, boundary conditions and solver parameters. CFX-Solver uses a coupled solver to solve the governing equations (conservations of mass, momentum and scalar quantities), i.e. the governing equations are solved simultaneously rather than sequentially, as in a a segregated solver. Thus, this solution approach uses a fully implicit discretization of the equations at any given time step. It also reduces the number of iterations required to reach convergence for a steady state simulation. Ansys CFX uses a single cell, unstaggered, collocated grid to overcome the decoupling of pressure and/or velocity. The continuity equation is modeled using a second order central difference approximation to the first order derivative in velocity, modified by a fourth derivative in pressure. CFX-Post allows the user to import and view the results from the solver through a graphical user interface. Raw data can be readily exported at desired locations within the model domain [54].

For the planar plume, a two-dimensional grid is used extending 0.5 m in the cross-stream direction and 2.0 m in the streamwise direction. The mesh is designed to be refined in the location where mixing takes place. It consists of 4 equally spaced cells along the slot and 50 cells along the remainder of the cross-stream direction with a geometric spacing. There are 80 cells in the stream-wise direction also with a geometric spacing. This results in a total number of 4320 hexahedral cells in total. The geometric spacing is determined by specifying the number of cells desired and the first cell width, which in this case is set equal to the width of the cells which align to the slot spacing. A constant growth rate calculates the remaining cell spacing.

The layout of the domain and the placement of boundary conditions is similar to the experimental settings and is displayed in Fig. 3.1. The plume inlet velocity is uniform at 0.868 m/s and the helium/air mixture has a helium mass fraction of 0.053. Wall boundary conditions are placed at the floor and vertical wall with no-slip conditions applied. The side and top planes are defined as openings with static pressure boundary conditions imposed to allow flow in and out of the domain. Ambient conditions are set according to the experimental setup with a pressure of 99 kPa and temperature of 297 K.

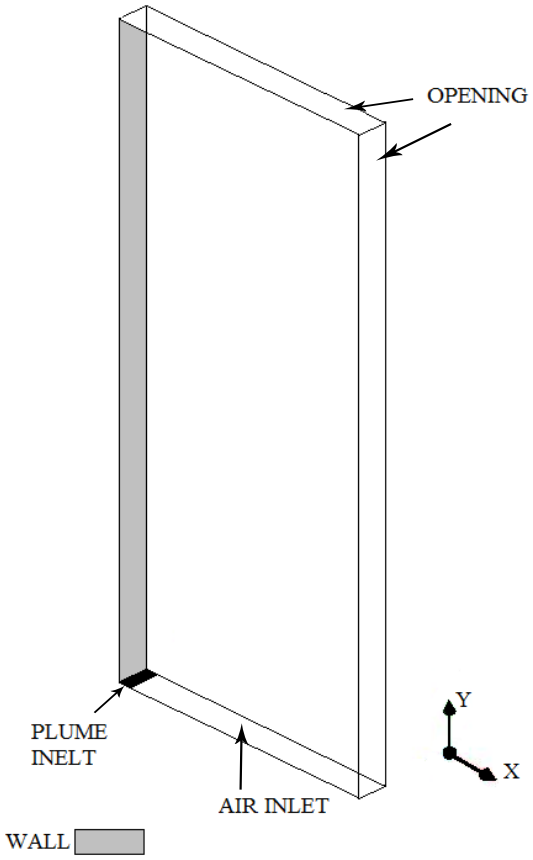

Figure 3.1: Layout and boundary conditions of the planar plume

To simulate the axisymmetric plume, it is not necessary to model the entire domain

of the experimental chamber. Due to symmetry, a five-degree slice of the chamber is considered. Calculations using the full three-dimensional domain were also performed and the difference in the results between the two computational domains was found to be negligible. The layout, grid spacing and spacing type along the slice is displayed in Fig. 3.2. The mesh is one node thick in the axial direction. Grid refinement takes place in the area of interest attempting to design the grid as uniform as possible near the plume source. The mesh consists of 22,882 hexahedral cells.

The setup of the plume inlet, platform surrounding the plume inlet as well as the air inlet are all accounted for according to the experimental details as shown in Fig. 3.3. A no slip condition is applied to all wall boundaries. A 5% turbulence intensity is set at all inlet boundary conditions. Nominal turbulence intensities range from 1-5%. Numerical results for the plume proved that varying the turbulence intensity at the inlet between these two values produces negligible effect. Static pressure opening boundaries allow flow to move freely in and out of the domain. The side and roof of the chamber are modeled as openings. The actual experimental enclosure indicates walls in these locations but convergence problems occured when these surfaces were specified as walls. The plume gas composition consists of helium, acetone and oxygen at concentrations of 0.71, 0.18 and 0.11 respectively. The plume gas enters the domain at the plume inlet with a uniform normal velocity profile equal to 0.325 m/s. The air inlet velocity profile is uniform at 0.15 m/s. The model domain is isothermal at a temperature of 284 K and atmospheric pressure is applied.

Mesh dependency tests show that the predicted velocities and plume concentrations are grid independent for both the planar and axisymmetric simulations. A high resolution advection scheme is applied for the solver. The advection scheme implemented is in the form:

$$\phi_{ip} = \phi_{up} + \beta \nabla \phi \cdot \Delta \vec{r}, \tag{3.17}$$

where ϕ_{ip} is the value at the integration point, ϕ_{up} is the value at the upwind node, β is the blending factor which can vary between 0 and 1, $\nabla\phi$ is the nodal gradient of the upwind node and $\vec{r}$ is the vector from the upwind node to the integration point. A varying blend factor is calculated depending on the type of flow to enforce boundedness. Simulations are

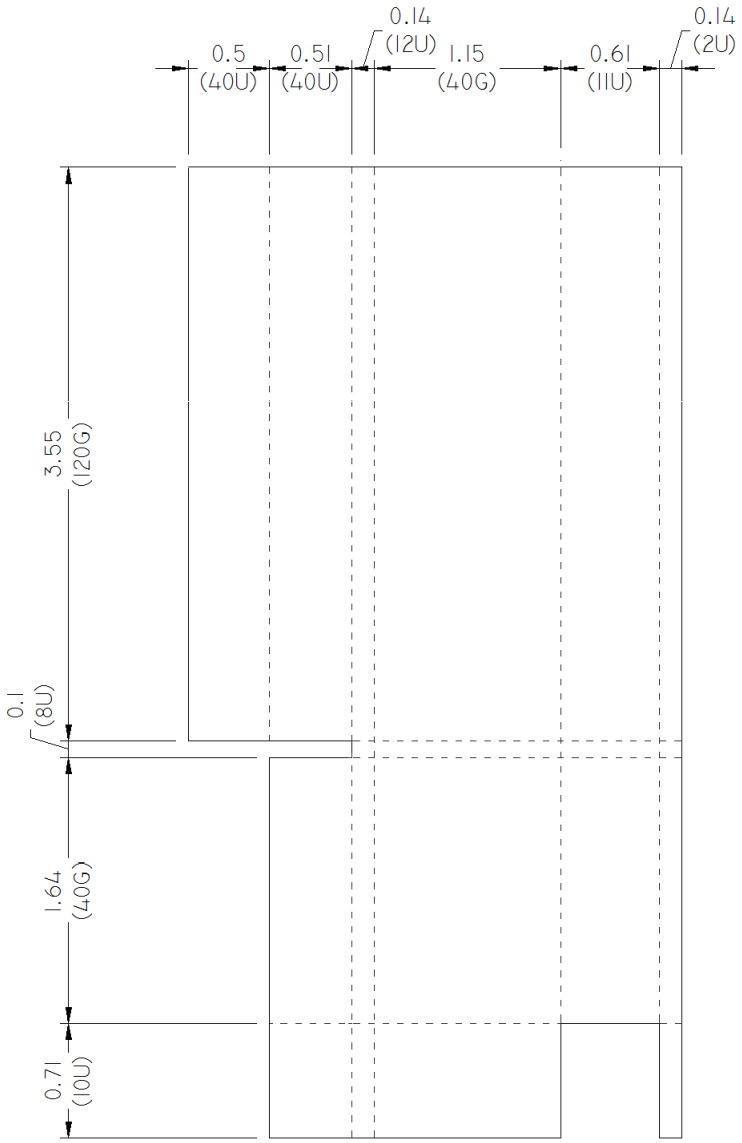

Figure 3.2: Dimensions, number of nodes and mesh spacing type for the plume chamber. Dimensions are in meters. Numbers in brackets represent the number of nodes within the specified spacing. Letters in brackets represent mesh spacing (U = uniform spacing, G = geometric).

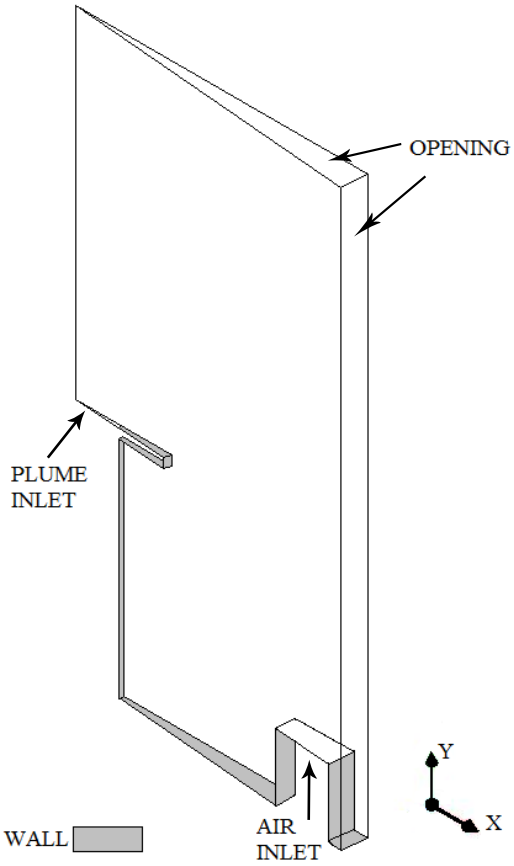

Figure 3.3: Boundary conditions for the axisymmetric plume.

run until all maximum residuals for the momentum, turbulence and species equations were less than 10^{-4}. Running the simulation until the maximum residuals were less than 10^{-5} did not show any visible differences in the velocity and plume concentration results.

The modified source terms for SGDH and GGDH are defined and implemented in CFX by user CFX Expression Language (CEL) functions based on FORTRAN subroutines. These are functions created by the user based on available variables existing in CFX.

3.5 Results

3.5.1 Planar plume

The results were taken sufficiently far downstream from the source to make use of the self-preserving correlations described in Sangras et al. [2, 3]. The self-preserving non-dimensional parameters, V(x/y) and F(x/y), and characteristic plume widths, l_v/y and l_f/y, for velocity and mass fraction respectively are calculated as:

$$V\left(x/y\right) = vB_o^{-1/3}, \tag{3.18}$$

$$F\left(x/y\right) = fgB_o^{-2/3}y\left|1-\rho_\infty/\rho_o\right|, \tag{3.19}$$

$$V\left(l_v/y\right) = e^{-1}V_{max}, \tag{3.20}$$

$$F\left(l_f/y\right) = e^{-1}F_{max}, \tag{3.21}$$

where x and y are the cross-stream and streamwise coordinates respectively, v is the streamwise velocity, B_o is the source buoyancy flux, f is the mixture fraction, g is gravity, ρ_∞ is the free stream air density and ρ_o is the source density.

In the self-preserving region, $f << 1$, the mixture fraction can be determined using the linearized state relationship for density [36]:

$$\rho = \rho_\infty + f\rho_\infty\left(1-\rho_\infty/\rho_o\right), \tag{3.22}$$

where ρ is the gas density. The source buoyancy flux, B_o, is a conserved scalar of the flow. For plane plumes with uniform source properties, it is defined as:

$$B_o = bv_o g\frac{\left|\rho_o-\rho_\infty\right|}{\rho_\infty}, \tag{3.23}$$

where b is the slot width and v_o is the source velocity [55].

Simulation for the planar plume using the SGDH and GGDH model were initially run using the buoyancy constant suggested by Van Maele et al. [26]. Normalized radial profiles of the velocity and mass fraction results using Eqs.(3.18 & 3.19) respectively are compared to the experimental data [2, 3] and numerical values of Van Maele et al. [26] (noted as 'VM'

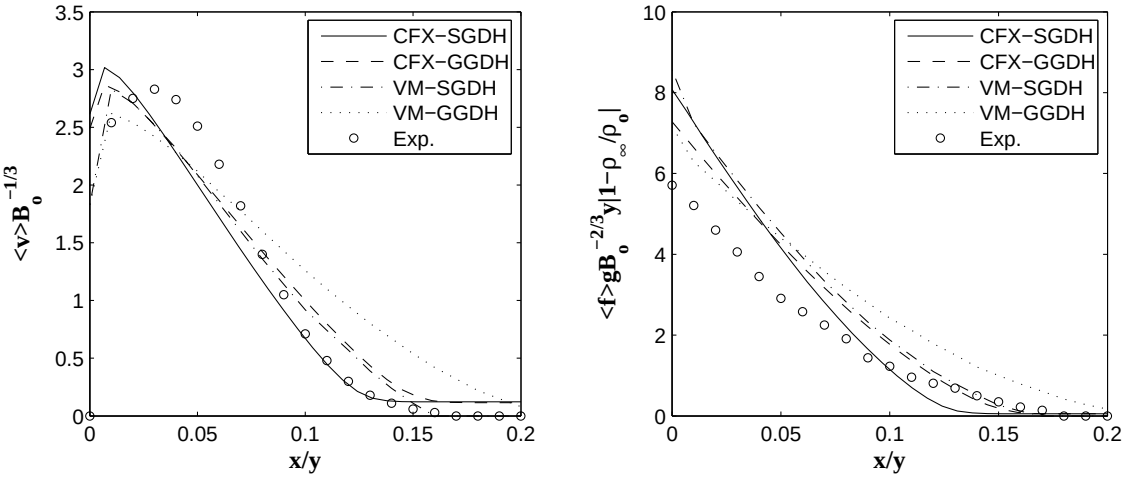

Figure 3.4: Comparison of normalized radial profiles of streamwise velocity and mixture fraction of CFX results with those of Van Maele et al. and experimental data. ($C_{3\varepsilon} = 0.8$)

in Fig. 3.4 and Table 3.1). Results are consistent with those of Van Maele et al. In the present work as in past results tested in the self-preserving region, a change of buoyancy model from SGDH to GGDH causes the spreading rate to increase and thus the maximum value decreases for both the streamwise velocity and mixture fraction. When compared to the experimental data, results produced fall outside the range of experimental uncertainty.

Further details are provided in Table 3.1 where values are taken at x/y=0.0125 following the experimental data. As shown in Table 3.1, the two models produce good results for the maximum normalized streamwise velocity. While the SGDH predicts a good spreading rate, the GGDH over predicts the experimental results by 21%. In both cases the maximum normalized mixture fraction is overestimated by up to 23.5%. Similar results were obtained by Van Maele et al. [26]. The peak values are determined best by the GGDH model and the spreading rates by the SGDH model in [26]. Although the maximum values and spreading rates of the present results are slightly different then those produced by Van Maele et al. [26], the trends in how the results of the SGDH model compare to those of the GGDH model are similar.

Table 3.1: Comparison of self-preserving data of the planar plume for $C_{3\varepsilon} = 0.8$

Model	V_{max} (m/s)	l_v/y (-)	F_{max} (-)	l_f/y (-)
Experiment	2.84±0.14	0.081±0.004	5.71±0.14	0.076±0.004
VM-SGDH	2.84	0.094	7.06	0.084
VM-GGDH	2.63	0.120	6.15	0.106
CFX-SGDH	2.95	0.083	7.05	0.073
CFX-GGDH	2.82	0.098	6.47	0.086
CFX-Default	2.95	0.083	7.07	0.073

A range of values for $C_{3\varepsilon}$ between 0 and 1 was tested. These results are displayed in Fig 3.5. The buoyancy constant had no impact on the results using SGDH while producing a slight variance in the results for the GGDH model. In the case of the GGDH model an increase in $C_{3\varepsilon}$ from 0 to 1 decreases the maximum streamwise velocity by 5.8% and the maximum mixture fraction by 10.4%. The low sensitivity to the buoyancy constant in this plume may be attributed to the relatively high density ratio, ρ_o/ρ_∞. In Eqs.(3.13 & 3.14), a high density ratio leads to a high mean density causing G to have less significance because it is relatively small in the turbulence equations in relation to P. Therefore, the impact of $C_{3\varepsilon}$ on the ε transport equation (Eq.(3.9)) remains small. The inclusion of the cross-density gradient in Eq.(3.14) leads to a greater production of turbulence due to buoyancy when compared to SGDH and therefore, varying the buoyancy constant for GGDH has a slight impact on the results. A higher buoyancy constant acts to decrease the accuracy of the velocity while increasing the accuracy of the mass fraction. Further, a lower buoyancy constant improves the velocity prediction while producing a worse prediction for the mass fraction.

3.5.2 Axisymmetric plume

Figures 3.6 and 3.7 display experimental and simulated values of cross-stream velocity, streamwise velocity, plume concentration and turbulent kinetic energy from results of the standard k-ε model with no buoyancy corrections of the axisymmetric plume of O'Hern et al. [4]. The gray shaded regions surrounding the experimental data represent the ex-

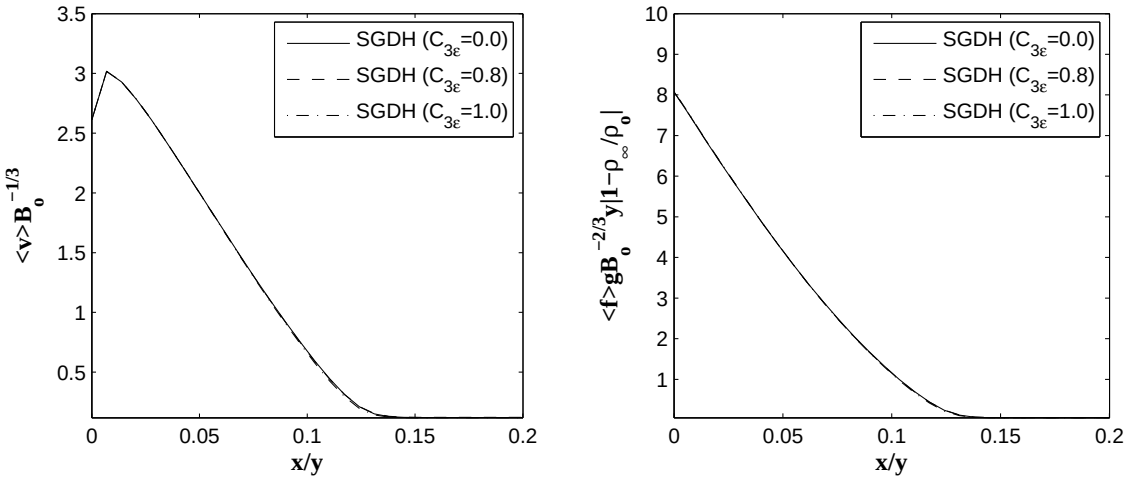

(a)

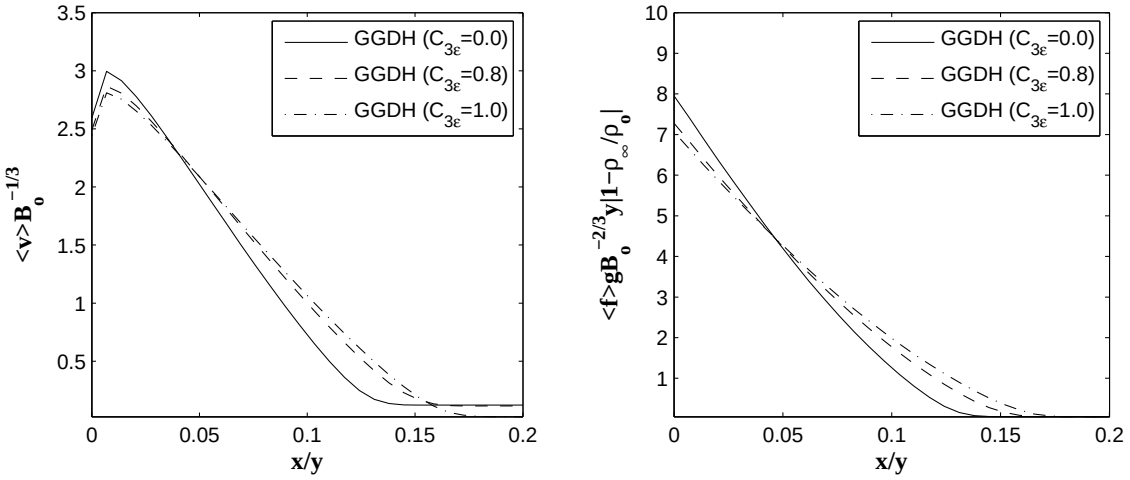

(b)

Figure 3.5: Normalized radial profiles of streamwise velocity and mixture fraction for various buoyancy constant values. (a) SGDH (b) GGDH.

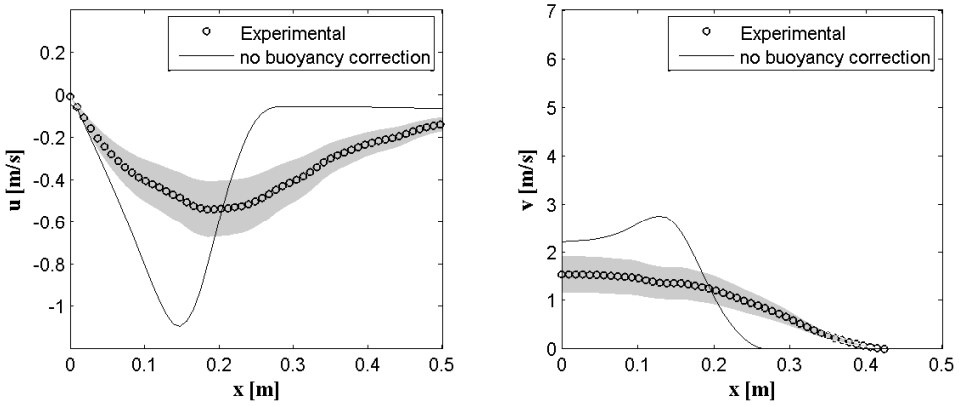

(a) y = 0.2 m

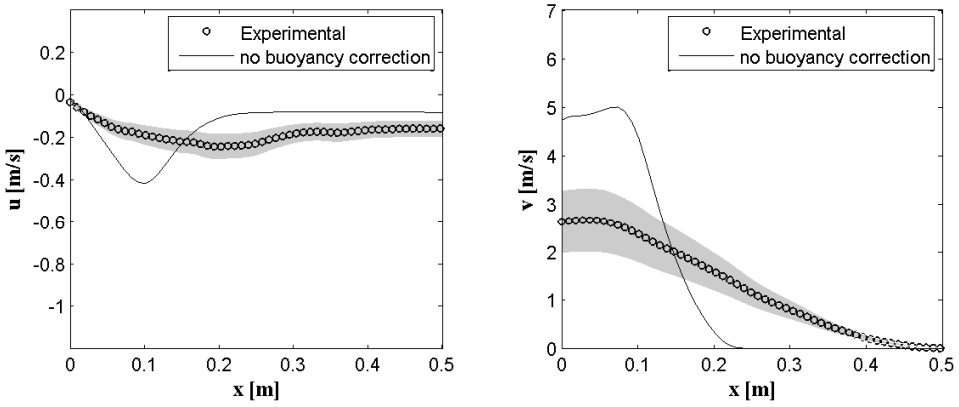

(b) y = 0.4 m

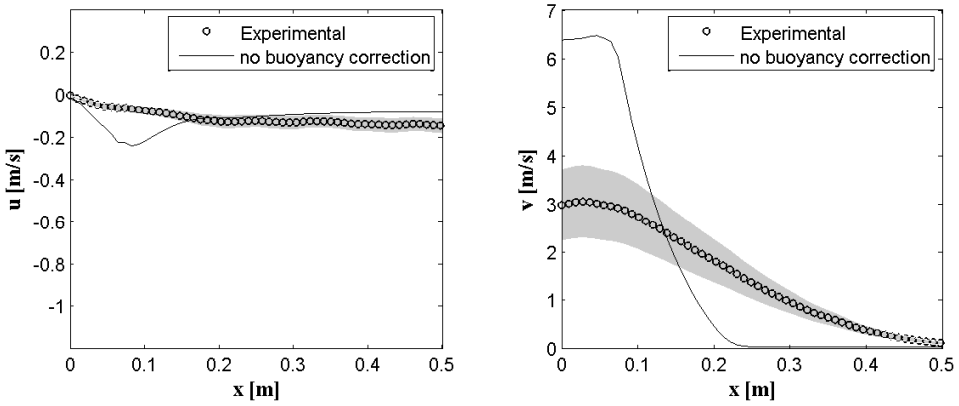

(c) y = 0.6 m

Figure 3.6: Cross-stream (left) and streamwise velocity (right) comparison of standard k-ε model with no buoyancy correction to experimental data.

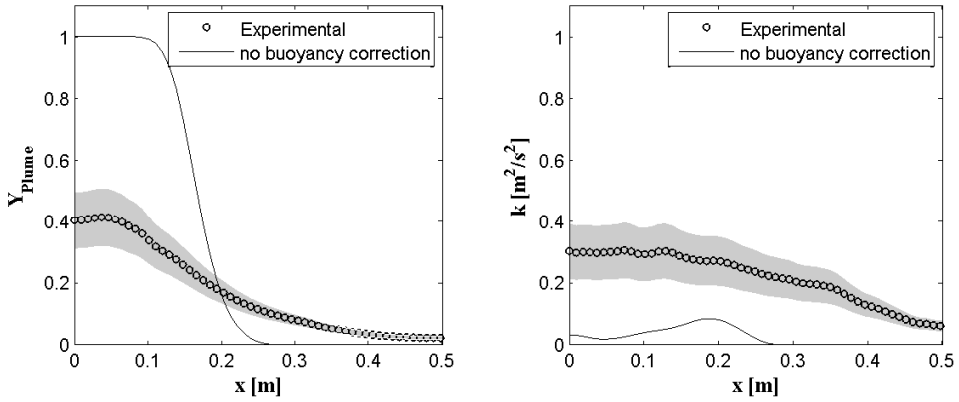

(a) y = 0.2 m

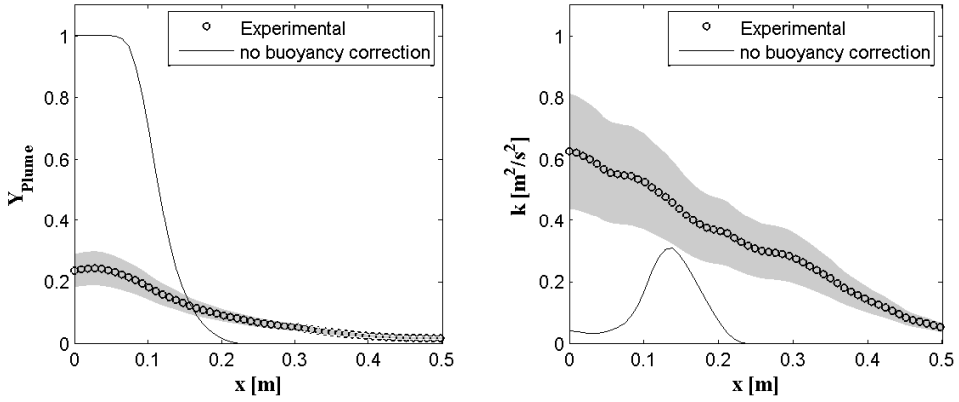

(b) y = 0.4 m

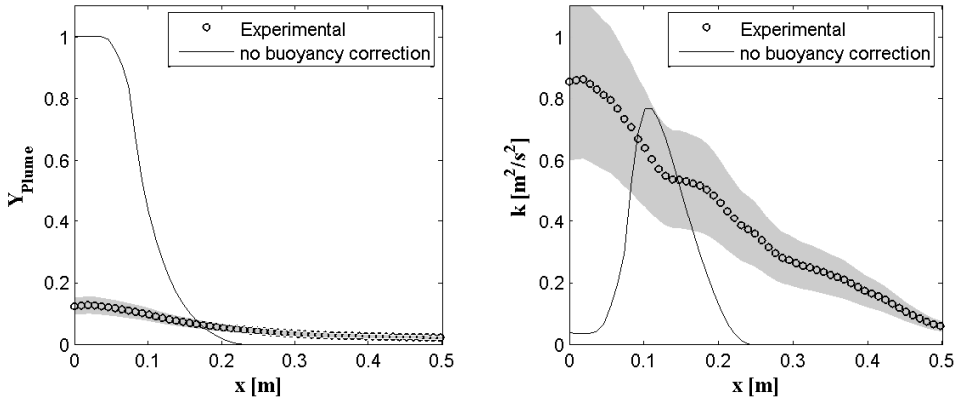

(c) y = 0.6 m

Figure 3.7: Plume concentration (left) and turbulent kinetic energy (right) comparison of standard k-ε model with no buoyancy correction to experimental data.

perimental uncertainty. The predictions based on the standard k-ε model agree with past findings of vertical thermal plumes [30, 31].

Near the plume source the cross-stream velocity displays a large entrainment into the plume. As the distance from the plume increases, the entrainment decreases. It should be noted that the location of the spike in the cross-stream velocity corresponds to the same location the decrease in the streamwise velocity occurs.

At all locations tested, the spreading rates in both streamwise velocity and plume concentration predicted using the numerical model are considerably less than those indicated by the experimental data. On the other hand the maximum values are over predicted in the simulated results. Figure 3.7 indicates that the centerline plume concentration is 1.0 at all tested locations. This centerline value is maintained up to approximately 0.9 m above the plume inlet. In the modeled results there is clearly insufficient account given for the actual mixing of the helium plume with the surrounding air, causing the plume to rise vertically without spreading horizontally.

The under prediction of the spreading rate of the streamwise velocity creates a thin shear layer in the region separating the plume from the surrounding air. This shear layer leads to an increase in turbulent kinetic energy at the plume-air interface which is evident in the turbulent kinetic energy plots in Fig. 3.7. Outside of this shear layer region in the surrounding air, the ambient air is quiescent. This acts to suppress the turbulent kinetic energy.

Figures 3.8, 3.9 and 3.10 show the results of varying the buoyancy constant for the CFX, SGDH and GGDH buoyancy models respectively. The C_3 value for the CFX model is tested over a range of 0 to 1. Similarly, the SGDH model is tested over a range of values of buoyancy constant, $C_{3\varepsilon}$, of 0 to 1. Convergence problems occurred in the GGDH model with values of the buoyancy constant over 0.6. Therefore, for the GGDH model, the buoyancy constant was tested over the range of 0 to 0.6.

Although the results displayed are for only one distance above the plume source inlet (y=0.4m) the trend in the variance of the buoyancy constant is comparable at all levels tested. Examining the three models, the range of possible velocity and plume concentration

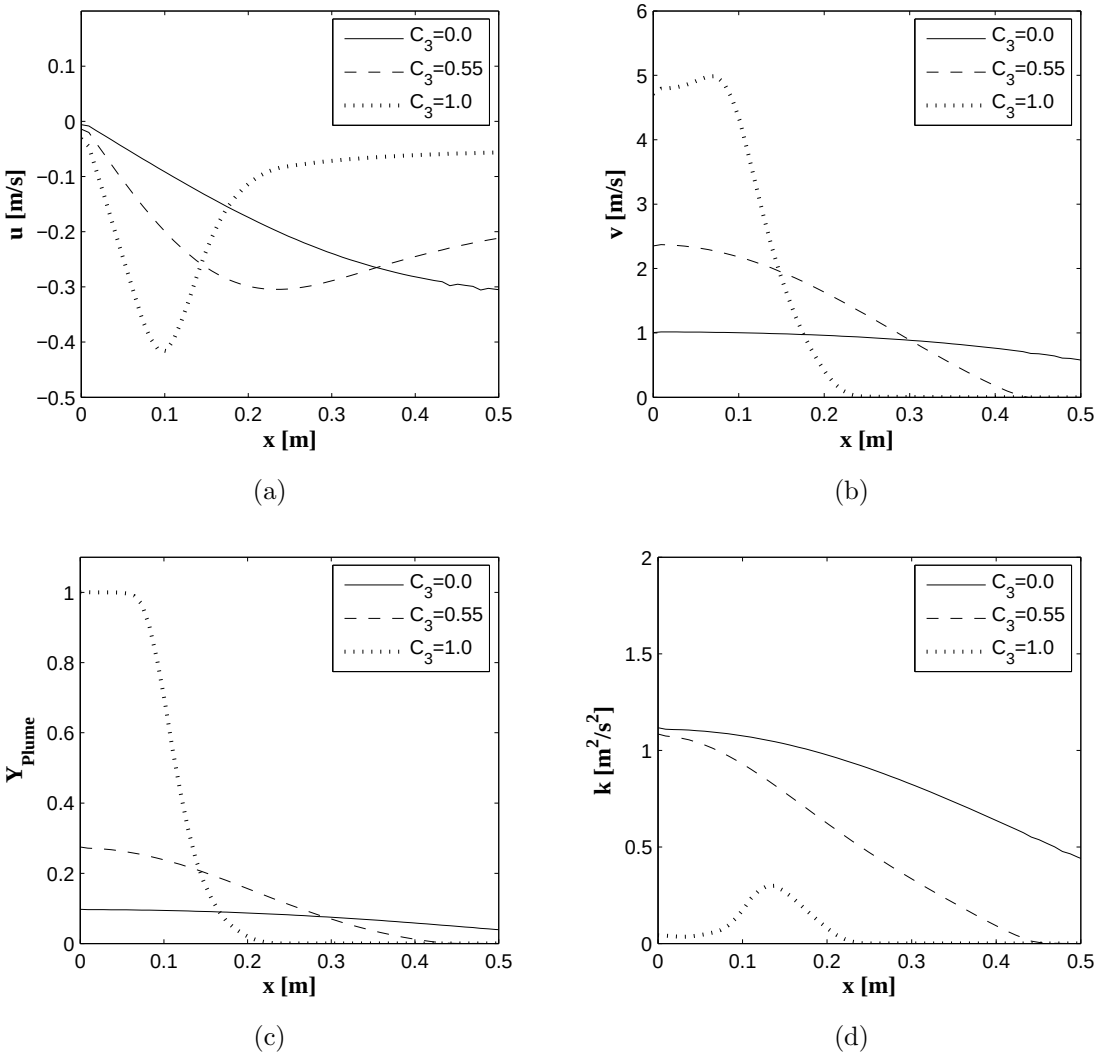

Figure 3.8: CFX buoyancy model results varying the buoyancy constant at y=0.4m. (a) cross-stream velocity (b) streamwise velocity (c) plume concentration (d) turbulent kinetic energy.

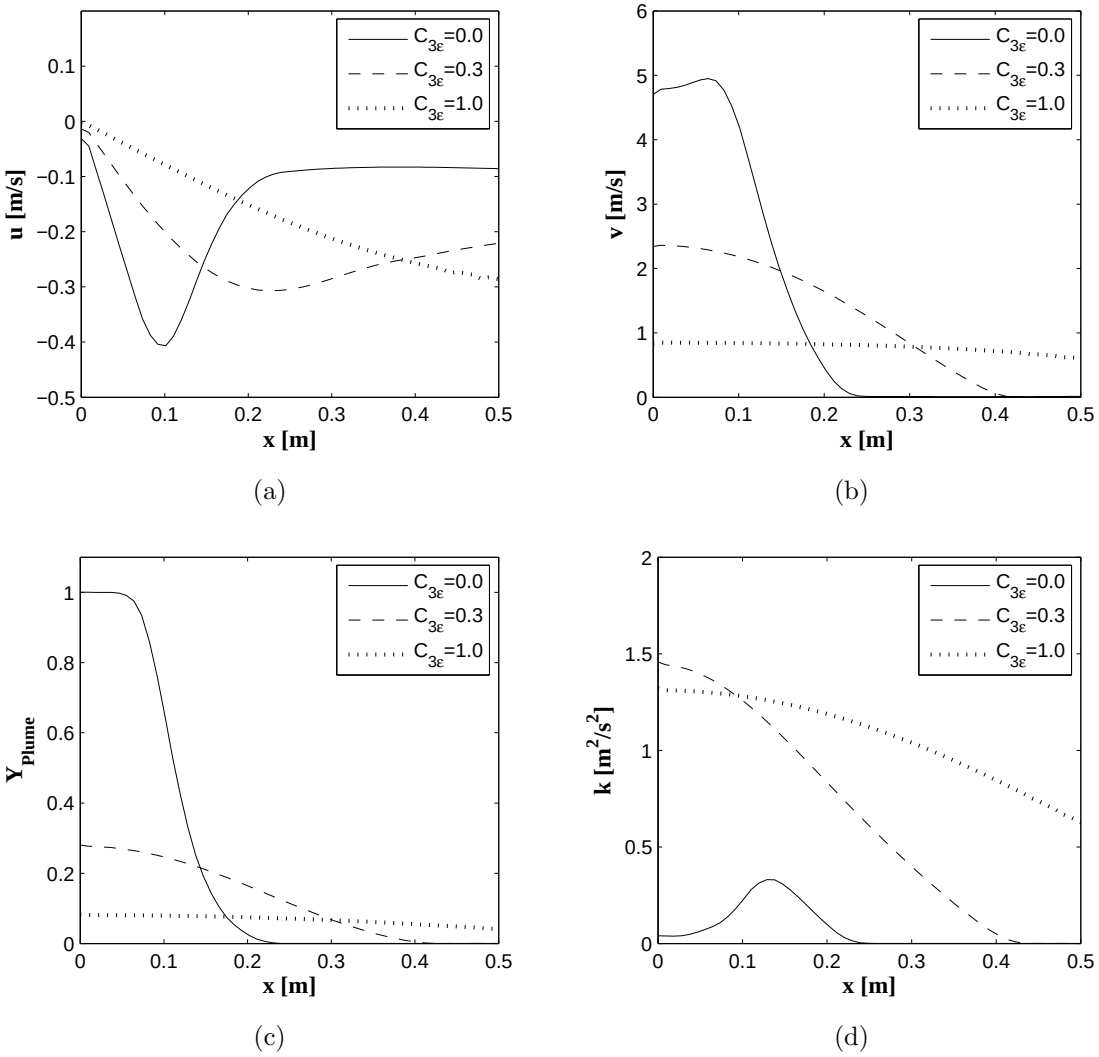

Figure 3.9: SGDH buoyancy model results varying the buoyancy constant at y=0.4m. (a) cross-stream velocity (b) streamwise velocity (c) plume concentration (d) turbulent kinetic energy.

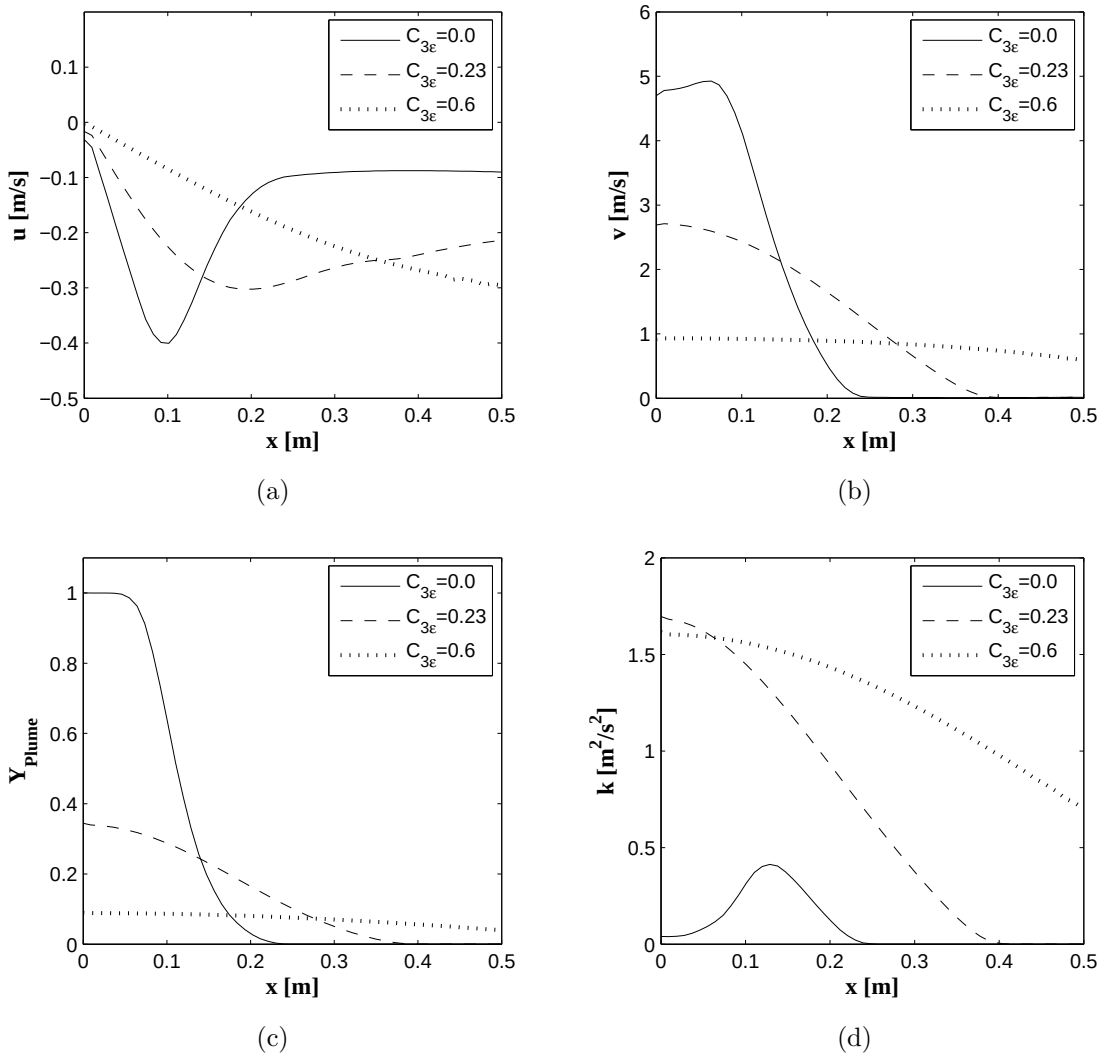

Figure 3.10: GGDH buoyancy model results varying the buoyancy constant at y=0.4m. (a) cross-stream velocity (b) streamwise velocity (c) plume concentration (d) turbulent kinetic energy.

results are similar for all three buoyancy models. The maximum streamwise velocity ranges from 0.85m/s to 4.99m/s and the peak plume concentration ranges from 0.08 to 1.0. This is in contrast to the results of the planar plume simulation and previous findings in the self-preserving region [28, 32, 34, 41]. In the self-preserving region, the results are independent of the buoyancy constant for the SGDH model and show little sensitivity for the GGDH model. As suggested in the discussion for the planar plume in Section 3.5.1 the sensitivity to the buoyancy constant in this case may be explained by the magnitude of the density ratio. The inlet helium concentration for the axisymmetric plume results in a density ratio of 0.182 which is much lower than the value for the planar plume which has a density ratio of 0.75. Further, because the data is gathered close to the source, little mixing has taken place and the low density ratio is maintained throughout the model domain. Equation (3.13) shows that a low density ratio results in a higher production of turbulent kinetic energy due to buoyancy, G. Therefore, the impact of G on the turbulence equations becomes more significant and thus small changes in the value of $C_{3\varepsilon}$ create a larger effect on the results. Although the CFX buoyancy model does not include this density ratio, a large value of G still exists relative to the plumes examined in the self-preserving region. This is due to the low density source gas creating a high density gradient. This effectively produces the same result as the other two models but on a different scale.

All three buoyancy models produce fairly similar results for maximum values and spreading rates of the plume concentration and streamwise velocity at the extreme values of the buoyancy constant shown in Table 3.2 keeping in mind that the turbulent dissipation source terms in Eqs.(3.12 & 3.15) for the buoyancy correction are such that a CFX buoyancy constant of C_3=1 corresponds to a SGDH and GGDH buoyancy constant of $C_{3\varepsilon}$=0. When C_3=1 for the CFX model, $C_{3\varepsilon}$=0 for the SGDH and GGDH model, the maximum plume concentration is equal to 1 for all three models and the maximum velocity ranges from 4.92 m/s in the GGDH model to 4.99 m/s in the CFX model. At the other extreme where C_3=0 for the CFX model, $C_{3\varepsilon}$=1 for the SGDH model and $C_{3\varepsilon}$=0.6 for the GGDH model, the maximum plume concentration ranges from 0.08 in the SGDH model to 0.10 in the CFX model and the maximum velocity ranges from 4.92 m/s in the GGDH to 4.99 m/s in the CFX model. Thus, the range of velocity and plume concentration results for extreme values of the buoyancy constant are similar.

Table 3.2: Maximum value and spreading rate comparison for the various buoyancy models at y=0.4m.

Buoyancy Model	Buoyancy Constant	$Y_{P,max}$ [-]	$x\,(Y_{P,max}/2)$ [m]	V_{max} [m/s]	$x\,(V_{max}/2)$ [m]	k_{max} $[m^2/s^2]$	$x\,(k_{max}/2)$ [m]
CFX	0.00	0.10	0.45	1.02	0.53	1.12	0.44
	0.55	0.27	0.22	2.37	0.26	1.08	0.23
	1.00	1.00	0.11	4.99	0.14	0.30	0.18
SGDH	0.00	1.00	0.11	4.95	0.14	0.33	0.18
	0.30	0.28	0.22	2.36	0.26	1.46	0.22
	1.00	0.08	0.50	0.85	0.63	1.32	0.49
GGDH	0.00	1.00	0.11	4.92	0.14	0.41	0.18
	0.23	0.34	0.19	2.71	0.23	1.70	0.21
	0.60	0.09	0.47	0.93	0.58	1.62	0.46

The difference in the three buoyancy models is evident in the turbulent kinetic energy profiles. The three models show similar trends but the results for the turbulent kinetic energy are predicted on different scales indicated by the varying maximum values and spreading rates. The various buoyancy models compared at similar buoyancy constants produce similar spreading rates. The maximum values on the other hand display a wider range between the models. This variation can be explained by the equations used for the production of turbulence due to the buoyancy effect, G, for the three models. The CFX model neglects the pressure gradient and assumes that the reference density is equal to the plume density as shown in Eq.(3.13). A negligible pressure gradient is a valid assumption because the pressure gradient is an order of magnitude less than the $\rho_\infty g_j$ term near the plume inlet and the pressure gradient decreases as the flow moves further from the inlet. The exclusion of the density ratio in the CFX model lowers the G value up to a factor of 5.6 compared to the SGDH model for this plume. This acts to lower the turbulent kinetic energy which explains the drop in k from the SGDH to CFX model. The exclusion of the cross-density gradient in Eq.(3.13) creates a lower G value for the SGDH model than the GGDH model. This explains the drop in k from the GGDH to SGDH model.

By varying the buoyancy constant for the three buoyancy models the results can be optimized to match the experimental data. The centerline streamwise velocity results for

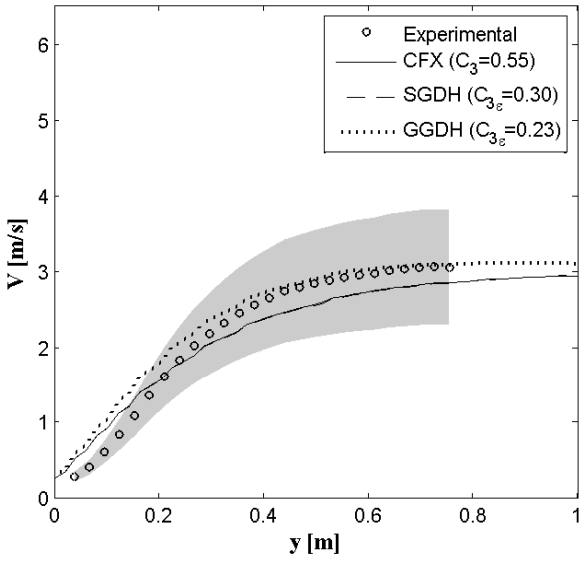

Figure 3.11: Centerline streamwise velocity comparison.

the three buoyancy models are compared with the experimental data in Fig. 3.11. The results for all three buoyancy models are within experimental uncertainty indicating that the transition from laminar-to-turbulent flow is well predicted.

Figures 3.12 and 3.13 display the radial profiles for the velocities, plume concentration and turbulent kinetic energy at various distances from the plume source. For the CFX and SGDH model, results presented are for a buoyancy constant equal to 0.55 and 0.30 respectively. These values correspond to the best agreement with the experimental data. The predicted results for the cross-stream velocity still captures the trend of the experimental data well near the plume source. As the value of the cross-stream velocity decreases so does the accuracy of the numerical results. Near the plume source the streamwise velocity profile follows closely to that of the experiment. At a larger distance from the plume inlet the velocity near the centerline begins to under predict the experimental data but is still within the range of experimental uncertainty. The plume concentration profiles show larger discrepancies. Good results are produced close to the plume inlet but differences increase

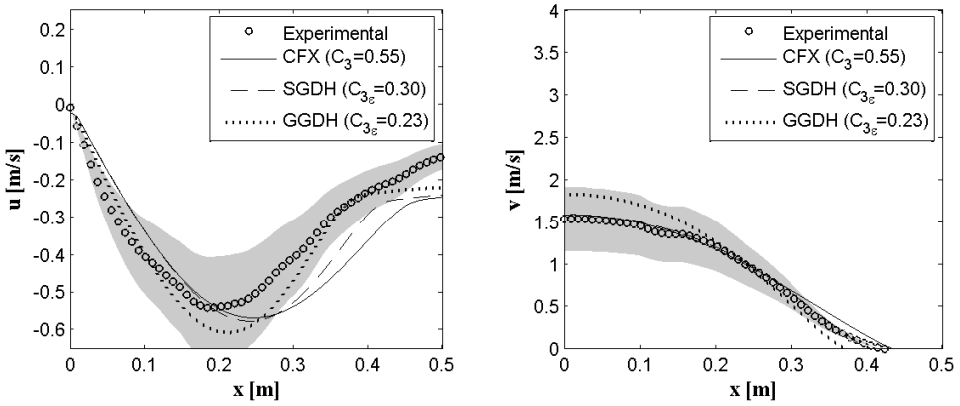

(a) y = 0.2 m

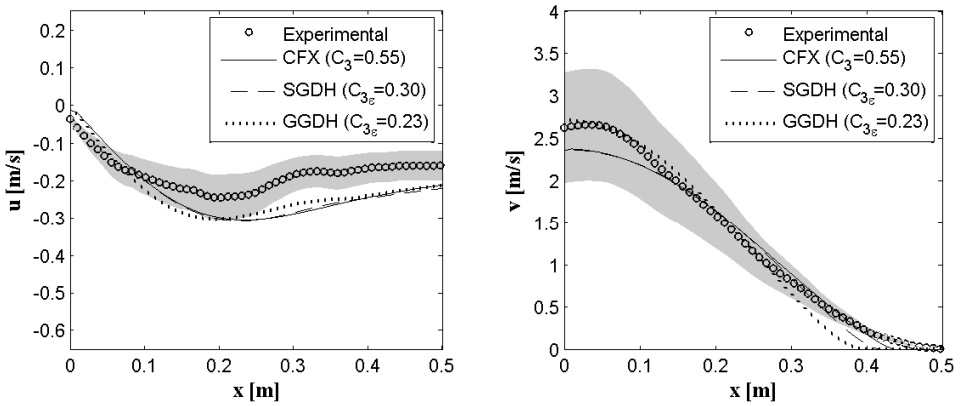

(b) y = 0.4 m

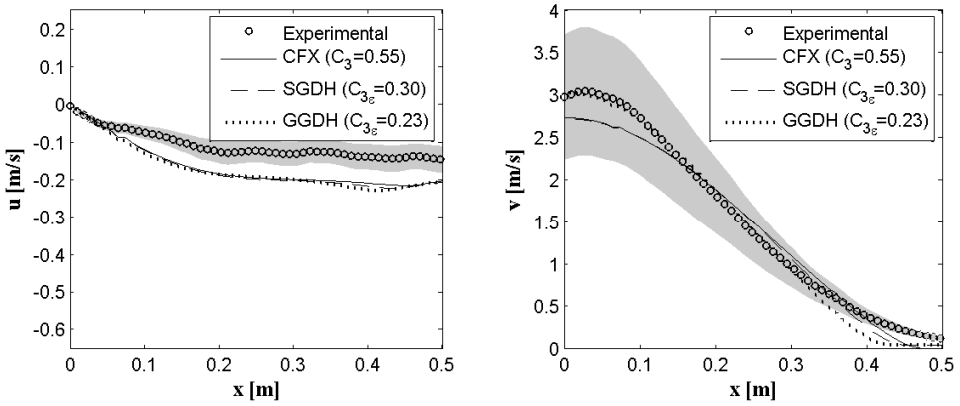

(c) y = 0.6 m

Figure 3.12: Cross-stream velocity (left) and streamwise velocity (right) comparison of k-ε model with variable $C_{3\varepsilon}$ to experimental data.

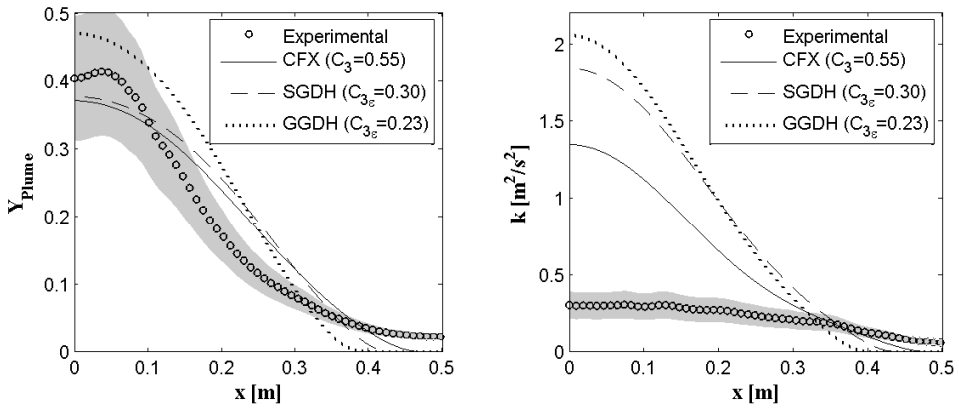

(a) y = 0.2 m

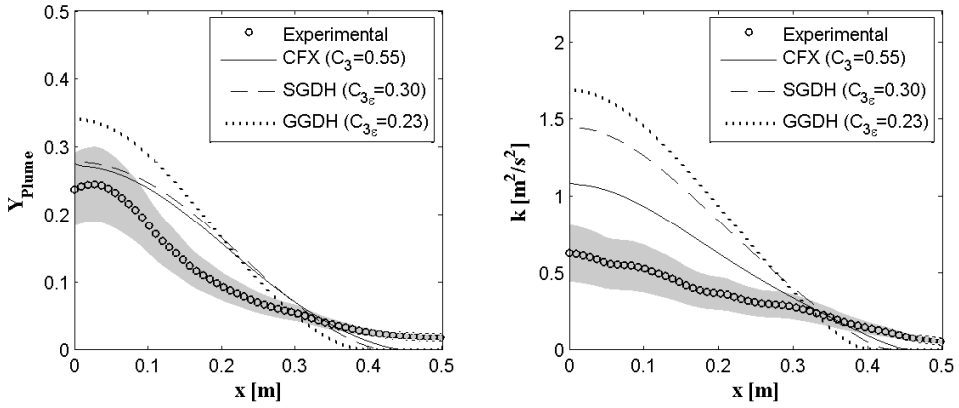

(b) y = 0.4 m

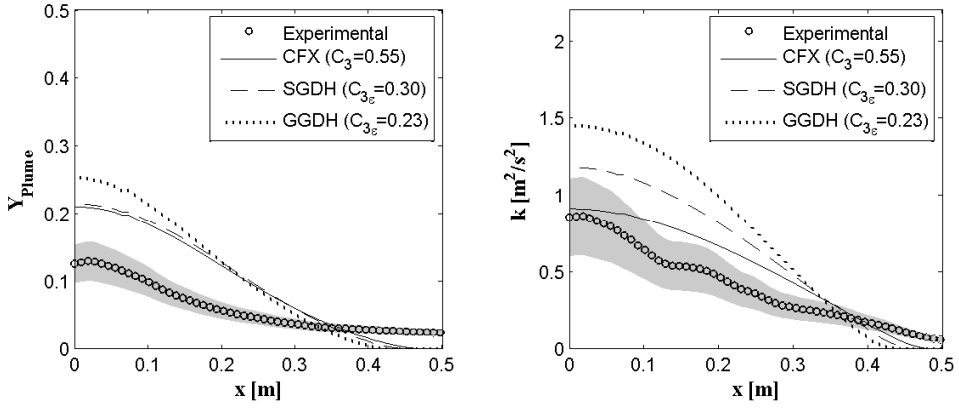

(c) y = 0.6 m

Figure 3.13: Plume concentration (left) and turbulent kinetic energy (right) comparison of k-ε model with variable $C_{3\varepsilon}$ to experimental data.

further away. However, in all regions there is a definite improvement over the standard k-ε model.

Good agreement with experimental data is obtained using $C_{3\varepsilon} = 0.23$ for the GGDH model. The cross-stream velocity results are similar to those for the CFX and SGDH models. The streamwise velocity profiles of the model match the experimental data very well. There is no visible improvement in results from GGDH over the SGDH model in the predictions of plume concentration. In order to include differential diffusion, molecular diffusion was added in the simulations but no significant change in the results was noticed.

For all models there is a large discrepancy between predicted and experimental values of turbulent kinetic energy. Further, the type of buoyancy model used in the simulation has a great impact on the k value due to its dependence on G. This is not evident in the velocity and plume concentration because the velocity and plume concentration are coupled with the two turbulence equations (Eqs.(3.8 & 3.9). The impact of the turbulent dissipation, ε, acts to balance out the changes in k.

3.6 Conclusions

The results for the planar plume are consistent with the simulations of Van Maele et al. [26]. Both the SGDH and GGDH show little or no sensitivity to the buoyancy constant, $C_{3\varepsilon}$, in the self-preserving region for this plume. Results showed that all maximum values and spreading rates for the SGDH model were within experimental uncertainty with the exception of the maximum mixture fraction. The GGDH model over predicted all maximum values and spreading rates except for the maximum velocity value. These simulations confirmed that for a high density ratio plume, the SGDH model has no dependence on the buoyancy constant, $C_{3\varepsilon}$, while $C_{3\varepsilon}$ has a slight impact on the GGDH model. The SGDH model proved to produce the most accurate results for this plume but the GGDH model allows for some variance in the results.

Good results are produced for the axisymmetric plume. At optimal values of $C_{3\varepsilon}$, the addition of buoyancy source terms via the CFX, SGDH and GGDH models presented

significant improvement over the standard k-ε model for both the streamwise velocity and plume concentration profiles. The CFX and SGDH model produced similar results. In the near source region, these two models demonstrated the best performance in plume concentration while the GGDH model produced the best results for the streamwise velocity. Unlike the planar plume in this study and plumes of the past where experimental data was gathered in the self-preserving region, these results were shown to be sensitive to the buoyancy constant. It is expected that the constant may have to be tuned depending on the conditions of the buoyant plume to be modeled.

An intermediate approach between DNS and RANS is LES. LES resolves the large scales of motion while modeling the small scales. It is a three-dimensional, time dependent modeling approach which can lead to a deeper insight into the plume dynamics. This modeling technique is applied to the axisymmetric buoyant helium plume. Results will be discussed in the following chapter.

Chapter 4

Large Eddy Simulation

The RANS calculations performed on the axisymmetric helium plume in Chapter 3 give insight into a few quantities such as the time averaged properties and mixing rates of velocity and plume concentration. To further investigate the movement of the helium plume, a three dimensional, time dependent study using the Large Eddy Simulation (LES) approach is undertaken. In addition to the averaged quantities, properties such as puffing cycles and rms quantities can be determined to provide further information into details of plume dynamics.

Partial results of this chapter have been submitted to the CFD Society of Canada [56].

4.1 Governing Equations

In LES the large scale components of a flow are resolved while those quantities that occur at length scales smaller than what can be resolved on the numerical grid must be modeled using a subgrid-scale (SGS) model. Using a SGS model, the effects of the smaller scale components, which have been modeled are applied to the resolved large scale components. A filter is used to determine the large scale components. Therefore, the filtered velocity is

defined as:

$$\overline{u}_i(x,t) = \int G(x,x')\, u_i(x',t)\, dx', \tag{4.1}$$

where $\overline{u}$ is the filtered velocity field and the localized function, $G(x,x')$, is the filter kernel. The velocity field can then be defined as:

$$u_i(x,t) = \overline{u}_i(x,t) + u'(x,t), \tag{4.2}$$

where $u'(x,t)$ is the residual field. The length scale, Δ, associated with the filter kernel determines the separation point between the large scales and the small scales. Eddies larger than Δ are resolved and eddies smaller than Δ are modeled.

The mass conservation equation does not change from the RANS formulation. With the inclusion of the filter, it remains as:

$$\frac{\partial \rho}{\partial t} + \frac{\partial(\rho \overline{u}_i)}{\partial x_i} = 0, \tag{4.3}$$

where ρ is the density. Filtering the Navier-Stokes equations gives:

$$\frac{\partial(\rho \overline{u}_i)}{\partial t} + \frac{\partial(\rho \overline{u_i u_j})}{\partial x_j} = -\frac{\partial \overline{p}}{\partial x_i} + \frac{\partial \overline{\tau}_{ij}}{\partial x_j}, \tag{4.4}$$

where $\overline{p}$ is the filtered pressure field. The mean viscous stress tensor component, $\overline{\tau}_{ij}$ is defined as a function of the turbulent viscosity and characteristic filtered rate of strain, $\overline{S}_{ij} = \frac{1}{2}\left(\frac{\partial \overline{u}_i}{\partial x_j} + \frac{\partial \overline{u}_j}{\partial x_i}\right)$:

$$\overline{\tau}_{ij} = -2\mu_t \overline{S}_{ij}. \tag{4.5}$$

The quantity $\overline{u_i u_j}$ is not easily computed and therefore a modeling approximation is used:

$$\tau^s_{ij} = \rho\left(\overline{u_i u_j} - \overline{u}_i \overline{u}_j\right), \tag{4.6}$$

where τ^s_{ij} is called the subgrid-scale Reynolds stress or simply subgrid-scale [57].

4.2 Numerical Details

The open source software Fire Dynamics Simulator (FDS) maintained at the National Institute of Standards and Technology (NIST) is used to model the axisymmetric plume.

FDS is a LES code with the ability to model fire-driven fluid flow as well as capable of modeling non-combustion situations. FDS solves the low-Mach number form of the Navier-Stokes equations which have been optimized for low-speed, buoyancy driven flows. This code neglects compressibility effects present in high-Mach number flows which require much smaller time steps and thus reduces the computational requirements of the simulation [58]. Convection and diffusion terms in the equations are approximated using second-order finite differences. Flow variables are updated in time on a three-dimensional, rectilinear grid using an explicit second order predictor-corrector scheme. An adaptive time step is used to allow for a faster convergence implementing the Courant-Friedrichs-Lewy (CFL) condition. This ensures that the solutions of the equations cannot be updated with a time step larger than that which allows a parcel of fluid to cross a grid cell [14].

The viscous stress tensor, in Eq.(4.5), is modeled in FDS using the Smagorinsky model [10]. Rather than using the actual fluid viscosity, the eddy viscosity is derived by dimensional arguments and is given by:

$$\mu_t = C_s^2 \rho \Delta^2 \left|\overline{S}\right|, \tag{4.7}$$

where C_s is an empirical constant. The default for this value in FDS is 0.20. Δ is the filter length scale on the order of the size of a grid cell and $\left|\overline{S}\right| = \left(2\overline{S}_{ij}\overline{S}_{ij}\right)^{1/2}$, is the magnitude of the large-scale strain-rate tensor.

Relative to RANS, LES is computationally expensive. A full three-dimensional model is required because flow variables are updated in time. This adds to the computational cost. To keep the LES model tractable then, the experimental setup described in Section 2.5.2 is simplified into a cubic enclosure. The computational setup is displayed in Fig. 4.1 and consists of a 4 m cubic domain.

The plume inlet is located at the center of the bottom plane. The air inlet surrounding the plume inlet creates a co-flow. FDS only allows for rectangular meshes. Thus the plume inlet in the computational domain, initially annular in the experiment, is made up of a group of square surfaces. The plume inlet is designed to keep the group of squares as circular as possible while attempting to match the area of the experimental plume inlet. It is not possible for the model plume inlet area to be equivalent to the experimental plume inlet

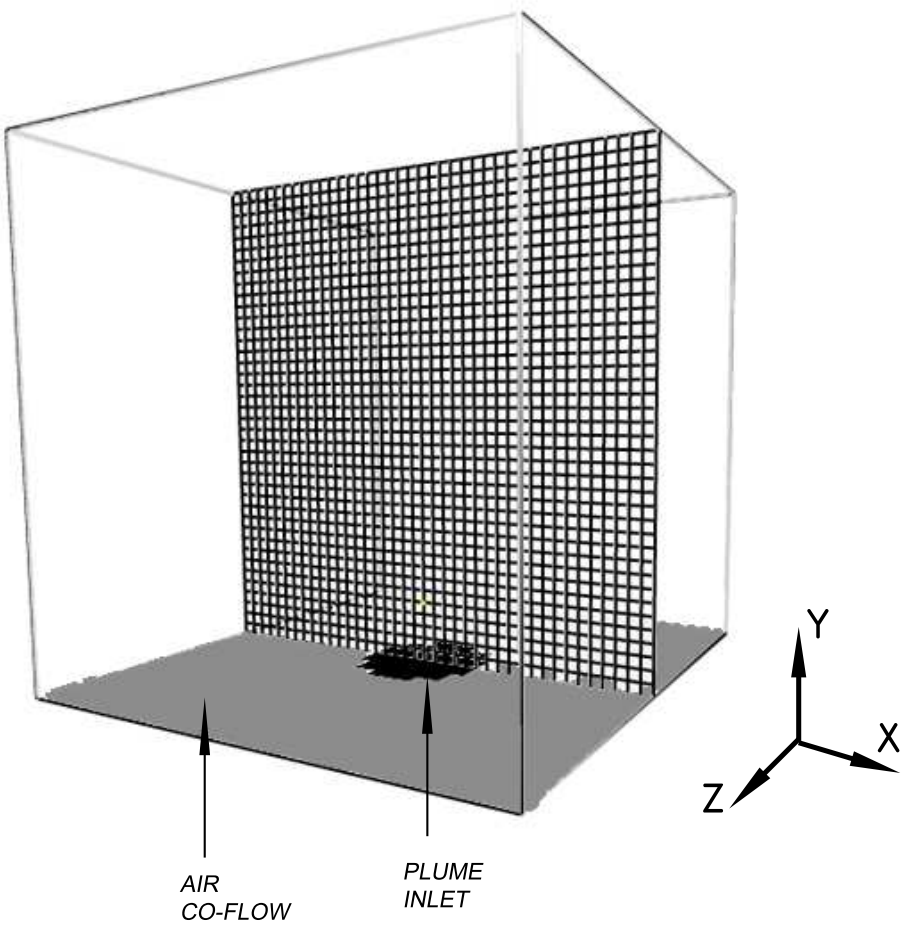

Figure 4.1: Computational domain in LES. White surfaces are openings.

Table 4.1: Plume inlet area and velocity for the various grid sizes

Grid Spacing [m]	Area [m^2]	Velocity [m/s]
0.100	0.800	0.319
0.050	0.790	0.323
0.025	0.790	0.323
Experimental	0.785	0.325

area with the grid resolution used, therefore, the plume inlet velocity is adjusted to ensure that the plume inlet mass flow rate is consistent with that used in the experiment. Values for the plume source area and velocity for the three grid sizes used are in Table 4.1. The adjustment required to match the plume mass flow is also applied to the air inflow rate. To simplify the simulation further, the plume gas, which is composed of helium, acetone and oxygen, is compiled as one gas with a molecular weight of 5.45 g/mol corresponding to the experimental value of the source gas mixture. The remaining surfaces in the computational domain are defined as openings. A uniform mesh is used, i.e. $\Delta_x = \Delta_y = \Delta_z = \Delta$, where Δ_x, Δ_y and Δ_z are the node spacings in the x, y and z direction respectively. Three grid sizes are tested, $\Delta = 0.1$ m, 0.05 m and 0.025 m, resulting in 64x10^3, 512x10^3 and 4096x10^3 cells, respectively.

The LES calculations are set to output data every 0.005 s over 20 s of physical time. The first 10 s allow for the initial flow transients to move downstream and for the flow to reach quasi-steady flow conditions. Data from the second 10 s of simulation is compiled to produce the time averaged quantities.

4.3 Results

With the ability to resolve instantaneous flow fields in LES, numerical results of puffing cycles can be compared with the experimental observations. When the low density helium plume enters the enclosure, it accumulates under a layer of the higher density ambient air. The plume gas gathers until it generates a Rayleigh-Taylor instability. This is caused when

a lighter fluid underlying a heavy fluid is accelerated. The lighter plume gas accelerates upward through the overlying fluid creating a toroidal vortex. The rising accelerating vortex entrains the surrounding air below it creating another heavy layer and the cycle repeats [4, 59, 60].

Instantaneous density contours with velocity vectors can be seen at two different times of the puffing cycle in Figs. 4.2(a) and 4.2(b). These results were produced with the finest mesh, where Δ=0.025 m. In Fig. 4.2(a) plume gas is beginning to accumulate under the heavier layer of ambient air. By the time the simulation has reached the time frame of Fig. 4.2(b), the plume gas has broken through the ambient air. Figure 4.2(b) displays the plume gas rising in a thin stream along the center axis. The velocity vectors show the surrounding air being entrained into the plume.

Figure 4.3 shows time traces of streamwise velocity at a point 0.5 m above the plume source along the center axis. A trace of 4 s time from 12 to 16 s of simulation is displayed. The plume puffing frequency and magnitude for the various grid sizes can be determined with the aid of these time trace plots. Puffing frequency is calculated by dividing the number of puffing cycles by the time span for these cycles. One puff cycle is characterized in Fig. 4.3 by a low streamwise velocity point followed by a high peak and then back to a low point. The coarsest mesh produces a very weak puffing magnitude and the puff frequency cannot be determined. This is due to lack of resolution of the scales of motion required to calculate the fluctuations. In this case, the results are similar to time averaged values. This explains why the velocity is almost constant with little fluctuation in time.

As the mesh is refined the simulated puffing magnitude increases and a better estimate of the puffing frequency can be obtained. As well, the fluctuations within the puff cycles can be seen for the simulation run on the finest mesh. Compared to the puffing frequency of the experiment of 1.36 Hz [4], the meshes of $512\text{x}10^3$ and $4096\text{x}10^3$ cells produce puffing frequencies of 1.2 Hz and 1.3 Hz respectively. Refinement of the mesh acts to generate a more accurate accounting of the interacting scales in the flow resulting in better estimates of puffing frequency and more realistic puffing magnitude.

The radial profiles of the time average and rms cross-stream velocity, streamwise velocity and plume concentration results are displayed in Figs. 4.4, 4.5, 4.6 and 4.7 respectively

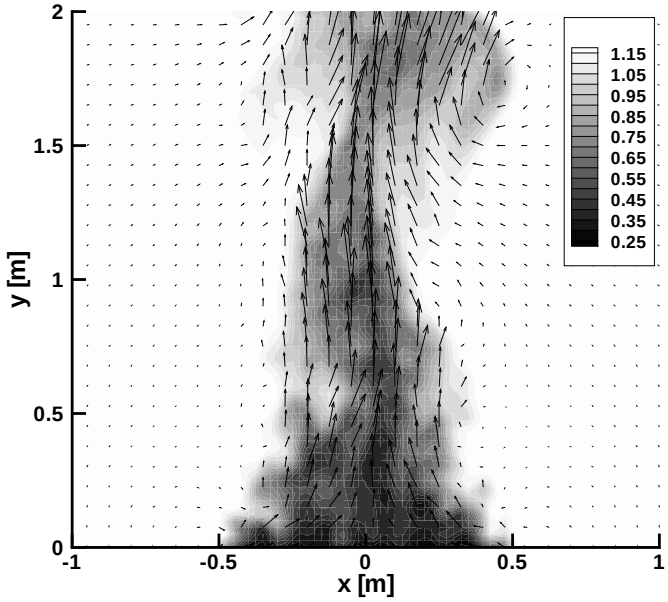

(a)

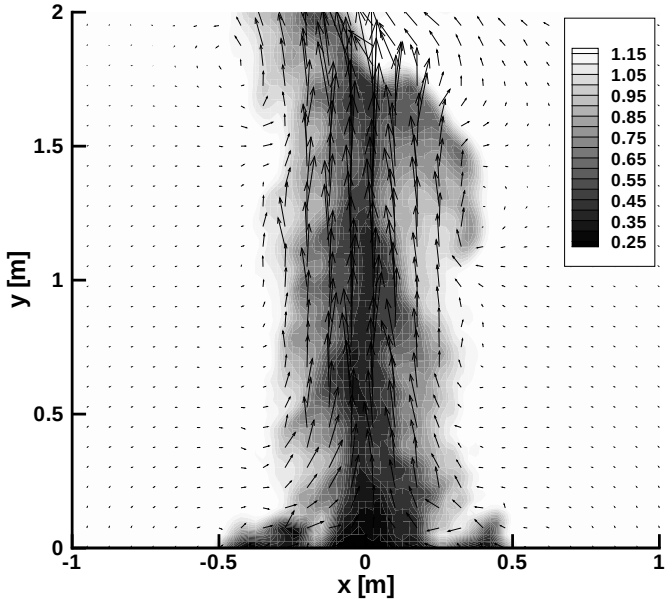

(b)

Figure 4.2: Density contours overlayed with velocity vectors at two instances during the puff cycle (LES, $4096{\cdot}10^3$ cells). (a) t = 14.51[s] (b) t = 14.84[s].

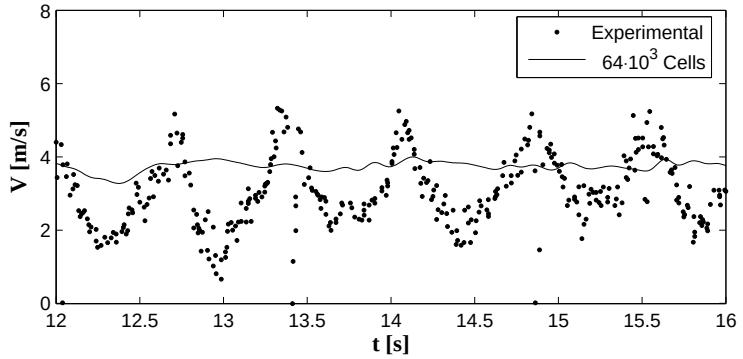

(a)

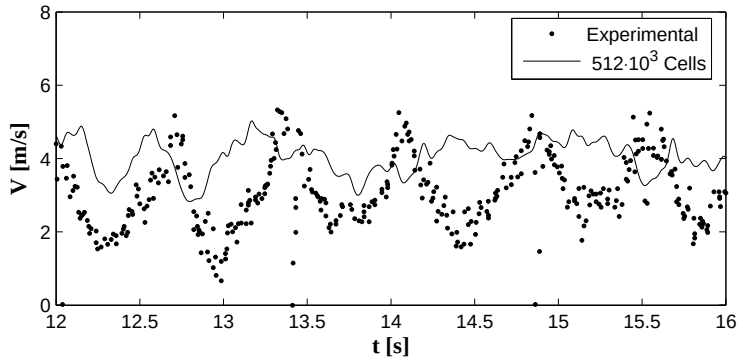

(b)

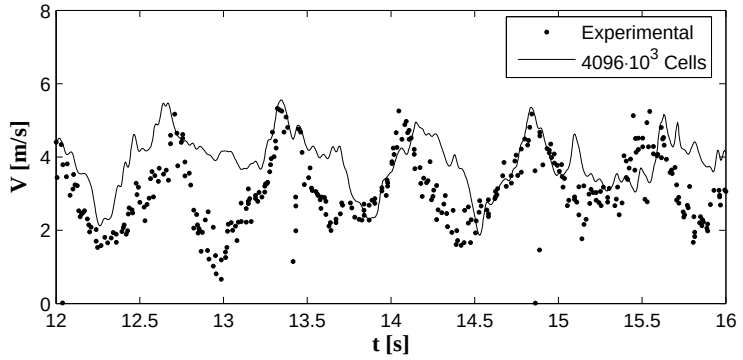

(c)

Figure 4.3: Time trace of streamwise velocity at y=0.5 m above the plume source on the center axis for the various grid resolutions. (a) $64{\cdot}10^3$ cells (b) $512{\cdot}10^3$ cells (c) $4096{\cdot}10^3$ cells.

at three vertical distances from the plume source, y=0.2 m, y=0.4 m and y=0.6 m. The gray shaded region in each figure represents the experimental uncertainty. Plotted are the results of the LES plume simulations run on each of the three grid sizes against the experimental data at varying distances from the plume inlet. Values of time averaged velocity and plume concentration appear to have become independent of the chosen mesh size for the finest meshes simulated and at all locations tested.

The cross-stream velocity results capture the shape of the radial profile of the plume near the plume inlet. Within the plume, cross-stream velocity magnitudes are over predicted. RMS quantities are generally lower than the experimental data. The grid sizing does not have a large impact on the time averaged cross-stream velocity but differences in value due to grid size are evident in the rms quantities. The variance of grid size acts to increase the level of fluctuation. Large grid spacing leads to a larger length scale which is modeled as opposed to fully resolved. These modeled length scales cannot produce the small fluctuations within the velocity field, they essentially determine an averaged velocity field. By decreasing the grid spacing, the smaller fluctuations can be determined, thus the rms quantities increase.

Streamwise velocity results are presented in Fig. 4.5. The time-averaged peak centerline axial velocity values over predicted in all cases. This is consistent with the over predicted cross-stream values ensuring that the conservation of mass is maintained. A larger amount of the surrounding air is entrained in the numerical models compared to the experimental data, thus the streamwise velocity also over predicts the experimental values. The error in the estimation increases as the distances from the plume source increases. For the finest mesh, the simulation over predicts the peak time averaged streamwise velocity by 19%, 24% and 40% for distances of 0.2 m, 0.4 m and 0.6 m from the plume source, respectively. At radial locations greater than approximately 0.1 m streamwise velocity predictions are quite good. This is true for all grid sizes tested. The streamwise velocity rms values under predict experimental data along the center axis. Rms quantities at radial distances greater than 0.1 m are in good agreement with the experimental values.

The buoyancy-induced turbulence from the small scales of motion is not resolved adequately in the present implementation of LES. This explains why the predictions near the

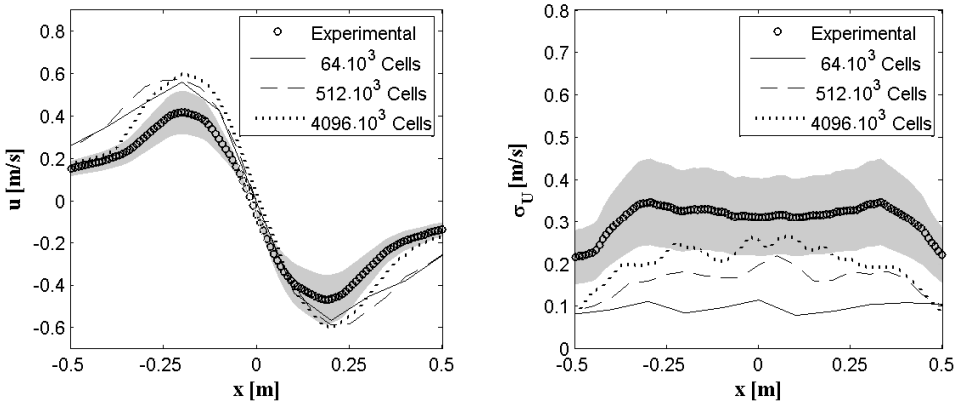

(a) y = 0.2 m

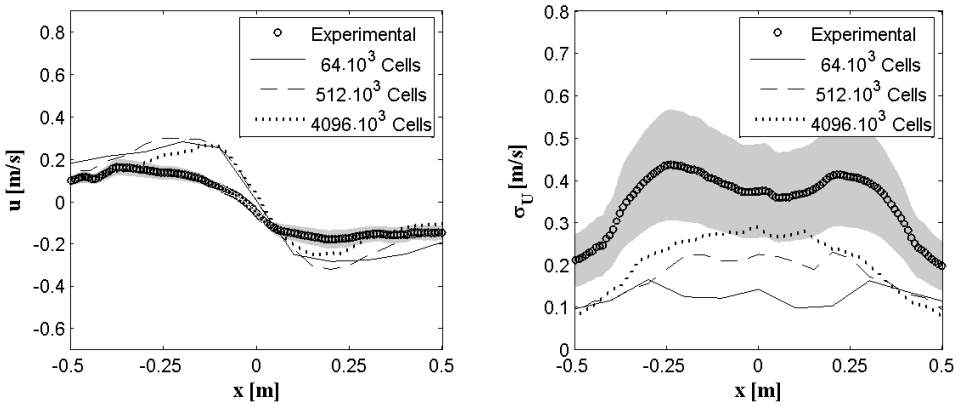

(b) y = 0.4 m

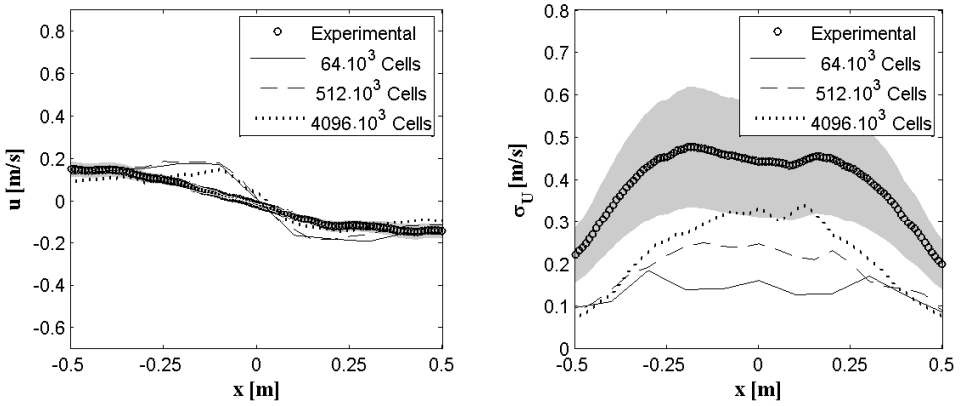

(c) y = 0.6 m

Figure 4.4: Time averaged cross-stream velocity (left) and cross-stream rms velocity (right) comparison of varying grid sizes to experimental data.

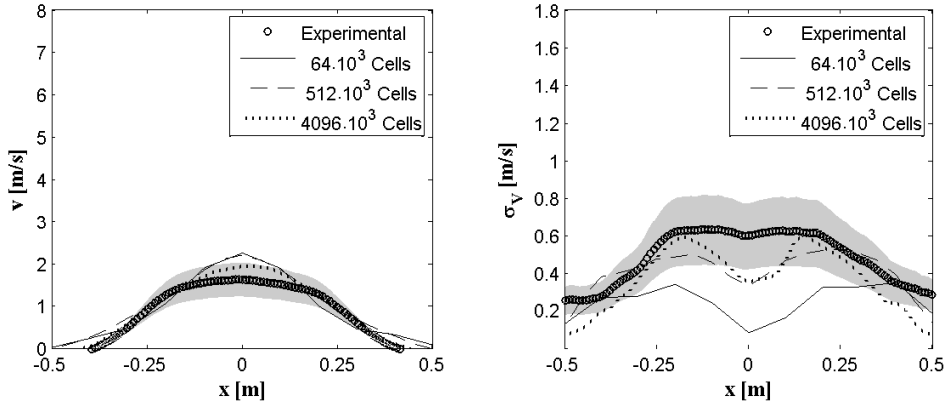

(a) y = 0.2 m

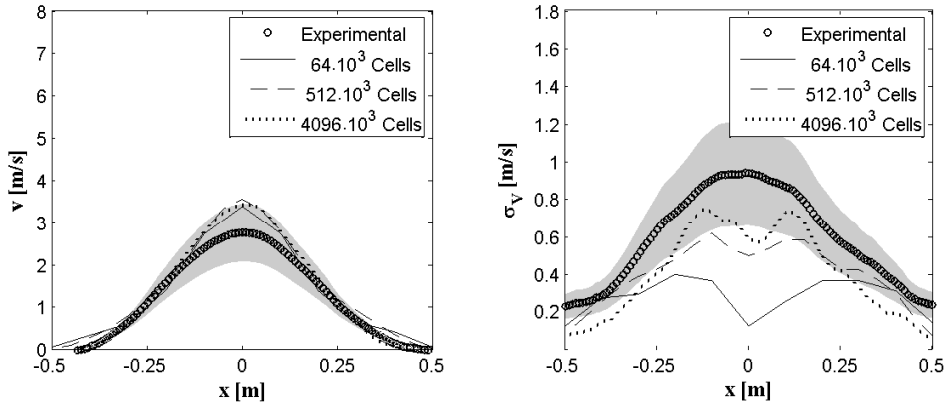

(b) y = 0.4 m

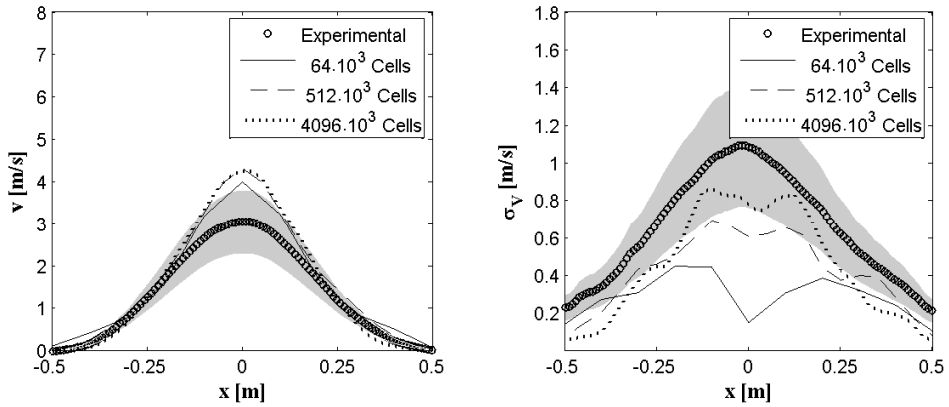

(c) y = 0.6 m

Figure 4.5: Time averaged streamwise velocity (left) and streamwise rms velocity (right) comparison of varying grid sizes to experimental data.

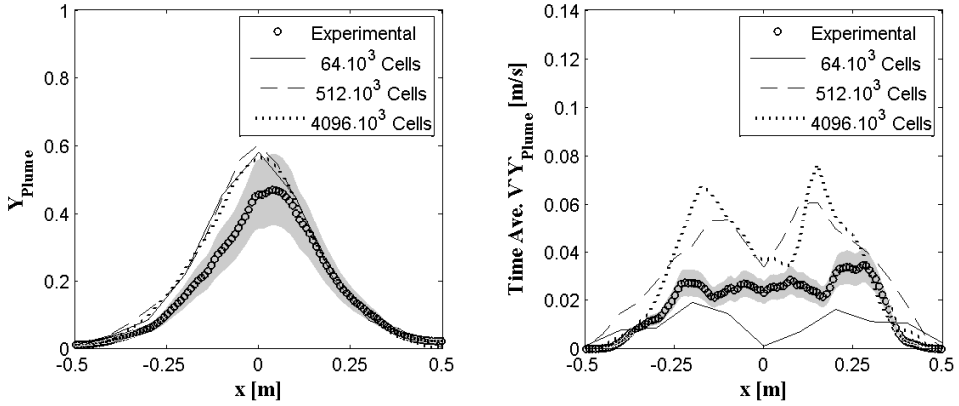

(a) y = 0.2 m

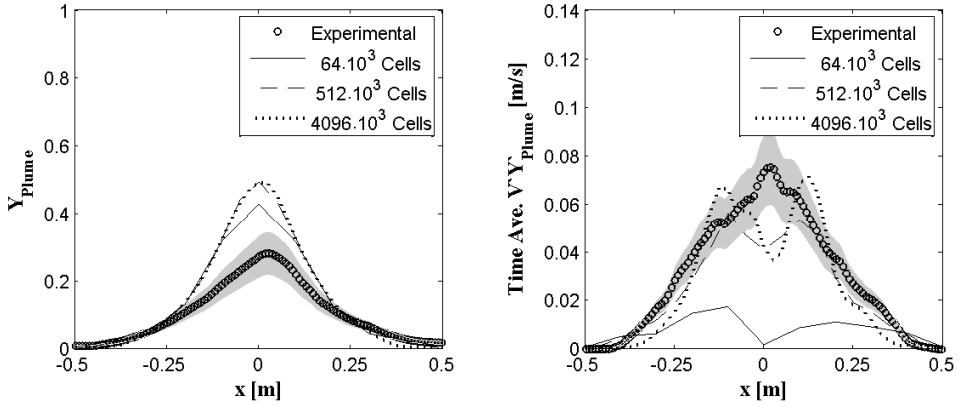

(b) y = 0.4 m

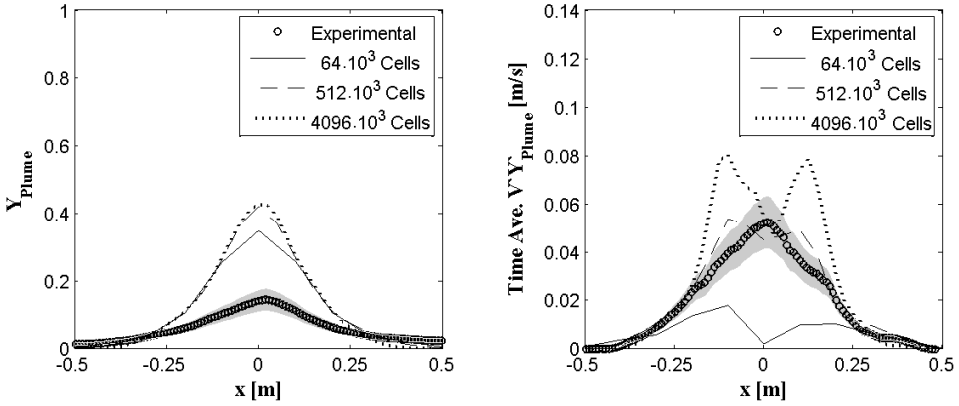

(c) y = 0.6 m

Figure 4.6: Time averaged plume concentration (left) and V'Y'$_{plume}$ (right) comparison of varying grid sizes to experimental data.

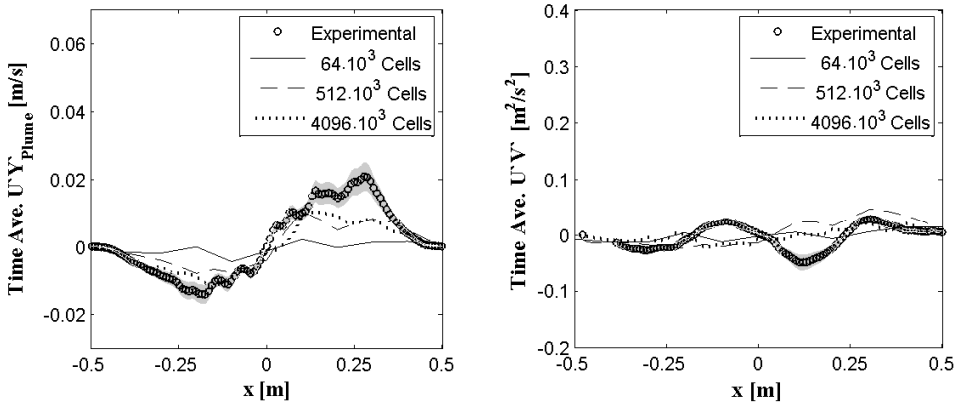

(a) y = 0.2 m

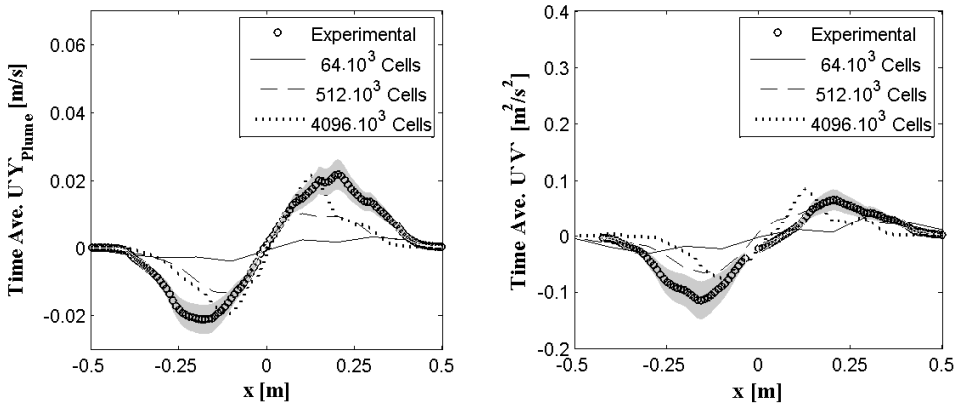

(b) y = 0.4 m

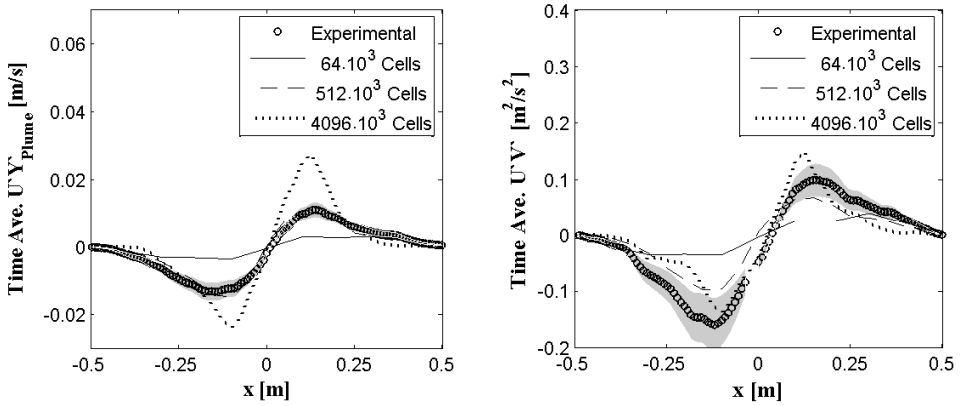

(c) y = 0.6 m

Figure 4.7: Time averaged U'Y'$_{plume}$ (left) and U'V' (right) comparison of varying grid sizes to experimental data.

base of the plume are good, where the larger scale fluctuations are predominate. Moving away from the plume source, the flow should get more and more turbulent due to buoyancy and shear production but the rate at which it does is lower than the experimental plume. Thus, mixing rates, buoyancy and shear production are under predicted and the plume rises without much lateral dissipation.

Similar to the case of time averaged streamwise velocity, values of time averaged plume concentration are over predicting the experimental data in the center axis region. The percent difference from the experimental data in the numerical model increases with the distance from the plume source. At distances of 0.2 m, 0.4 m and 0.6 m from the plume source, resultant discrepancies of 24%, 82% and 202% occur in the plume concentration, respectively. Good predictions for time averaged plume concentration are obtained at radial distances greater than 0.25 m. The under resolved buoyancy-induced turbulence is one likely cause for the over prediction of concentration values on the center axis since mixing rates of ambient fluid into the plume would be suppressed. Figure 4.8 shows the plume concentration contours built from the experimental data and the finest mesh data simulations run on. The first three contours of the numerical results at the plume source indicate that the numerical results are under predicting the experimental data along the center axis. As the distance from the plume source increases, the numerical results begin to over predict the experimental results. In this region it can be seen that rather than spreading laterally dut to entrainment and mixing, the plume simply carries upward.

Experimental rms values of the plume concentration were not available. Rather, experimental data of a cross correlation between velocity and plume concentration fluctuations is provided to provide further insight into the dynamics of the plume concentration. The time averaged $V'Y'_{Plume}$ radial profiles displayed in Fig.4.6 shows a valley at the center axis. The peaks on either side of the center axis correspond to the shear layer between the plume and surrounding air causing the fluctuations in the streamwise velocity and plume concentration. The peaks are a result of flickering in the diffusion of the plume gas into the ambient gas. Further, there is a greater buoyancy acceleration in this region then along the center axis causing the larger amounts of fluctuation. The center of the plume is relatively consistent and therefore does not produce the flickering leading to the large amounts of fluctuation. This is consistent with the experimental results of Albers and Agrawal [61]

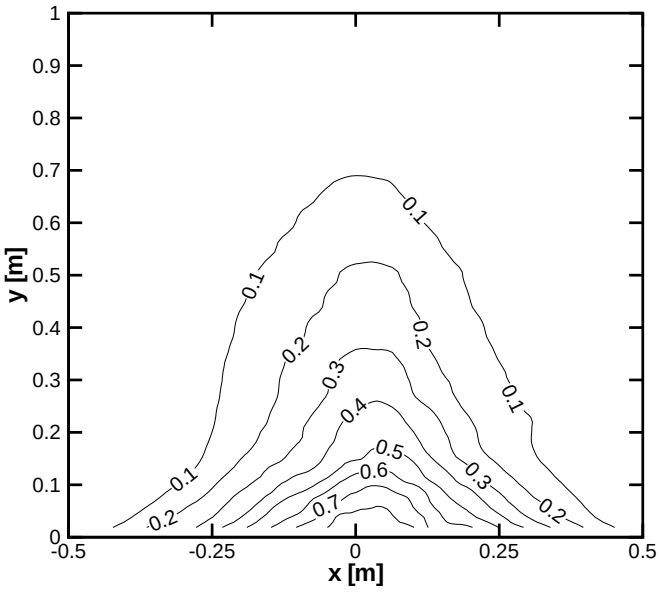

(a)

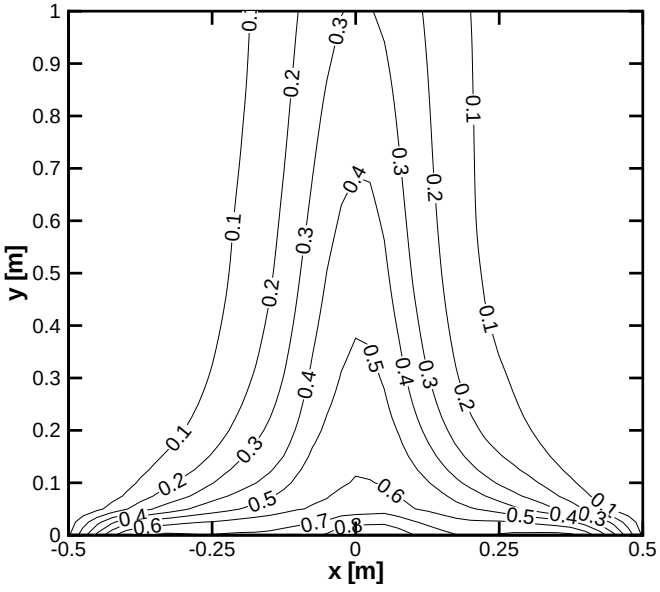

(b)

Figure 4.8: Plume concentration contours. (a) experimental (b) $4096{\cdot}10^3$ cells.

and the numerical results of Zhou et al. [40] and DesJardin et al. [6]. This is not evident in the experimental work because the plume concentration and velocity gradients are more gradual in the radial direction. The numerical results contain large gradients leading to the strong buoyancy forces in the region separating the two gases.

The cross correlation for the cross-stream velocity and plume concentration fluctuations are found in the time averaged $U'Y'_{Plume}$ and $U'V''$ displayed in Figs.4.7. The time averaged $U'Y'_{Plume}$ as well as the time averaged $U'V'$ predict similar trends to the experimental data. As the mesh is refined the peak values increase. In the case of the time averaged $U'Y'_{Plume}$, the maximum and minimum predictions for the finest mesh over predict the experimental data and the error increases as the distance from the plume source increases. Numerical results for the time averaged $U'V'$ values lie just outside of experimental uncertainty.

In validating FDS with test runs, Zhang et al. [62] varied the empirical constants C_s, Pr and Sc and found the results to be most sensitive to the Smagorinsky constant, C_s. Therefore, in this work, simulations were run for Smagorinsky constants of 0.0 and 0.1 and compared to the experimental data as well as results of the simulation using the default value of C_s=0.2. Radial profiles of cross-stream velocity, streamwise velocity and plume concentration results for the varying values of Smagorinsky constant are displayed in Figs. 4.9, 4.10, 4.11 and 4.12 respectively for C_s=0.0, 0.1 and 0.2.

Experience of FDS users have found that best results are obtained when the Smagorinsky constant is set to a value as low as possible while still maintaining numerical stability [14]. This means that the resolvable eddies are not "damped" by excessive amounts of artificial viscosity. The current results are consistent with this assessment. Larger discrepancies between model and experimental time averaged streamwise velocity and plume concentration data is seen for increasing values of C_s. When $C_s = 0.3$ the time averaged values along the center axis overshoot the results with the default value.

The cross-stream radial profile results with varying Smagorinsky constant in Fig. 4.9 show that lowering the Smagorinsky constant has little effect on the time averaged cross-stream velocity. The cross-stream rms quantity decreases as the Smagorinsky constant is lowered. The time averaged streamwise velocity and plume concentration radial profiles displayed in Figs. 4.10 and 4.11 show that decreasing the Smagorinsky constant produces

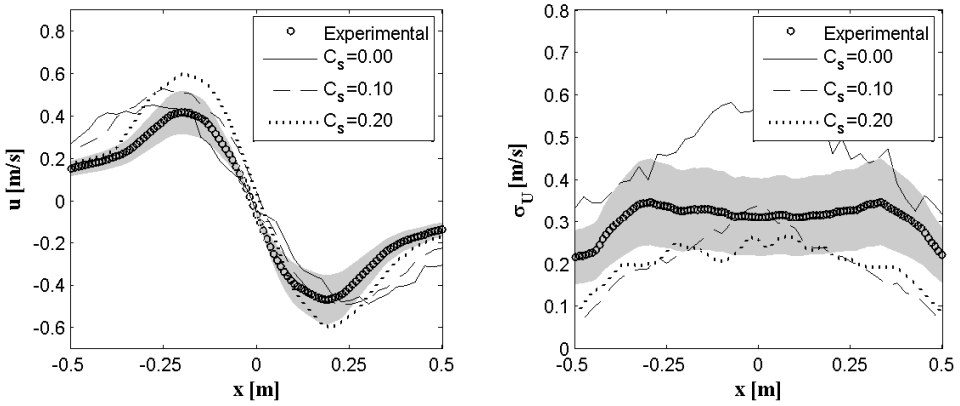

(a) y = 0.2 m

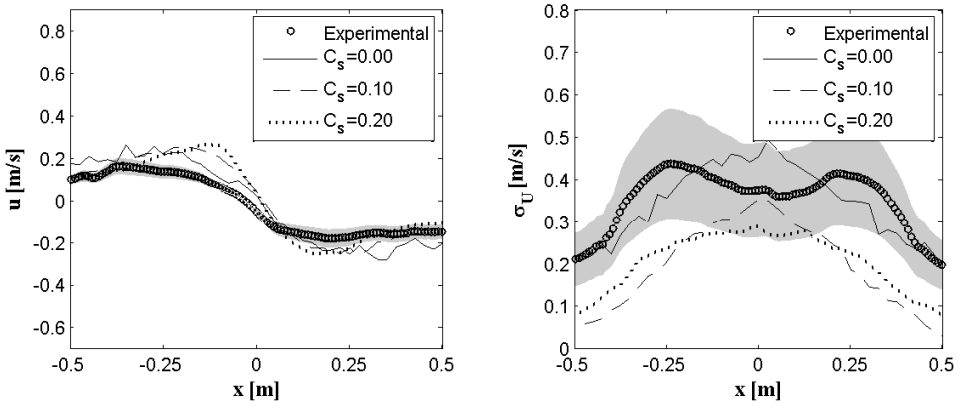

(b) y = 0.4 m

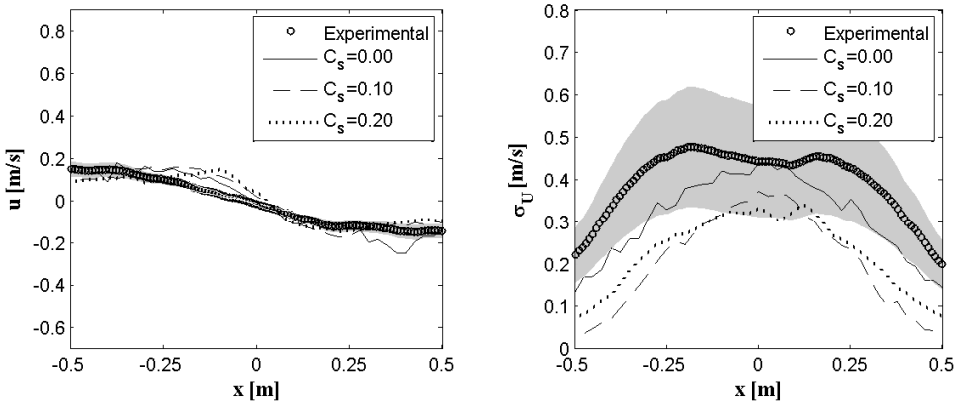

(c) y = 0.6 m

Figure 4.9: Time averaged cross-stream velocity (left) and cross-stream rms velocity (right) comparison of varying Smagorinsky constants.

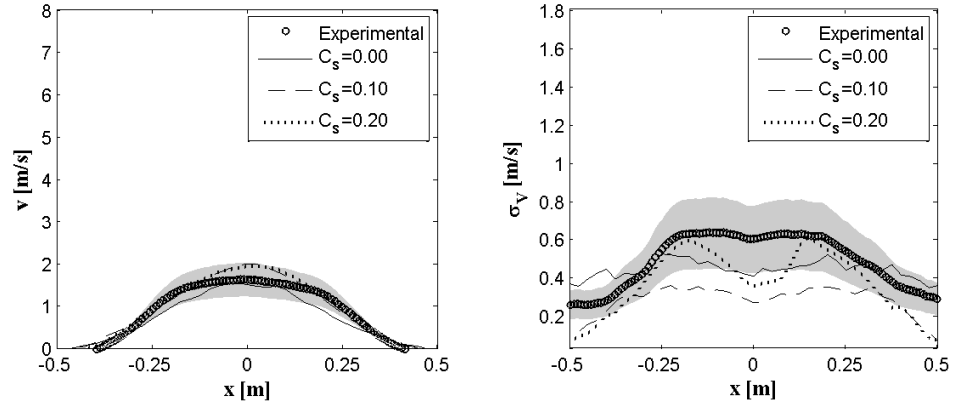

(a) y = 0.2 m

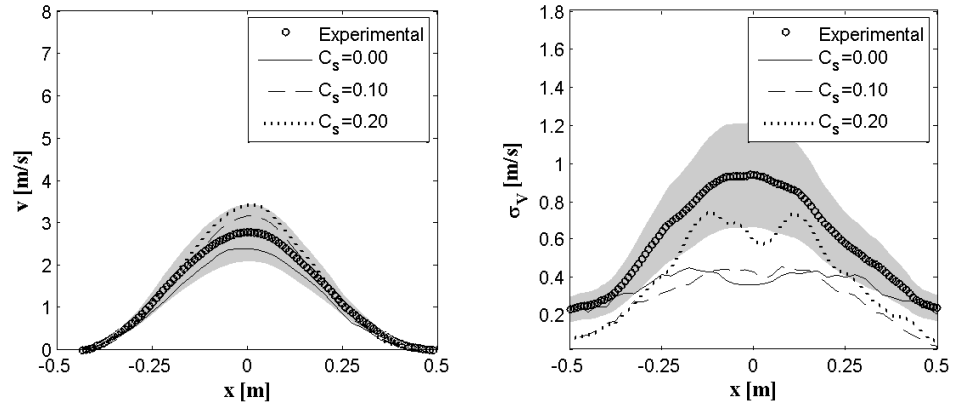

(b) y = 0.4 m

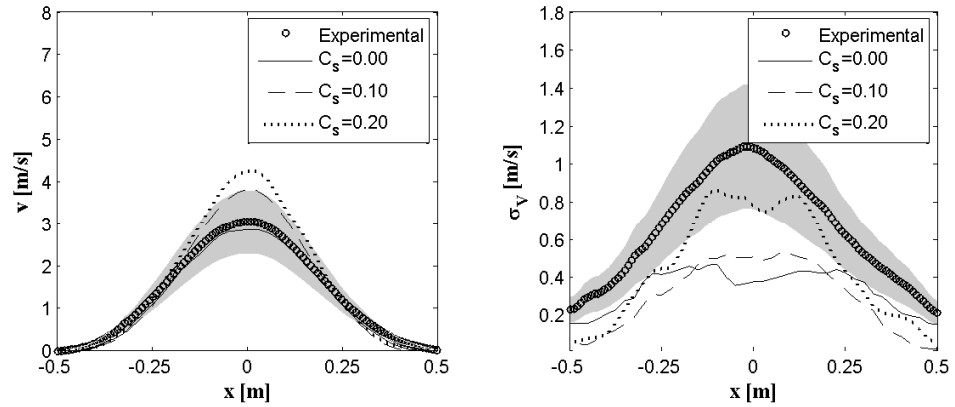

(c) y = 0.6 m

Figure 4.10: Time averaged streamwise velocity (left) and streamwise rms velocity (right) comparison of varying Smagorinsky constants.

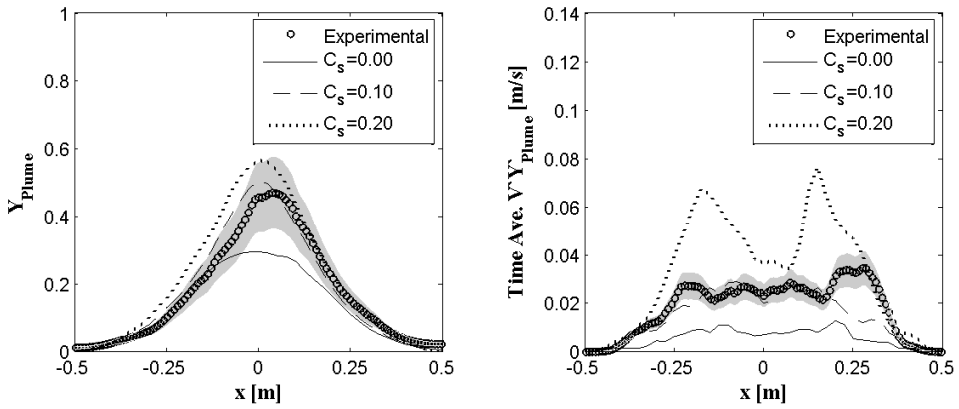

(a) y = 0.2 m

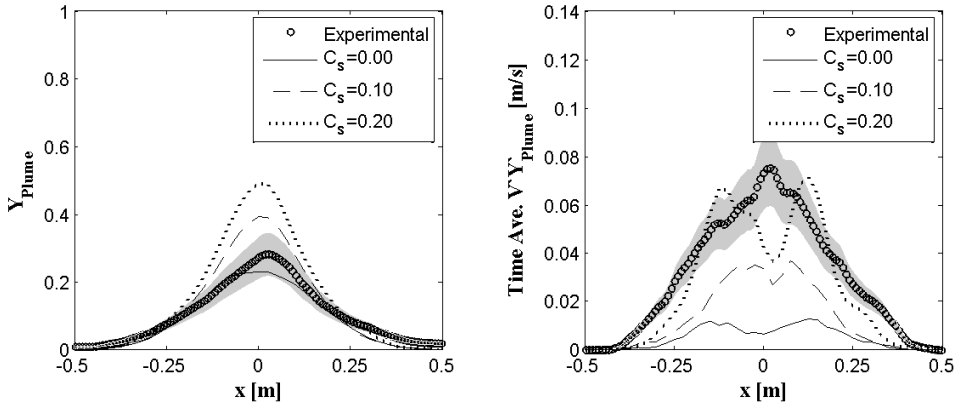

(b) y = 0.4 m

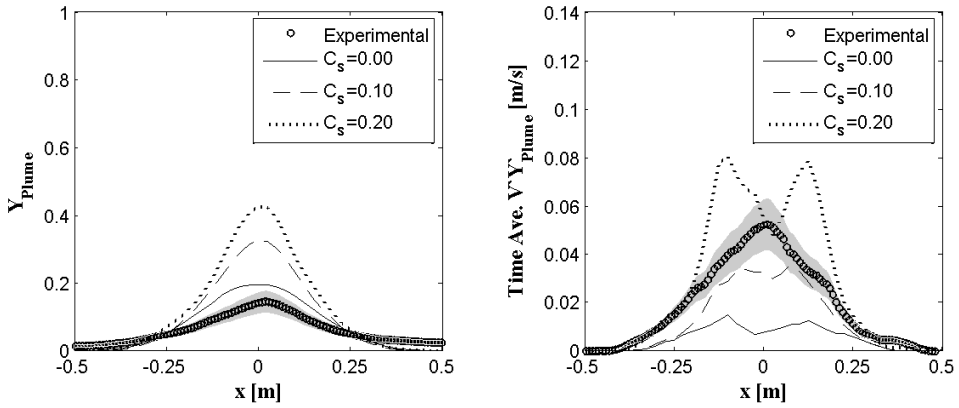

(c) y = 0.6 m

Figure 4.11: Time averaged plume concentration (left) and V'Y'$_{plume}$ (right) comparison of varying Smagorinsky constants.

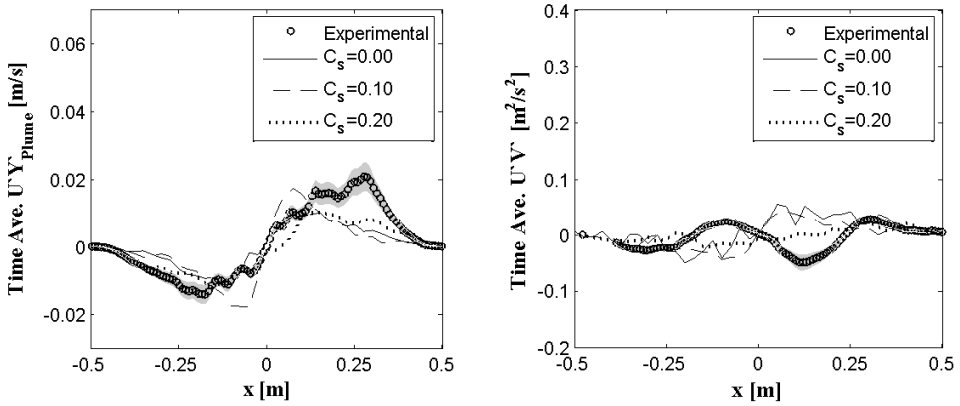

(a) y = 0.2 m

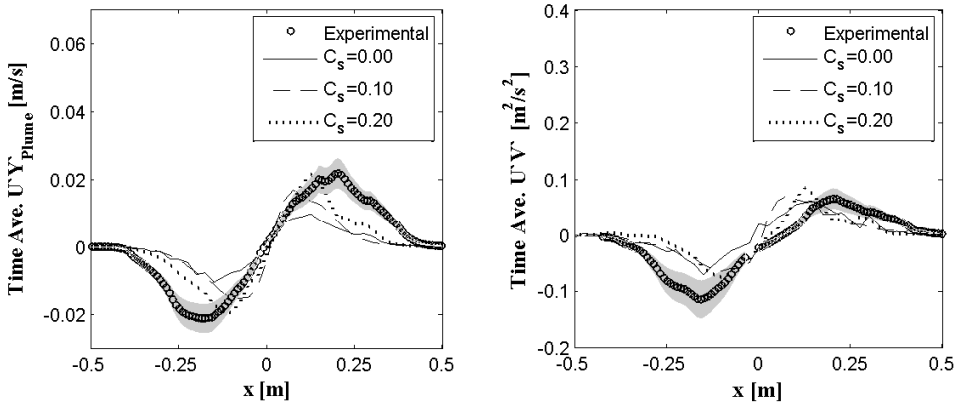

(b) y = 0.4 m

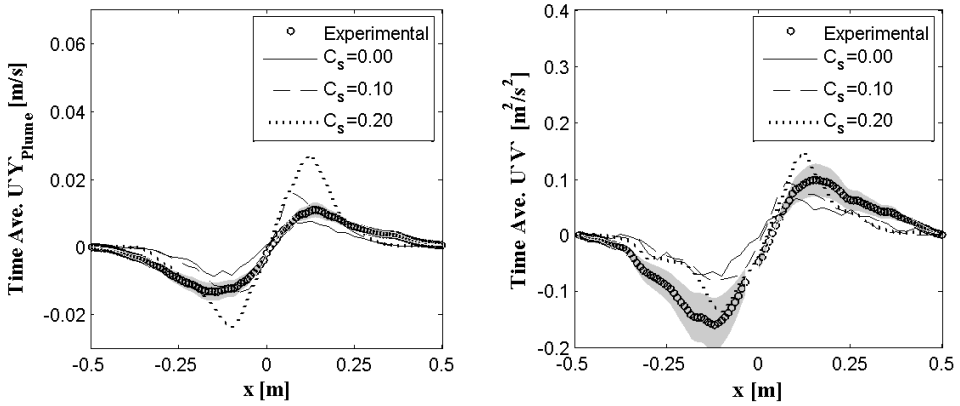

(c) y = 0.6 m

Figure 4.12: Time averaged U'Y'$_{plume}$ (left) and U'V' (right) comparison of varying Smagorinsky constants.

more accurate time averaged streamwise velocity and plume concentration results. When the Smagorinsky constant is set to zero, very good results are produced for the time averaged streamwise velocity and within experimental uncertainty. But similar to the model using the RANS approach which produced good velocity results but poor helium concentration measurements, the time averaged helium concentration spreading rates are not correctly predicted. While the time averaged values are more accurately predicted when the Smagorinsky constant is decreased, a greater error is produced in the rms values.

The time averaged streamwise velocity contours based on the experimental results are compared with the numerical results with a Smagorinsky constant of 0.0 in Fig. 4.13. The radial spread of the contours is well predicted and comparable to that seen from the experimental data. The contours of the numerical results indicate the same problem which occurred when the Smagorinsky constant was at the default value of 0.2. As the distance from the plume source increases, the velocity contours along the centerline continue to increase. This indicates that the plume gas continues to accelerate as the distance from the plume source increases although at a lower rate than the results of the model run with the default value of Smagorinsky constant.

The results of the centerline streamwise velocity profiles are displayed in Fig. 4.14. The numerical results agree well with experimental values near the plume source. Error in the numerical model increases as the distance from the plume source increases. The experimental data indicates that the streamwise velocity begins to decrease 0.69 m above the plume source. The streamwise velocity along the centerline for the numerical model on the other hand levels off at 1.25 m above the plume source at a velocity of 5.04 m/s when $C_s = 0.2$ and 3.5 m above the plume source at a velocity of 4.29 m/s when $C_s = 0.0$. Nicolette et al. [63] noted that the transition from laminar to turbulence affects the time averaged centerline streamwise velocity by lowering the peak velocity relative to what would be produced by a pure laminar flow. Turbulence acts to spread the momentum of the plume and thus the peak value decreases. Figure 4.14 indicates that the numerical model is not accurately simulating this transition. This leads to the inability to resolve the buoyancy-induced turbulence which produces the poor results along the centerline.

The time averaged plume concentration contours obtained from the experimental results

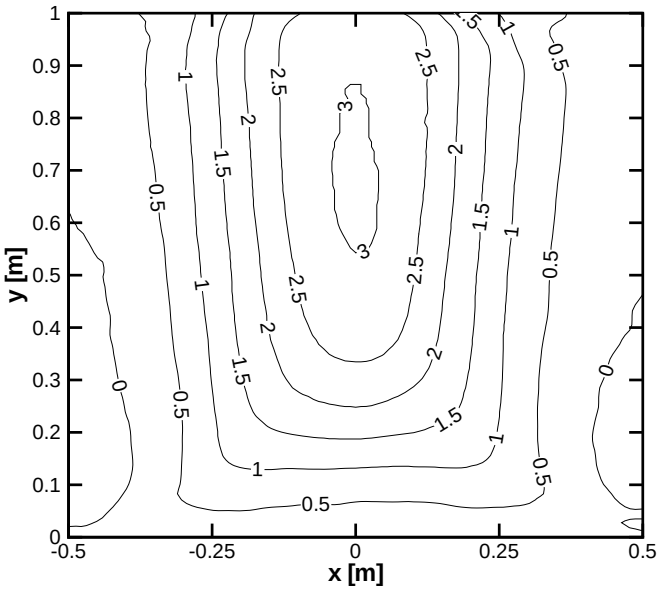

(a)

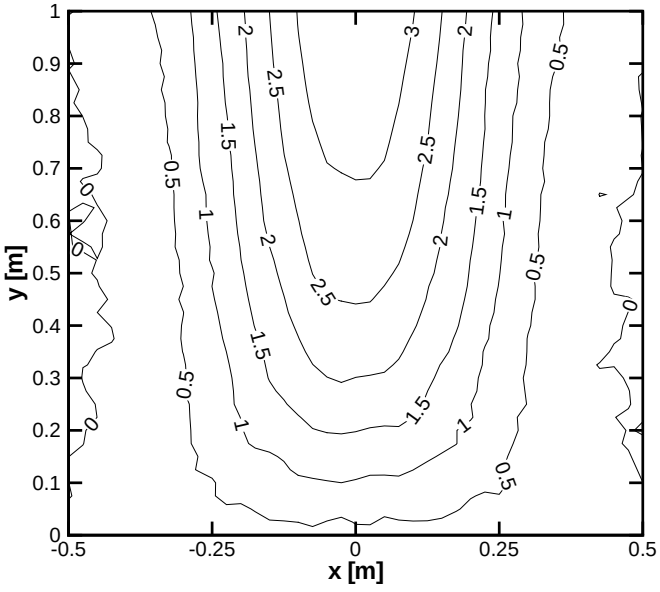

(b)

Figure 4.13: Streamwise velocity contours. (a) experimental (b) $C_s = 0.00$.

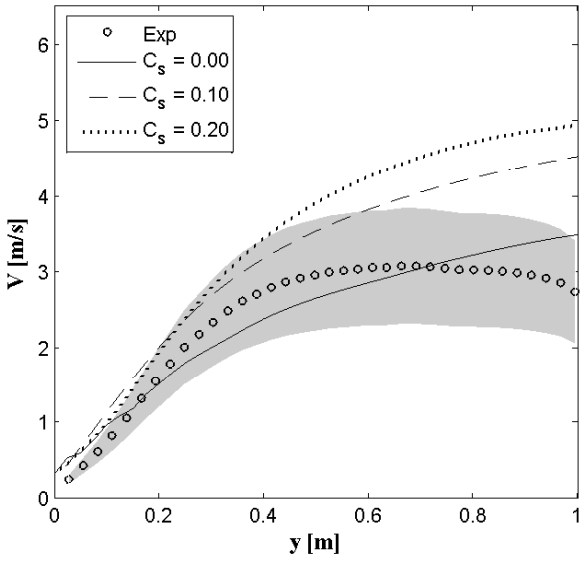

Figure 4.14: Centerline streamwise velocity comparison.

and numerical results with a Smagorinsky constant of 0.0 are displayed in Fig. 4.15. Near the plume source the numerical results once again under predict the experimental results as was the case when the Smagorinsky constant was 0.2. With the Smagorinsky constant at 0.0 the under prediction is even greater near the plume source and the vertical gradient of plume concentration decreases.

The large helium plume of O'Hern et al. [4] was previously numerically modeled using LES by DesJardin et al. [6]. Molecular and turbulent flux and stress terms for the filtered conservation equations were approximated using standard fourth-order centered finite differencing and integrated in time using a finite volume formulation with standard fourth-order Runge-Kutta time advancement. Low Mach number characteristics were incorporated into the momentum and energy transport equations to reduce computational cost by implementing the PGS methods of O'Rourke et al. [64, 65].

The present results are consistent with those obtained by DesJardin et al. [6] for the time averaged properties. Best results for their simulations were produced for the finest

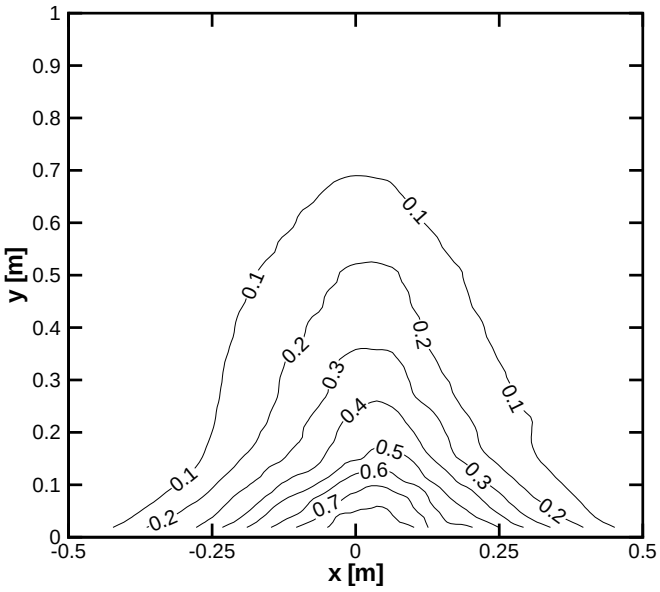

(a)

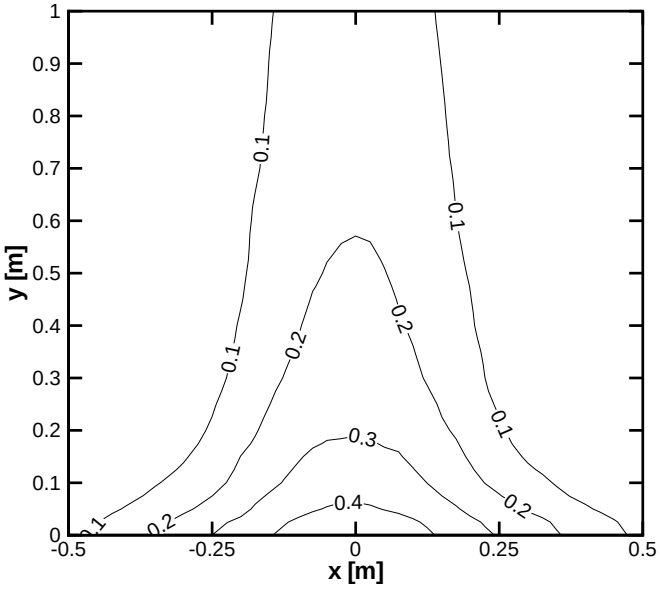

(b)

Figure 4.15: Plume concentration contours. (a) experimental (b) $C_s = 0.00$.

mesh and no SGS model ($C_s = 0$). Time averaged streamwise velocity results were within experimental uncertainty while the time averaged plume concentration was highly over predicted along the center axis. The results were found to be very sensitive to the grid resolution for the two grid sizes tested.

Contrary to the present results, rms quantities produced by DesJardin et al. [6] did not exhibit peaks away from the center axis. Streamwise and plume concentration rms results of DesJardin et al. [6] were larger than the experimental values and the error increased as the distance from the plume source increased. Similar to the present results, rms quantities were better predicted with the addition of the SGS model.

4.4 Conclusions

Large eddy simulation calculations of the axisymmetric helium plume proved to be sensitive to mesh spacing and the Smagorinsky constant, C_s. With a coarse mesh, the smaller scales of motion were not resolved and simply modeling them produced results similar to using a RANS approach. There was very little fluctuation in the puffing cycle. As the mesh was refined, the puffing magnitudes increased and values of puffing frequency matched well with the experimental data.

Time averaged values for the two velocity components and the plume concentration showed little sensitivity to the mesh spacing. The cross-stream velocity was well captured. Streamwise velocity and plume concentration significantly over predicted center axis values at the three distances from the plume source tested. Similar to the puffing cycles, rms quantities showed sensitivity to the mesh spacing. The finest mesh tested proved to produce the best results.

When the Smagorinsky constant was set to zero, essentially turning off the modeling portion of the smaller eddies, very good time averaged velocity predictions were obtained. Predicted results lay within the experimental uncertainty of the data. Compared to the default model, plume concentrations were better predicted but this improvement is not consistent at all distances from the plume source tested.

The time averaged centerline streamwise velocity indicated that the laminar to turbulence transition was not accurately captured. The numerical model predicted this transition further from the plume source than what was expected according to the experimental data. This caused the plume to continue to accelerate leading to an over prediction in peak time averaged streamwise velocity values.

Chapter 5

Conclusions

CFD analysis of buoyant plumes is an important tool for fire safety research. In studying the dynamics of the plume, fire safety engineers can develop preventative measures as well as assessment of risk. It is important that full and accurate models be developed for this purpose. The present work extends the existing body of work of numerical simulations of buoyant plumes into the near source region.

5.1 Assessment of Current Results

Two helium plumes were tested in the RANS study: the planar wall plume of Sangras et al. [2, 3] and the axisymmetric plume of O'Hern et al. [4]. The addition of the buoyancy source terms via the SGDH and GGDH model to the standard k-ε model presented different results in terms of the dependency of the model on the buoyancy constant, $C_{3\varepsilon}$. The results of the planar plume in the self-preserving region proved to be consistent with those gathered by Van Maele et al. [26]. The SGDH buoyancy model showed no dependency on the buoyancy constant while the GGDH buoyancy model indicated a small dependency on the buoyancy constant. Both models produced good velocity and mass fraction results when compared to the experimental data.

For the axisymmetric plume in the near-source region, the addition of buoyancy source terms via the CFX, SGDH and GGDH buoyancy models presented a significant improvement over use of the standard k-ϵ model prediction of both the streamwise velocity and plume concentration profiles. Overall, the CFX and SGDH buoyancy models demonstrated the best performance in terms of predicting plume concentration while the GGDH model produced the best results for the streamwise velocity. It is expected that the buoyancy constant may have to be tuned depending on the conditions of the buoyant plume to be modeled because of the high sensitivity of the results to values for the buoyancy constant.

The RANS results of the axisymmetric plume and the dependency of the results on the buoyancy constant are contrary to the results of studies summarized in Chapter 2 which are plumes studied in the self-preserving region. The axisymmetric plume of O'Hern et al. [4] shows that in the near source region of buoyant plumes, the buoyancy modified standard k-ε model reacts differently to the buoyancy constant than in the self-preserving region.

The LES study of the axisymmetric plume in the near source region indicated that the model results were sensitive to both the mesh spacing and the Smagorinsky constant, C_s. With the default Smagorinsky constant set in the FDS model the time averaged velocity and plume concentration showed little sensitivity to the grid spacing with the finest mesh used, which was a uniform spacing of 0.025 m between nodes. Both the time averaged streamwise velocity and plume concentration over predicted the experimental results along the center axis well outside of experimental uncertainties. The rms quantities showed significant sensitivity to the mesh spacing chosen and the results generally improved relative to experimental data with the refinement of the mesh. Decreasing the Smagorinsky constant produced an improvement on the time averaged velocity and plume concentration results but the accuracy in the results vary with the vertical distance from the plume source. The time-averaged centerline streamwise velocity profile indicated the laminar-to-turbulence transition was poorly predicted and that the transition occurred later in the flow than what was expected.

5.2 Future Work

The basic Smagorinsky model and the constant C_s in the LES approach did not produce adequate results for both time averaged and rms values of the plume velocity components and plume concentration. While a higher Smagorinsky constant produced better predictions of experimental rms results, a lower value for the constant produced better predictions of the measured time averaged quantities. Further, the level of accuracy varied with the distance from the plume source as well as in the radial direction.

It is suggested that a subgrid model with the inclusion of buoyancy effects such as the one proposed by Brown et al. [66] be implemented. This type of model introduces a 'backscatter' which transfers energy against the flow of the turbulent energy cascade from small to large scales. The study undertaken by Brown et al. [66] concluded that implementing this model created more turbulence. The present model indicates that the plume gas continues to accelerate as the distance from the plume source increases where as the experimental data shows that the plume gas begins to slow down at a distance of 0.69 m above the plume inlet. It is expected that for the axisymmetric plume studied in the near source region that creating more turbulence would act to produce better and more consistent prediction in the time averaged streamwise velocity and plume concentration than the present model.

Bibliography

[1] W. Rodi. *Turbulent buoyant jets and plumes*. Permagon Press, 1982.

[2] R. Sangras, Z. Dai, and G.M. Faeth. Mixture fraction statistics of plane self-preserving buoyant turbulent adiabatic wall plumes. *J. Heat Transfer*, 121:837–43, 1999.

[3] R. Sangras, Z. Dai, and G.M. Faeth. Velocity statistics of plane self-preserving buoyant turbulent adiabatic wall plumes. *J. Heat Transfer*, 122:693–700, 2002.

[4] T.J. O'Hern, E.J. Weckman, A.L. Gerhart, S.R. Tieszen, and R.W. Schefer. Experimental study of a turbulent buoyant helium plume. *J. Fluid Mech.*, 544:143–71, 2005.

[5] E. Marotta. Fire losses in canada: Annual report 2002. Technical report, Council of Canadian Fire Marshals and Fire Commissioners, 2002.

[6] P.E. DesJardin, T.J. O'Hern, and S.R. Tieszen. Large eddy simulation and experimental measurements of the near-field of a large turbulent helium plume. *Phys. Fluids*, 16:1866–1883, 2004.

[7] L.F. Richardson. *Weather prediction by numerical process*. Cambridge University Press, Cambridge, 1922.

[8] A.N. Kolmogorov. The local structure of turbulence in incompressible viscous fluid for very large reynolds numbers. *Dokl. Akad. Nauk SSSR*, 30:299–303, 1941.

[9] S.B. Pope. *Turbulent Flows*, chapter 10. Cambridge University Press, 2000.

[10] J. Smagorinsky. General circulation experiments with the primitive equations. i. the basic experiment. *Monthly Weather Review*, 91:99–164, 1963.

[11] J.W. Deardorff. Numerical investigation of neutral and unstable planetary boundary layers. *J. Atmos. Sci.*, 29:91–115, 1972.

[12] M. Germano, U. Piomelli, P. Moin, and W.H. Cabot. A dynamic subgrid-scale eddy viscosity model. *Phys. Fluids*, 3(7):1760–1765, 1991.

[13] D.K. Lilly. A proposed modification of the germano subgrid-scale closure method. *Phys. Fluids A*, 4(3):633–635, 1992.

[14] K. McGrattan and G. Forney. *Fire dynamics simulator (Version 4) technical reference guide*, 2006.

[15] B.S. Baldwin and H. Lomax. Thin layer approximation and algebraic model for separated turbulent flow. *AIAA*, pages 78–257, 1978.

[16] T. Cebeci and A.M.O Smith. *Analysis of turbulent boundary layers: Applied mathematics and mechanics, Vol 15*. Academic Press, New York, 1974.

[17] B.S. Baldwin and T.J. Barth. A one-equation turbulence transport model for high reynolds number wall-bounded flows. *AIAA*, page TM 102847, 1990.

[18] P.R. Spalart and S.R. Allmaras. A one-equation turbulence model for aerodynamic flows. *Récherche Aerospatiale*, 1:5–21, 1994.

[19] A.N. Kolmogorov. The equations of turbulent motion in an incompressible fluid. *Izvestia Acad. Sci.*, 6:56–58, 1942.

[20] L. Prandtl. *Ü*ber ein neues formelsystem für die ausgebildete turbulenz. *Nachr. Akad. Wiss. Göottingent Math-Phys*, K1:6–19, 1945.

[21] W.P. Jones and B.E. Launder. The prediction of laminarization with a two-equation model of turbulence. *Int. J. Heat and Mass Transfer*, 15:301–14, 1972.

[22] T.H. Shih, W.W. Liou, A. Shabbir, Z. Yang, and J. Zhu. A new k-ε eddy viscosity model for high reynolds number turbulent flows. *Comput. Fluids*, 24:227–238, 1995.

[23] V. Yakhot and S.A. Orszag. Renormalization group analysis of turbulence. i basic theory. *J. Sci. Comput.*, 1:3–51, 1986.

[24] D.C. Wilcox. Multiscale model for turbulent flows. *AIAA*, 26:1311–1320, 1988.

[25] F.R. Menter. Zonal two equation k-ω turbulence models for aerodynamic flows. *AIAA*, Paper:93–2906, 1993.

[26] K. Van Maele and B. Merci. Application of two buoyancy-modified k-ϵ turbulence models to different types of buoyant plumes. *Fire Saf. J.*, 41:122–38, 2006.

[27] W.K. Chow and W.K. Mok. CFD fire simulations with four turbulence models and their combinations. *J. Fire Sci.*, 17:209–231, 1999.

[28] A. Shabbir and D.B. Taulbee. Evaluation of turbulence models for predicting buoyant flows. *J. Heat Transfer*, 112:945–51, 1990.

[29] L. Davidson. Second-order corrections of the k-ε model to account for non-isotropic effects due to buoyancy. *Int. J. Heat and Mass Transfer*, 33:2599–2608, 1990.

[30] M.O. Annarumma, J.M. Most, and P. Joulain. On the numerical modeling of buoyancy-dominated turbulent vertical diffusion flames. *Combust. Flame*, 85, 1991.

[31] S. Nam and R.G. Bill Jr. Numerical simulation of thermal plumes. *Fire Saf. J.*, 21:231–56, 1993.

[32] N.C. Markatos, M.R. Malin, and G. Cox. Mathematical modeling of buoyancy-induced smoke flow in enclosures. *Int. J. Heat. Mass Transfer*, 25:63–75, 1982.

[33] Z. Yan and G. Holmstedt. A two-equation turbulence model and its application to a buoyant diffusion flame. *Int. J. Heat and Mass Transfer*, 42:1305–15, 1999.

[34] J. Worthy, V. Sanderson, and P. Rubini. Comparison of modified $k - \varepsilon$ turbulence models for buoyant plumes. *Numer. Heat Transfer*, 39:151–65, 2001.

[35] J.C. Chen and W. Rodi. *Turbulent buoyant jets: A review of experimental data*, volume 4. Pergamon, 1980.

[36] Z. Dai, L.K. Tseng, and G.M. Faeth. Structure of round, fully developed, buoyant turbulent plumes. *J. Heat Transfer*, 116:409–417, 1994.

[37] K.B. McGrattan, H.R. Baum, and R.G. Rehm. Large eddy simulations of smoke movement. *Fire Saf. J.*, 30:161–178, 1997.

[38] T.G. Ma and J.G. Quintiere. Numerical simulation of axi-symmetric fire plumes: accuracy and limitations. *Fire Saf. J.*, 38:467–492, 2003.

[39] X. Zhou, K.G. Luo, and J.J.R. Williams. Study of density effects in turbulent buoyant jets using large-eddy simulation. *Theoret. Comput. Fluid Dynamics*, 15:95–120, 2001.

[40] X. Zhou, K.G. Luo, and J.J.R. Williams. Vortex dynamics in spatio-temporal development of reacting plumes. *Combust. and Flame*, 129:11–29, 2002.

[41] C.P. Brescianini and M.A. Delichatsios. New evaluation of the $k-\varepsilon$ turbulence model for free buoyant plumes. *Numer. Heat Transfer*, 43:731–51, 2003.

[42] H. Xue, J.C. Ho, and Y.M. Cheng. Comparison of different combustion models in enclosure fire simulation. *Fire Saf. J.*, 36:37–54, 2001.

[43] B.E. Launder and D.B. Spalding. The numerical computation of turbulent flows. *Comp. Meth. Appl. Mech. Eng.*, 41:269–89, 1974.

[44] H.K. Versteeg and W. Malalasekera. *An introduction to computational fluid dynamics.* Pearson Education Limited, 1995.

[45] B.J. Daly and F.H. Harlow. Transport equations in turbulence. *Phys. Fluids*, 13:2634–49, 1970.

[46] R. Sangras, Z. Dai, and G.M. Faeth. Mixing structure of plane self-preserving buoyant turbulent plumes. In *Mixing and radiation properties of buoyant luminous flame environments: 1. Self-preserving plumes*, pages 99–769. National Institute of Standards and Technology, Washington, DC, March 1999.

[47] R. Sangras, Z. Dai, and G.M. Faeth. Mixing structure of plane self-preserving buoyant turbulent plumes. *J. Heat Transfer*, 120:1033–1041, 1998.

[48] Z. Dai, S.K. Krishnan, R. Sangras, J.S. Wu, and G.M. Faeth. *Mixing and radiation properties of buoyant luminous flame*. National Institute of Standards and Technology, Washington, DC, October 1996.

[49] X. Zhou, K.G. Luo, and J.J.R. Williams. Large-eddy simulation of a turbulent forced plume. *European J. Mechanics, B/Fluids*, 20:233–254, 2001.

[50] Sandia National Laboratories. $http://192.84.24.155/datasite\_viv.cfm$.

[51] W. Chung and C.B. Devaud. Numerical study of a buoyant helium plume using modified k-ϵ turbulence models. pages E2.1–5, University of Waterloo, Waterloo, Ontario, May 2006. The Combustion Institute Canadian Section.

[52] W. Chung and C.B. Devaud. Comparison of buoyancy-corrected k-ε turbulence models on two helium plumes. pages C1.1–6, Banff Centre, Banff, Alberta, May 2007. The Combustion Institute Canadian Section.

[53] W. Rodi. *Turbulence models and their application in hydraulics*. PhD thesis, University of Karlsruhe, 1980.

[54] Ansys CFX 10.0. Technical reference guide. 2005.

[55] E.J. List. Turbulent jets and plumes. *Annual review of fluid mechanics*, 14:189–212, 1982.

[56] W. Chung and C.B. Devaud. Buoyancy corrected k-ε turbulence models and large eddy simulation applied to a helium plume. University of Toronto, Toronto, Ontario, May 2007. CFD Society of Canada.

[57] J.H. Ferziger and M. Perić. *Computational methods for fluid dynamics*. Springer, 2002.

[58] R.G. Rehm and H.R. Baum. The equations of motion for thermally driven buoyant flows. *J. Research of the NBS*, 83:297–308, 1978.

[59] B.M. Cetegen and T.A. Ahmed. Experiments on the periodic instability of buoyant plumes and pool fires. *Combust. and Flame*, 93:157–184, 1993.

[60] B.M. Cetegen and K.D. Kasper. Experiments on the oscillatory behavior of buoyant plumes of helium and helium-air mixtures. *Phys. Fluids*, 8:2974–2984, 1996.

[61] B.W. Albers and A.K. Agrawal. Schlieren analysis of an oscillating gas-jet diffusion flame. *Combust. and Flame*, 119:84–94, 1999.

[62] W. Zhang, A. Hamer, M. Klassen, D. Carpenter, and R. Roby. Turbulent statistics in a fire room model by large eddy simulation. *Fire Saf. J.*, 37:721–752, 2002.

[63] V.F. Nicolette, S.R. Tieszen, A.R. Black, S.P. Domino, and T.J. O'Hern. A turbulence model for buoyant flows based on vorticity generation. Technical report, Sandia National Laboratories, October 2005.

[64] P.J. O'Rourke and F.V. Bracco. Two scaling transformations for the numerical computation of multidimensional unsteady laminar flames. *J. Comput. Phys.*, 33:185–203, 1979.

[65] J.D. Ramshaw, P.J. O'Rourke, and L.R. Stein. Pressure gradient scaling method for fluid flow with nearly uniform pressure. *J. Comput. Phys*, 58:361–376, 1985.

[66] A.R. Brown, S.H. Derbyshire, and P.J. Mason. Large-eddy simulation of stable atmospheric boundary layers with a revised stochastic subgrid model. *Quart. J. Roy. Meteor. Soc.*, 120:1485–1512, 1994.